# Multi–scale modeling of hydrogen isotope transport in porous graphite

I n a u g u r a l d i s s e r t a t i o n

zur

Erlangung des akademischen Grades

doctor rerum naturalium (Dr. rer. nat.)

an der Mathematisch-Naturwissenschaftlichen Fakultät

der

Ernst-Moritz-Arndt-Universität Greifswald

vorgelegt von

Manoj Warrier

geboren am 15.12.1967

in Maula-Ali, Indien

Greifswald, 27.08.2004

Dekan          ...............................................................

1. Gutachter:      .................................................................

2. Gutachter:      .................................................................

Tag der Promotion: ...............................................................

*I dedicate this work to my*

*mother P. V. Sharada,*
*father I. K. Warrier,*
*sister Veena, and*
*wife Vasudha*

*for support, encouragement and love.*

# Contents

# Chapter 1

# Introduction

Plasma, the fourth state of matter, is the most prevalent form of matter in the universe. It is widely studied to understand the mysteries of the universe [1, 2], to achieve a clean, long term source of energy for mankind [3] and also for common industrial processes [4] that go under the collective name of plasma processing. Matter gets into a plasma state when enough energy is supplied to ionize its constituents. Once the constituents are ionized, their interactions amongst themselves are governed by electromagnetic forces. This gives rise to a wide range of properties like long range interactions, high energy density, anisotropic behavior in the presence of magnetic fields, ambipolar diffusion, waves, etc.. which gives rise to a wide spectrum for study [5, 6, 7].

One common thread among the wide variety of plasmas created in laboratories to study the various plasma phenomena is that all these plasmas are in contact with surfaces. The high energy density in a plasma means that these interactions with surfaces usually change the surface characteristics. This property of the plasma to interact with surfaces is used by industry to modify surfaces to their needs (plasma nitriding, plasma assisted sputter deposition, etc). In fusion devices, plasmas have a very high energy density and the plasma surface interaction (PSI) is a cause for concern. These plasmas erode or alter the plasma facing material (PFM) leading to a decreased lifetime or performance. The eroded impurity atoms can also get into the plasma and radiate energy thereby reducing the energy density of the plasma, making it unfavorable for satisfying the necessary criteria [8] for fusion to occur. Therefore it is important to understand the various PSI phenomena and the parameters they depend upon so as to optimize the experimental conditions for favorable results.

## 1.1   Basics of plasma–wall interaction

A plasma consists of electrons and ions kept apart by the high average energies they have. The electrons are highly mobile compared to the ions because of their smaller mass and they diffuse away faster than the ions. This results in a polarized electric field due to charge separation. When the electric potential due to charge separation becomes of the same order as the average energy of the electrons, the diffusing electrons are held back by the polarized electric field. The electron diffusion is therefore limited by the ion diffusion. This type of diffusion is called ambipolar diffusion [6]. Such a diffusion ensures that electrons are the first species to reach any surface that is exposed to the plasma. This results in the electric potential at the surface becoming lower than the plasma potential. Electrons are repelled from the surface and the positively charged ions are attracted to the surface. There is a finite region over which the potential drops from the plasma potential to the "floating potential" at the surface and this is called the sheath. Fig.1.1 [9] shows a schematic of the sheath potential in front of a wall. This sheath depends on parameters like plasma density and plasma temperature, and applied voltage to the plasma facing surface [10].

In presence of a magnetic field the ions and electrons gyrate around the magnetic field. In this case too the electrons are more mobile than the ions in a direction along the magnetic field and a sheath forms. The sheath affects the energy and angular distributions of ions incident on the plasma facing surface [10, 11, 12, 13]. Fig.1.2 shows a schematic of a sheath in the presence of a magnetic field. Note that there now appears a magnetic sheath thickness and a electrostatic sheath thickness. The magnetic sheath is determined by the bending of the ion trajectories towards the surface. For a review of plasma sheaths see [9, 10, 14].

When a flux of ions which are accelerated in the sheath is incident on a surface, a wide variety of interactions can occur. These interactions can be classified based on the underlying physical mechanism (Fig. 1.3) into

- Momentum transfer processes,

- Diffusive processes, and
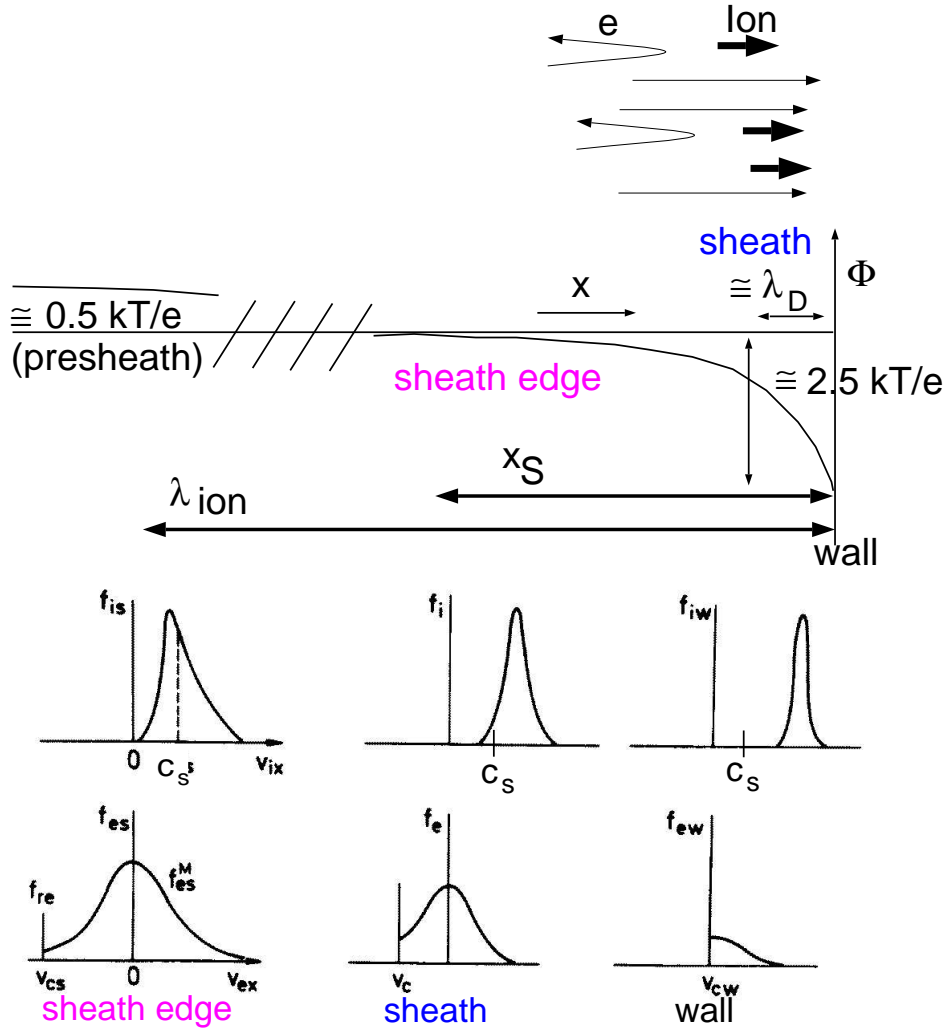
**Figure 1.1:** Schematics of the sheath potential in front of the wall without magnetic field (top). The relevant length scales are shown: Debye-length $\lambda_D$, sheath edge position $x_S$ and ionization length for neutrals $\lambda_{ion}$. In the bottom, the velocity distribution functions for ions $f_i$ and electrons $f_e$ are shown at the sheath edge, in the sheath and at the wall. The electrons have a cut-off Maxwellian (with a cut-off velocity $v_{cs}$ at the sheath edge). At the wall no electrons are going back (half -Maxwellian). The ions have already at the sheath edge a Non-Maxwellian distribution function as they are accelerated to $c_S$ or larger because of the Bohm criterion. (Figure from R. Chodura, descriptive caption reproduced from [9])

- Reactive-diffusive processes.

## 1.1.1   Momentum transfer processes

When an energetic ion is incident on a surface, it initially transfers its momentum to a target atom called the primary knock-on atom (PKA) [15] (Fig. 1.4). The incident
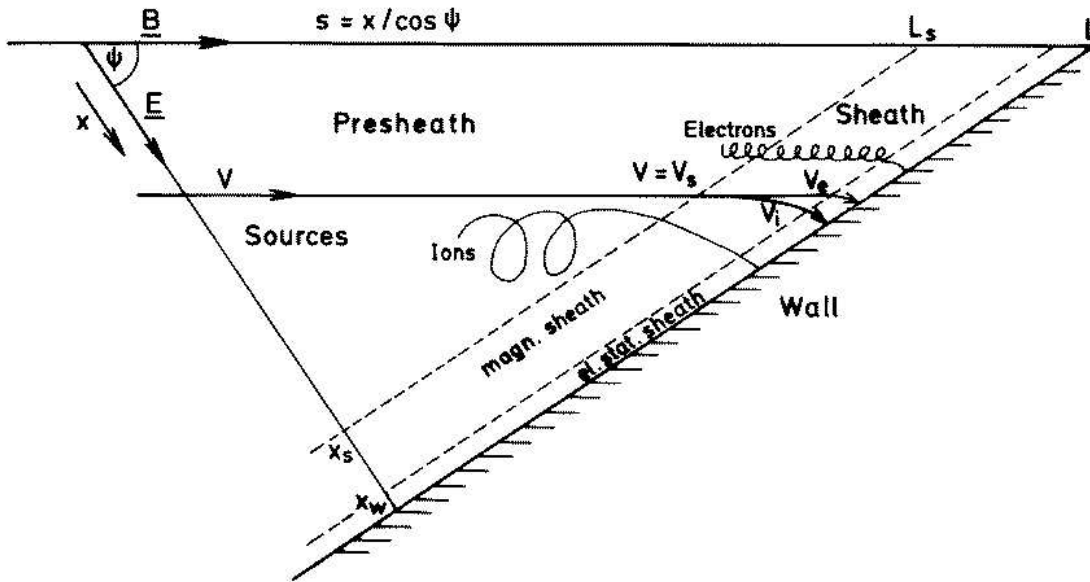
**Figure 1.2:** Schematics of the sheath with inclined magnetic field. Note that the simple sheath in Fig.1.1 is now replaced by a magnetic sheath and a electrostatic sheath. Note also that the electrons and ions gyrate around the magnetic field and if the angle made by the magnetic field **B** with the wall is small the ions can reach the wall before the electrons. (Figure from R. Chodura reproduced from [9])

atom can either lose momentum in subsequent collisions and finally come to rest in thermal equilibrium with the target (implantation) or get reflected from the target (backscattering). The PKA creates a collision cascade within the target and some of the cascading atoms can reach the surface of the target. If the atoms that reach the surface have more energy than the surface binding energy of the target material, they escape from the surface (physical sputtering). The cascading atoms also cause damage to the target and create interstitial target atoms.

The momentum transfer processes (physical sputtering and backscattering) depend on:

(i) Atomic masses of the projectile and target,

(ii) Energy of incidence of the projectile,

(iii) Angle of incidence of the projectile,

**Reactive processes**

**Momentum transfer processes**

**Physical Sputtering**

**Backscattering**

**Chemical Sputtering**

**Hydrogen recycling**

**Radiation Enhanced Sublimation (RES)**

**Diffusive processes**
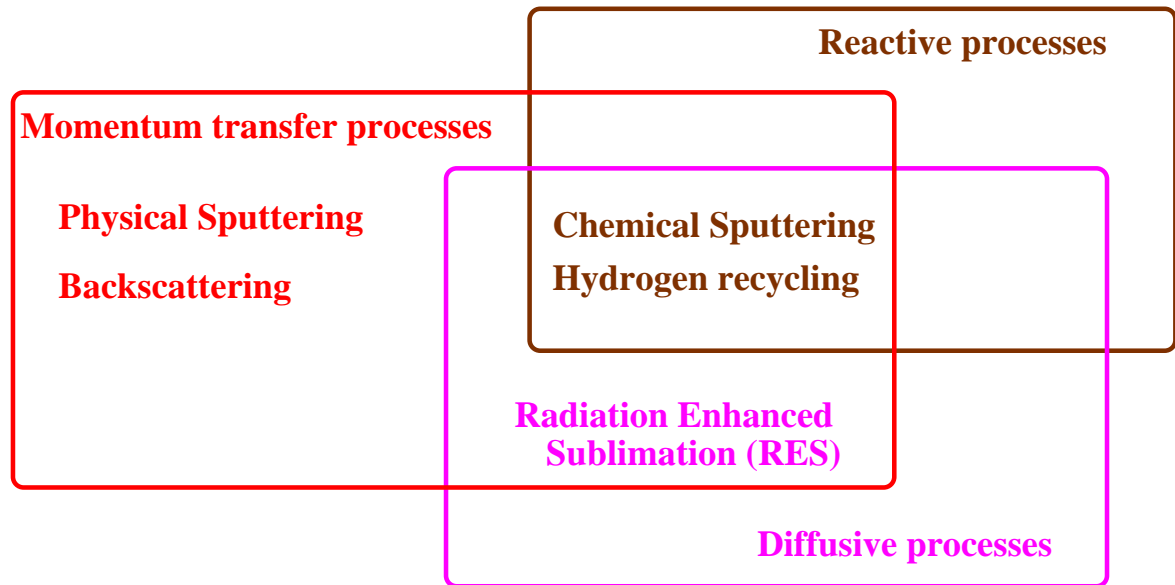
**Figure 1.3:** Classification of plasma surface interactions based on the underlying physical mechanism

(iv) Surface roughness of the target.

## 1.1.2  Diffusive and reactive–diffusive processes

The momentum transfer processes discussed above create damage sites and interstitials within their range of penetration on the target. In the case of a graphite target, at high temperatures ($>$ 1200 K) interstitial carbon atoms created by energetic incident ions/atoms diffuse along the damage sites or voids in the graphite, reach the graphite surface and get desorbed thermally (radiation enhanced sublimation – RES) [16] (Fig. 1.5). The incident atoms which have equilibrated with the surface diffuse within the target and can undergo chemical reactions with the target atoms to form new molecules. Some of these molecules diffuse to the target surface and can either be desorbed by incident atoms or be released thermally from the surface depending on the surface temperature (chemical erosion) [17, 18] Fig.1.5. In some cases an incoming energetic hydrogen atom or ion breaks a covalent C-C bond on the graphite surface by pushing apart the carbon atoms due to its short range repulsive potential. This can result in the ejection of either a carbon atom or a hydrocarbon and is called *swift chemical sputtering* [19] (Fig.1.6). Chemical sputtering of hydrocarbons is also observed at graphite temperatures lower than $500K$. This is not encompassed by Küppers model [18]. Enhanced sputtering of hydrocarbons from within the range of penetration of ions

incident atoms

backscattered atom

sputtered atom

implanted atom

PKA atom
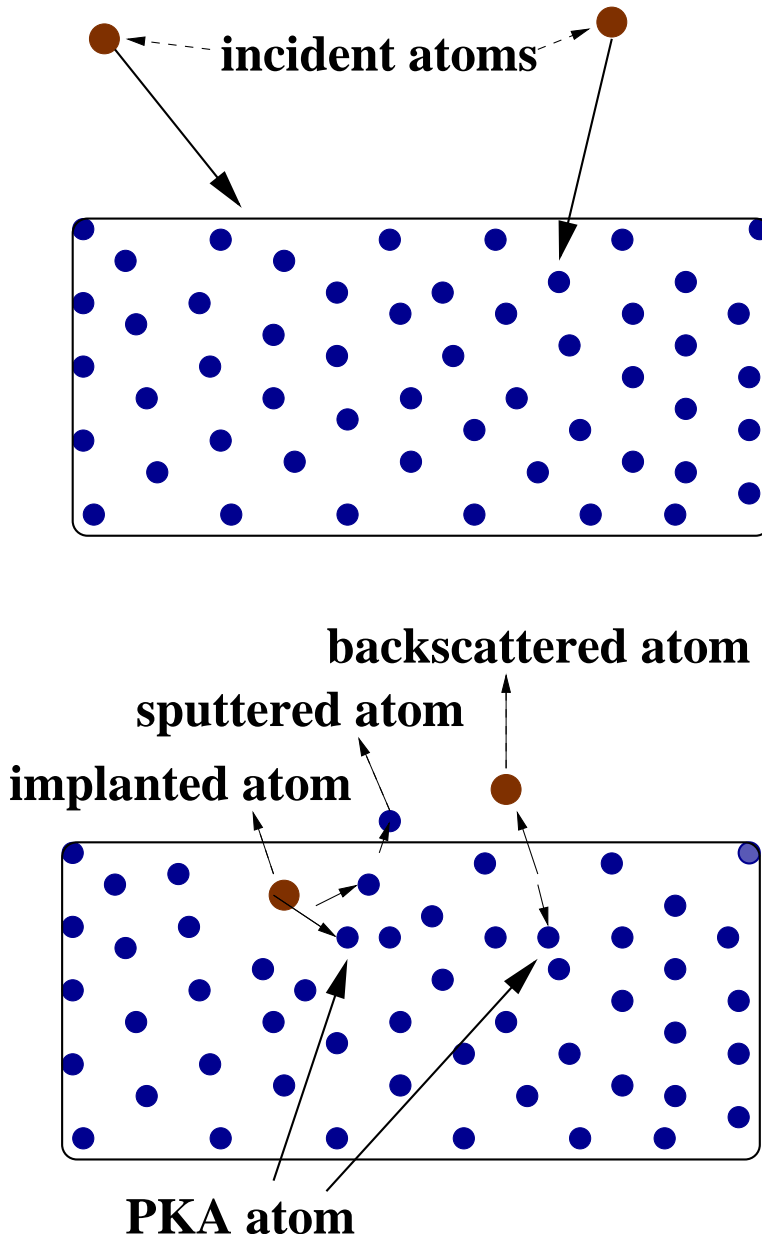
Figure 1.4: Illustration of momentum transfer processes

is also seen at these temperatures [20]. The model in [20] suggests creation of open bonds within the range of penetration of ions. These can then react with hydrogen to form hydrocarbons which can then be ejected by the swift chemical sputtering mechanism [19] (Fig.1.6).

The diffusive processes (RES) and the reactive diffusive process (chemical erosion) depend on:

## (I) Irradiated Sample

**Interstitial Carbon**

**Hydrogen**

## (II) Molecule formation and diffusion

## (III) Thermal release / desorption

**RES**

**Chemical Sputtering**

**Recycling**
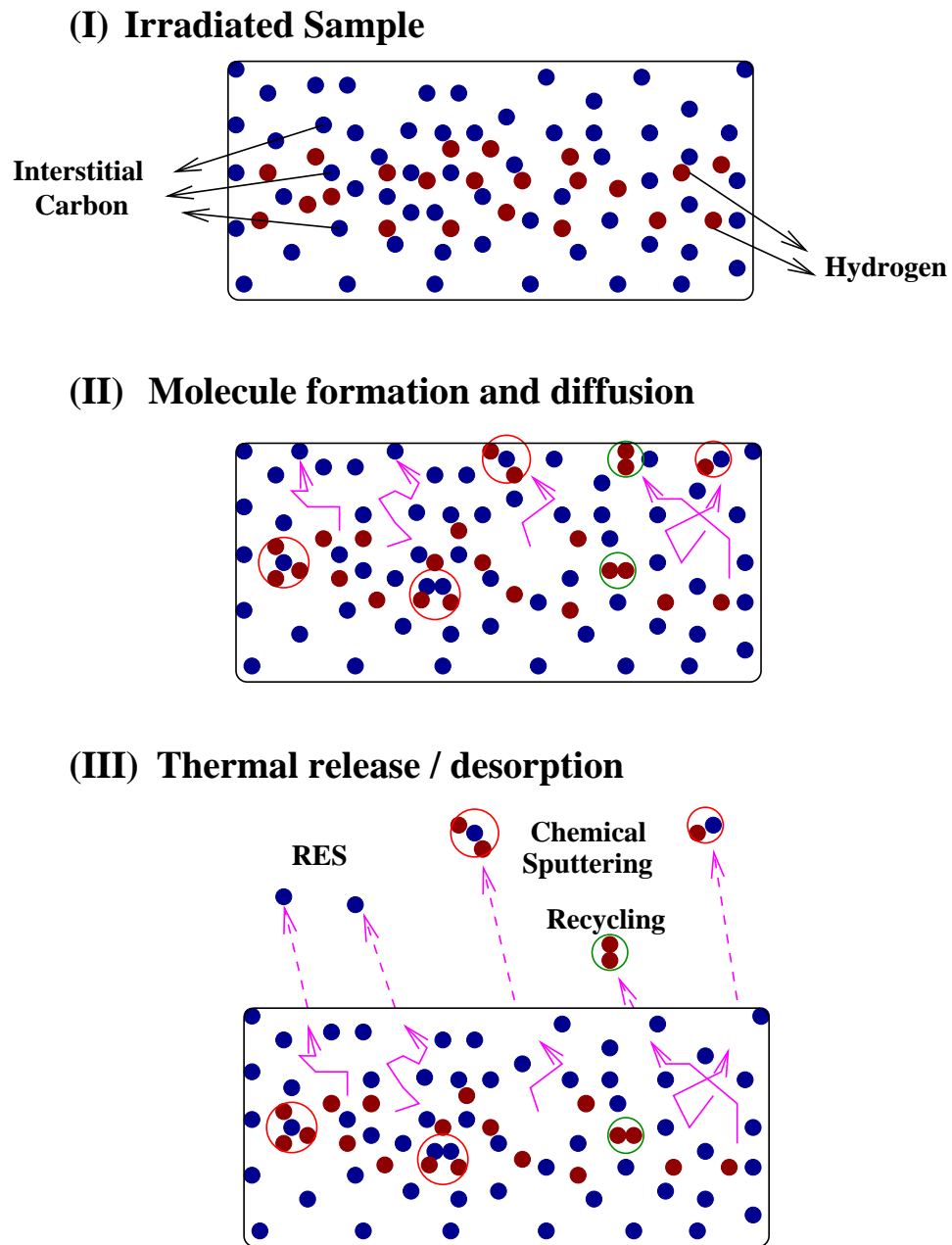
**Figure 1.5:** Illustration of reactive-diffusive processes

  (i)  The projectile mass,

 (ii)  The energy of the incident particle,

(iii)  The target temperature,

(iv)  Incident flux of particles.
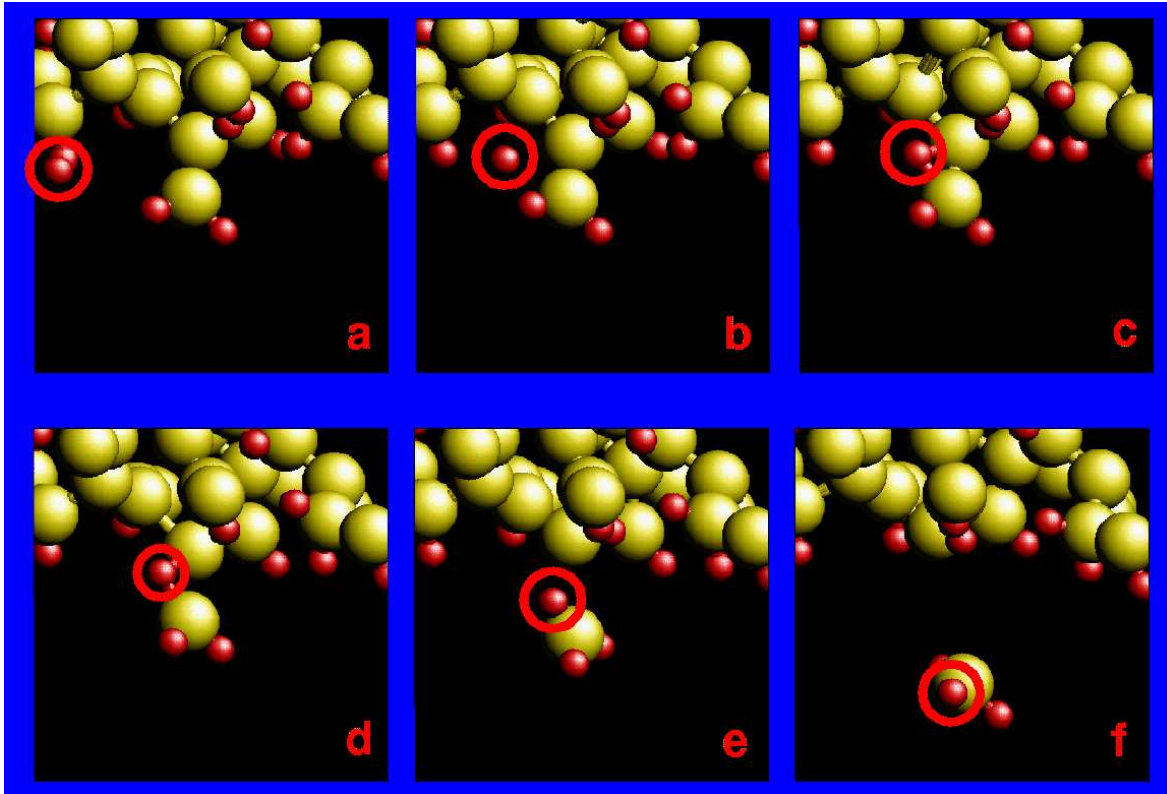
**Figure 1.6:** Illustration of Swift-chemical-sputtering processes. Note how the energetic hydrogen atom (encircled) breaks the C-C bond by which a hydrocarbon molecule is bounded on the hydrogenated graphite surface (Thanks to Emppu Salonen for this figure)

All the above erosion processes (physical sputtering, chemical erosion and RES) are quantified in terms of the ratio of the flux of target atoms leaving the surface to the flux of incident atoms (yield). Backscattering is quantified by the number backscattering coefficient, $R_N$, defined as the ratio of reflected particle flux to incident particle flux, and the energy backscattering coefficient $R_E$, defined as the ratio of reflected energy flux to the incident energy flux. The energy deposited by the plasma on the surface determines the surface temperature which is an important parameter in determining the diffusion of various species and also molecular formation on the surface. If a high energy flux is incident on a surface, the surface temperature increases and this can cause thermal evaporation of the surface atoms.

Therefore the important aspects of modeling PSI are:

- A model for the sheath (which describes the energy and particle flux distributions incident on the surface),

- A heat transport model in the target (which gives information of the temperature of the target),

- Models which specify the physical sputtering, chemical erosion and RES yields, models for backscattering coefficients, and models to evaluate thermal erosion.

Furthermore, the sputtered, recycled and evaporated atoms enter the plasma and affect the plasma parameters and therefore the particle and energy fluxes onto the target. Therefore the interaction of the edge plasma with a surface is a nonlinear feedback mechanism with the plasma parameters and the PSI coefficients depending on each other.

We have coupled models for a sheath with a simple PSI model which includes the latest empirical formulas for the above discussed PSIs and a model for heat diffusion in graphite to show the effect of such a coupling [21]. This was then incorporated into the edge transport code B2.5-SOLPS [22, 23] to study the feedback mechanisms. Appendix.A describes the simple model and the results of the coupling to SOLPS-B2.5. Appendix.B lists the empirical formulas for physical sputtering, chemical sputtering, RES, backscattering and thermal evaporation used in this study.

## 1.1.3 Additional processes

In addition to the above PSIs there exists

- Arcing [24], wherein the electric field between the plasma and the surface becomes so high that field emission of the electrons occurs and an arc is ignited which creates a melt layer on the surface (in case of metals) or craters (on graphite which sublimates),

- Blistering [25], wherein the implanted gas atoms in a target collect together at defects inside the material. When there is a continuous heat flux on the material the gas can become hot and expand causing blisters on the material surface.

- Flaking [26], wherein the surface changes cause microscopic parts of the surface to break off (flake).

- Secondary electron emission [27], due to ion and electron impact.

These effects are not addressed by the above classification and are beyond the scope of this thesis.

## 1.2 Motivation and main focus of this thesis

### 1.2.1 Advantages of graphite as a plasma facing material

Magnetic fusion devices are a promising energy source for the future due to the availability of abundant fuel - hydrogen isotopes and also because of the fact that they are more environmentally tolerable. A figure of merit of a magnetic fusion device is the fusion triple product [28] which is defined as the product of the plasma density $(m^{-3})$, the plasma temperature $(keV)$ and the plasma confinement time $(s)$. Figure Fig.1.7 shows the progress of tokamaks towards achieving fusion reactor conditions. Typical
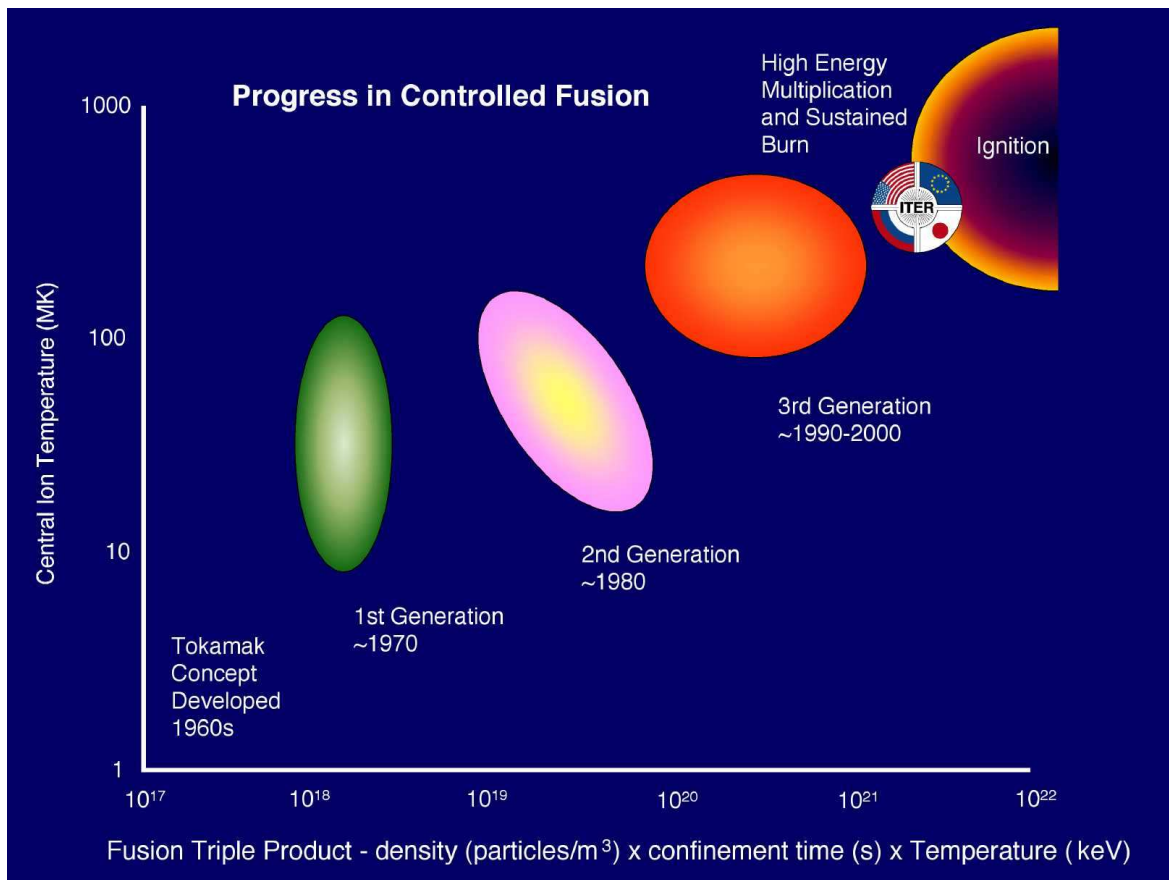


**Figure 1.7:** Progress towards Fusion Reactor conditions (published with kind permission of ITER)

plasma parameters in the current devices are temperatures of $10^8$ K and densities of around a few times $10^{19}$ $(m^{-3})$ confined for a second. This results in typical heat fluxes of a few $MWm^{-2}$ and particle fluxes of a few times $10^{23}$ $m^{-2}s^{-1}$ on the plasma facing surfaces. Therefore the plasma facing surfaces in these devices must have a very good thermal conductivity and high melting points from a heat handling point of view. Furthermore the erosion of the plasma facing surfaces leads to contamination of the plasma and therefore energy loss from the plasma by radiation. This loss is proportional to the atomic number $Z$ raised to the fourth power [29] which makes low $Z$ materials a better choice as plasma facing material (PFM). Graphite is the material of choice due to its high thermal conductivity, high sublimation energy and low $Z$ for these devices. However as the stage sets for the construction of a fusion reactor prototype ITER [30] where long PFM lifetimes and recovery of tritium (which is radioactive and must be recycled) is necessary, some shortcomings of graphite come to the fore.

## 1.2.2   Shortcomings of graphite as a plasma facing material

(i) There is uncertainty about the extrapolation of the chemical sputtering yield to high reactor relevant fluxes and in accounting for higher hydrocarbon formation [31, 32, 33]. Currently there exist good semi-empirical models for chemical erosion [17, 34] based on Küppers model [18] which fit a large number of experimental results.

(ii) The mechanisms leading to chemical sputtering at graphite temperatures lower than $500K$, called surface sputtering, which are not encompassed by Küppers model are not fully understood [20].

(iii) There is also a great disparity in the diffusion data of hydrogen isotopes in graphite [35].

(iv) Moreover the sputtered carbon/hydrocarbons can react with the tritium in the plasma and form co–deposited layers from which tritium recovery is impossible [36]. When making the transition to reactor relevant fusion machines with long pulse times, tritium co–deposition and recovery is so serious an issue that other plasma facing materials are considered instead of graphite or Carbon Fiber Composites (CFCs) [36, 37].

### 1.2.3   Focus of this thesis

The main reason for the various uncertainties listed above is the complex structure of graphite. It is highly chemically reactive and porous. An illustration of the porous structure of graphite, with typical length scales is shown in Fig.1.8. It consists of granules of size around a few microns separated by voids which are typically of the order of 0.1 $\mu$. The granules themselves are made up of crystallites (regions of crystal graphite) which are a few nanometers wide. The crystallites are separated by micro–voids which are a few Å wide [38, 39, 40]. This results in large chemically reacting internal surfaces which the hydrogen isotopes can diffuse into, recombine or form hydrocarbons and get trapped in the bulk of the graphite.

It is essential to understand the effects of porosity, trapping at internal surfaces, the chemical interactions that can occur within graphite, and the transport of hydrogen and the molecules formed, to interpret existing experimental results and to design new types of graphite based PFMs which are better suited as fusion reactor first wall materials. In order to study these processes a hierarchy of models is necessary at vastly differing length and time scales:

- Hydrogen isotope migration in crystallites which are a few nanometers in size

- Hydrogen interaction at crystallite–microvoid interfaces and trans–granular–diffusion (TGD), which is a few microns in size

- Hydrogen isotope molecule formation and transport in the voids and granule surfaces, which is typically over the size of the graphite target in fusion devices (a few cms)

Note that the time scale for these processes depends on the local microscopic graphite qualities and may change widely depending on the available number of traps, the local graphite temperature, the hydrogen concentration, etc. This sets the main focus of this thesis, which is, **to create a framework to study multi–scale transport of hydrogen isotope in a porous graphite–like structure as a test–bed** for addressing other problems concerning the use of graphite in fusion devices, such as:

- the full chemical sputtering problem,

- the hydrogen isotope inventory (tritium and isotope exchange studies),
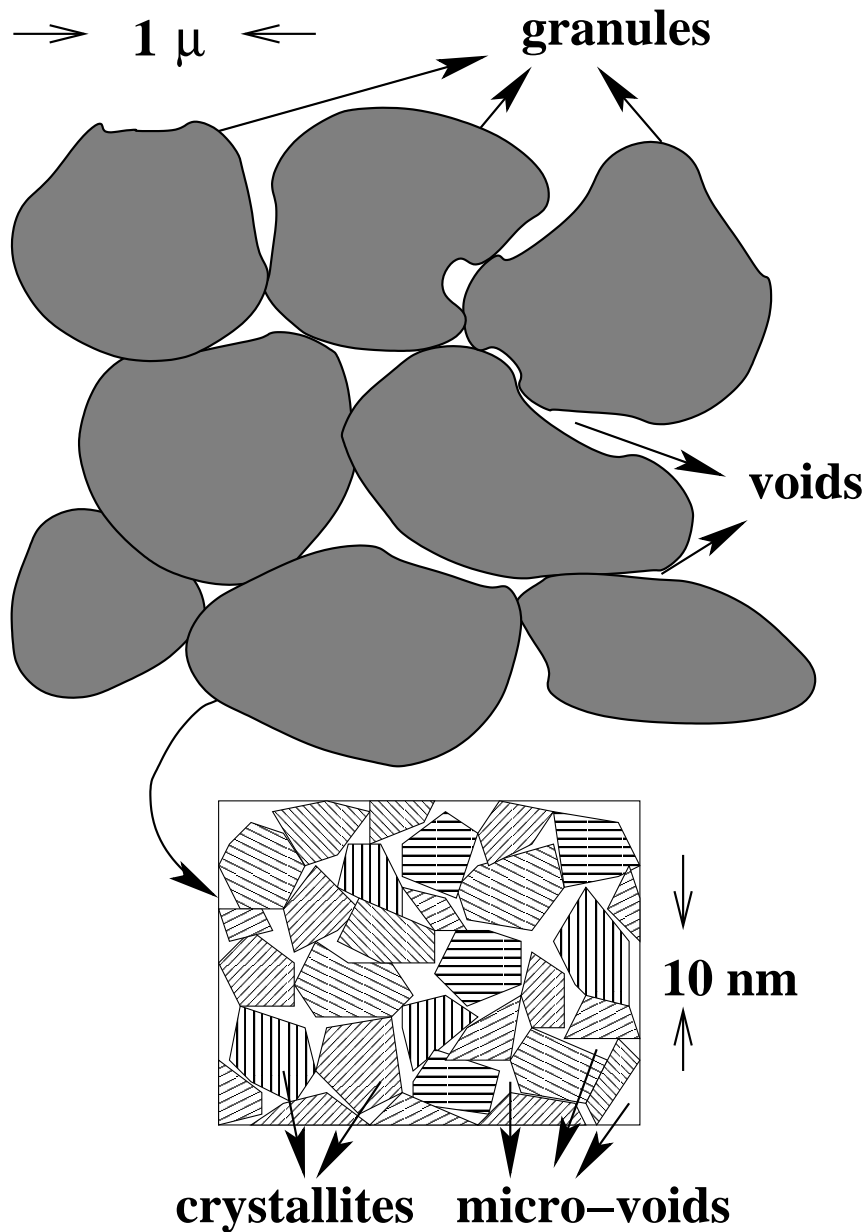
Figure 1.8: The porous structure of graphite

## 1.3   Multi–scale strategy

Many models have been proposed for hydrogen isotope recycling in porous graphite
and in other candidate PFMs [38, 39, 40, 41]. Others have studied hydrocarbon for-
mation and transport in graphite [34]. These models are macroscopic models and use
rate constants obtained from experiments [18, 42, 43, 44, 45, 46] some of which are
still in need of theoretical explanation. They also make use of simplifying assump-

tions of the porous structure to make the problem tractable. On the other hand there are microscopic models [19, 47, 48] which use molecular dynamics (MD) which deals with the interaction amongst individual atoms with either empirical potentials or density functional theory and give a good insight into the microscopic mechanisms studied.

In order to understand the physical microscopic processes contributing to the macroscopic transport, it is essential to use the insights gained from the microscopic models (consisting of a few hundreds of atoms over a time scale of a few picoseconds), and from experiments, into modeling the hydrogen isotope reactions and transport at the meso–scale (TGD) and further into the macro–scale (typically a centimeter over a time scale of several seconds). Therefore a multi–scale (both in length and time) approach to modeling PSI is necessary. In addition to the multiple scales involved one must also consider the effect of the porous structure of the PFM on particle transport.

We develop a multi–scale scheme for incorporating microscopic physical observations from modeling and experiments into modeling macroscopic transport in porous graphite. The scheme is illustrated in Fig.1.9. Molecular dynamics (MD) is used to study the diffusion of hydrogen isotopes in a graphite crystal. The length scale for this process is a few nanometers and the simulation time is hundred picoseconds. Chapter.2 describes the MD simulation. We then parametrize the diffusion in terms of potential wells $E_m^{l,h}$, jump attempt frequencies $\omega_o^{l,h}$ and jump distances $L^{l,h}$, so that a kinetic Monte Carlo (KMC) code **DiG**, which is much faster and reproduces the MD results can be used for scaling up. Chapter.3 describes parametrization of the MD results for use in KMC. Scaling up in length scales introduces the necessity of taking into consideration the porous geometry of graphite. A general scheme based on [49] is used to create the porous graphite geometry. This scheme can be used to create both, the crystallites separated by microvoids, and the granules separated by voids. KMC is used to simulate the transport of hydrogen isotopes in randomly oriented crystallites with a trapping–detrapping model at the microvoid–crystallite interfaces. Chapter.4 describes this scaled up trans–granular–diffusion. To simulate the macroscopic transport of hydrogen isotopes in graphite, the diffusion coefficients obtained from the simulations at the meso–scale $D_{TGD}$ is used in a Monte Carlo Diffusion (MCD) anzatz to simulate TGD, and the KMC code is used to simulate the transport in voids and desorption from the surface. Chapter.5 describes this macroscopic simulation. Finally in Chapter.6 a few applications of the multi–scale code are presented. Chapter.7 summarizes the work.
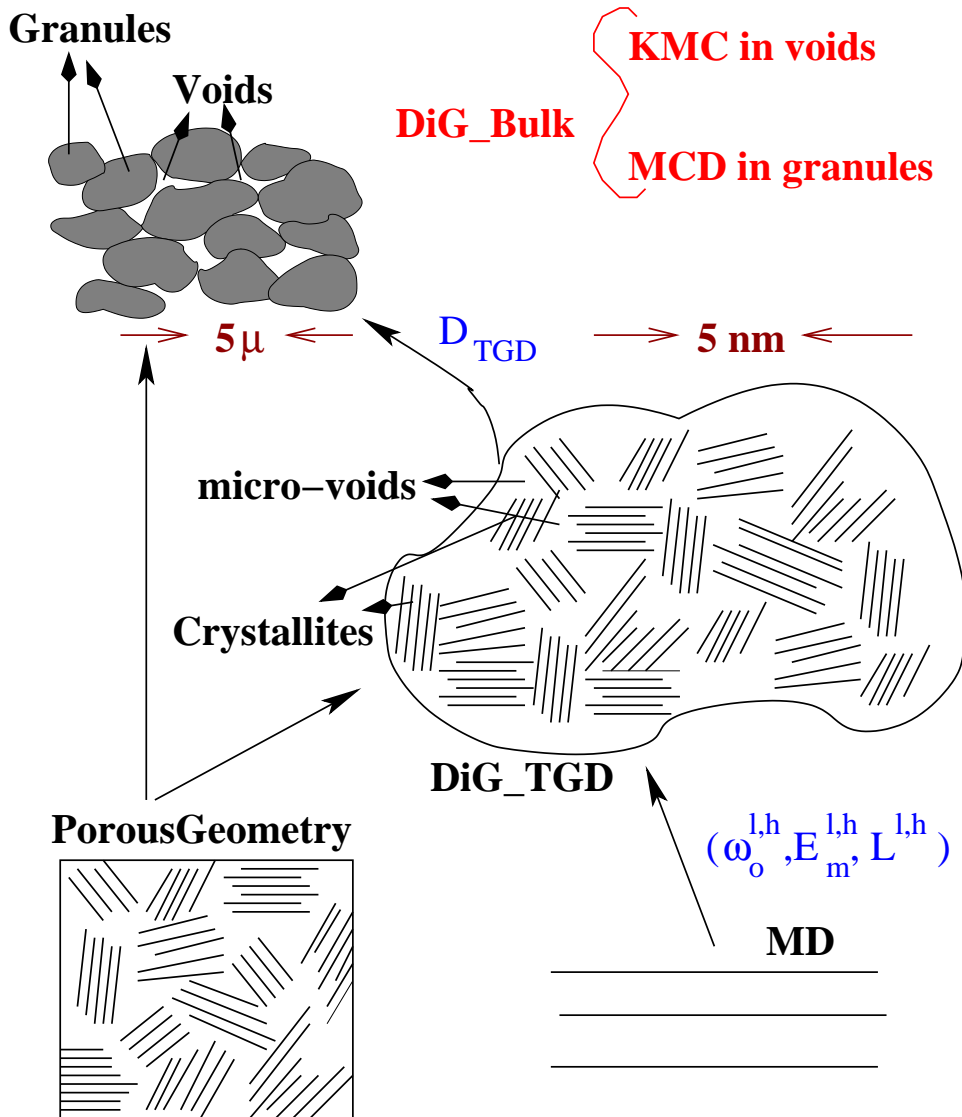
**Figure 1.9:** The Multi–scale scheme. **DiG_TGD** is the version of the multi–scale code that handles trans–granular–diffusion and **DiG_Bulk** is the version that handles Bulk diffusion. Note that various parameters (explained in the text) are transferred from **MD** to **DiG_TGD** and from **DiG_TGD** to **DiG_Bulk**

## 1.4  Guiding principles

There are many problems that can be studied at each of the scales lengths. For example, saturated hydrogen diffusion in crystallites, the SP3-SP2 ratio of carbon at the edge of crystallites, etc are interesting at the nanoscales. Similarly the H isotope

recombination studies for H and D implanted at different depths [39, 38] and hydrocarbon formation and transport are interesting at the micro–scales ($\sim 10^{-6}$ meters). At the centimeter scales hydrogen isotope recycling, etc are interesting. However, in this thesis we concentrate on developing the multi–scale toolbox using which many of these problems can be tackled at different scales. This approach has an analogy with the computer game kmines, wherein, the player marks out potential positions of "mines" that can stop the game and goes ahead with playing the game (Fig. 1.10). Like in the game, the insights gained from the larger picture can also help in resolving the more localized problems. We have attempted to compare our models with experiments



**Figure 1.10:** Computer game kmines

wherever possible. From the understanding obtained from the simulations, we have tried to make simple models which reproduce the simulation results. The multi–scale code is written in a modular fashion so that different modules can be chosen in order to simulate different problems at different scales.

# Chapter 2

# Molecular Dynamics simulations of hydrogen isotope diffusion in crystalline graphite

In this chapter the hydrogen isotope transport in a graphite crystal, at nanometer scales, is investigated using MD.

## 2.1 Brief introduction to molecular dynamics simulations

The most intuitive method to study microscopically the motion of atoms and their interactions amongst themselves is to solve the N body force equation,

$$m_i \ddot{\vec{r}}_i = \sum_{i \neq j, j=1}^{N} -\nabla \Phi_{ij} \tag{2.1}$$

where $\vec{r}$ is the position vector of a particle denoted by $i$, $m_i$ is the mass of the $i^{th}$ atom and $\Phi_{ij}$ is the interatomic potential between the $i^{th}$ atom and the $j^{th}$ atom. Molecular dynamics (MD) aims to do exactly just this using a computer since even for very small N, or for complicated forms of $\Phi_{ij}$, the above equation is not analytically solvable. Solving the above equations numerically on a computer has the following limitations:

- The inherent limitation of the time step being around a femtosecond to simulate materials, so as to cater to numerical stability.

- The number of atoms which can be simulated is limited to between 100 and $\sim 10^9$, depending on the type of potential used and the speed of the computation system.

## 2.1.1   Limitation in the time step

The limitation of the time step to a femtosecond can be understood as follows: Numerical schemes to solve Eqn.2.1 use a Taylor expansion

$$r(t + \Delta t) = r(t) + \dot{r}\Delta t + \frac{\ddot{r}}{2}(\Delta t)^2 + ..... \tag{2.2}$$

Different schemes truncate at different orders of the time step $\Delta t$ which determines the accuracy of the position calculation and also the time step to be used. For a discussion which evaluates the various numerical schemes that can be used in MD, see [50] (pages 69-84). In brief, for numerical stability it is required that the change in potential with a change in position of the coordinate of a particle in time $\Delta t$ must not be large (note that the second term of the Taylor expansion in Eqn.2.2 is equal to $-\nabla\Phi$). A simple rule of thumb frequently used is that the particle can move at most $(1/20)^{th}$ the distance between two neighboring atoms [51] (lecture 2). Typical interatomic distances in a graphene plane is $\sim 1.4$ Å and the typical velocity of an interstitial hydrogen atom which has equilibrated with the graphene plane at say 900 K is $\sim 0.047$ Å/femtosecond. Therefore the time step has to be 1.5 femtoseconds in this case and one would have to loop over $\sim 10^{15}$ iterations to simulate one second!!

## 2.1.2   Limitation in the number of atoms simulated

The second limitation depends on the choice of the interatomic potential, $\Phi$. Quantum mechanical approximations like Hartree–Fock (HF) methods, density functional theory (DFT) [52, 53], tight binding (TB) [54]) can be used to calculate $\Phi$ at each step. However this limits the number of atoms that can be simulated. On the other hand, analytical potentials can handle much larger numbers of atoms. There exist many two body potentials which can be used to simulate noble gases and other spherically symmetric structures [55, 56]. For structures which are not spherically symmetric, special care has to be taken to incorporate the symmetry of the solid being modeled (eg. the three body Stillinger-Weber potential [57]). There also exist standard potentials for special classes of systems like the embedded atom method (EAM) for metals [58].

Recently, analytical reactive bond order potentials (REBO) have become very attractive for simulating carbon based systems [59]. These are based on the ideas proposed by Abell [60] wherein the effect of electron contribution to the potential is modulated based on the local atomic coordination number (i.e. number of neighbors) by a "bond–order" function. Tersoff proposed a potential [61] which incorporates angular interactions and the dependence on local atomic coordination number. This models Si, Ge and C very well and the Abel-Tersoff formalism was shown to produce correct trends for potential barriers in chemical reactions by D. Brenner [62]. For a discussion on interatomic potentials from quantum to empirical to REBO see [51] (lectures 7 to 11), and for a discussion on the development of REBO see [59]. Table.2.1 (reproduced with permission of K. Nordlund), shows a rough estimate of the maximum number of atoms, $N_{max}$, that can be simulated in a week or so, on a single processor machine.

**Table 2.1:** Rough estimate of the number of atoms that can be simulated in MD for different methods of evaluation of interatomic forces

| Potential Model | Type | Scaling | $N_{max}$ |
|---|---|---|---|
| HF | Quantum mechanical | $O(N^{4-8})/O(N)$ | 50 |
| DFT | Quantum mechanical | $O(N^3)/O(N)$ | 200 |
| TB | Quantum mechanical (often semi–empirical) | $O(N^3)/O(N)$ | 1000 10000 |
| Many body and pair | classical, semi–empirical | $O(N)$ | $10^7$ |

As far as the carbon–hydrogen system is concerned, D. Brenner, using a highly parametrized Tersoff bond-order expression as a fitting function for a number of small hydrocarbon molecules, graphite and diamond, constructed an empirical potential [63] which reproduces hydrocarbon formation and can be used to study hydrogen isotope interaction with graphite. K. Nordlund extended the Brenner potential [64] to include long range interactions perpendicular to the the graphene planes so that crystal graphite could also be simulated. We use the Brenner potential with Nordlund's extension to simulate hydrogen isotope diffusion in crystalline graphite.

### 2.1.3    Other important aspects of a MD simulation

Other aspects of a MD simulation involve:

- Speeding up techniques,

- Boundary conditions depending on the problem,

- Fixing the macroscopic parameters of the system of particles like temperature, pressure and volume,

- Post-processing to check the consistency of the simulation and to analyze the results.

These are basic to MD simulations and good introductions to all these aspects can be found in [50, 51, 65, 66]. These aspects are briefly mentioned here only to introduce the technical terms used to describe the simulation.

**Speeding up techniques and boundary conditions**

Since the computation time of a MD simulation scales with the number of atoms in the simulation, one would want to use the minimum number of atoms as is possible without compromising on the accuracy of the results. To this end truncation of potentials, creating neighbor lists and judicious use of boundary conditions is important. When the interatomic potential falls off rapidly with distance, short range interactions dominate the simulation. The contribution of atoms beyond a critical distance $r_c$ becomes small and this error can be evaluated and corrected. This kind of simple truncation of the potential where the potential beyond $r_c$ is neglected can lead to infinite gradients in $\Phi$ at $r = r_c$ which leads to a numerically unstable situation as discussed above. Therefore the potential is truncated and shifted such that it becomes zero at $r = r_c$. In this case the potential energy and pressure on a system with a truncated and shifted $\Phi$ changes and corrections must be evaluated and applied. To further save computation time a list of atoms, called the neighbor list, within $r_c$ is maintained. This list is updated with a frequency depending on the rate at which atoms may move into or out of the neighborhood.

In order to simulate homogeneous bulk systems, periodic boundary conditions (PBCs) are used. This is illustrated in Fig.2.1 for a two dimensional system. Box
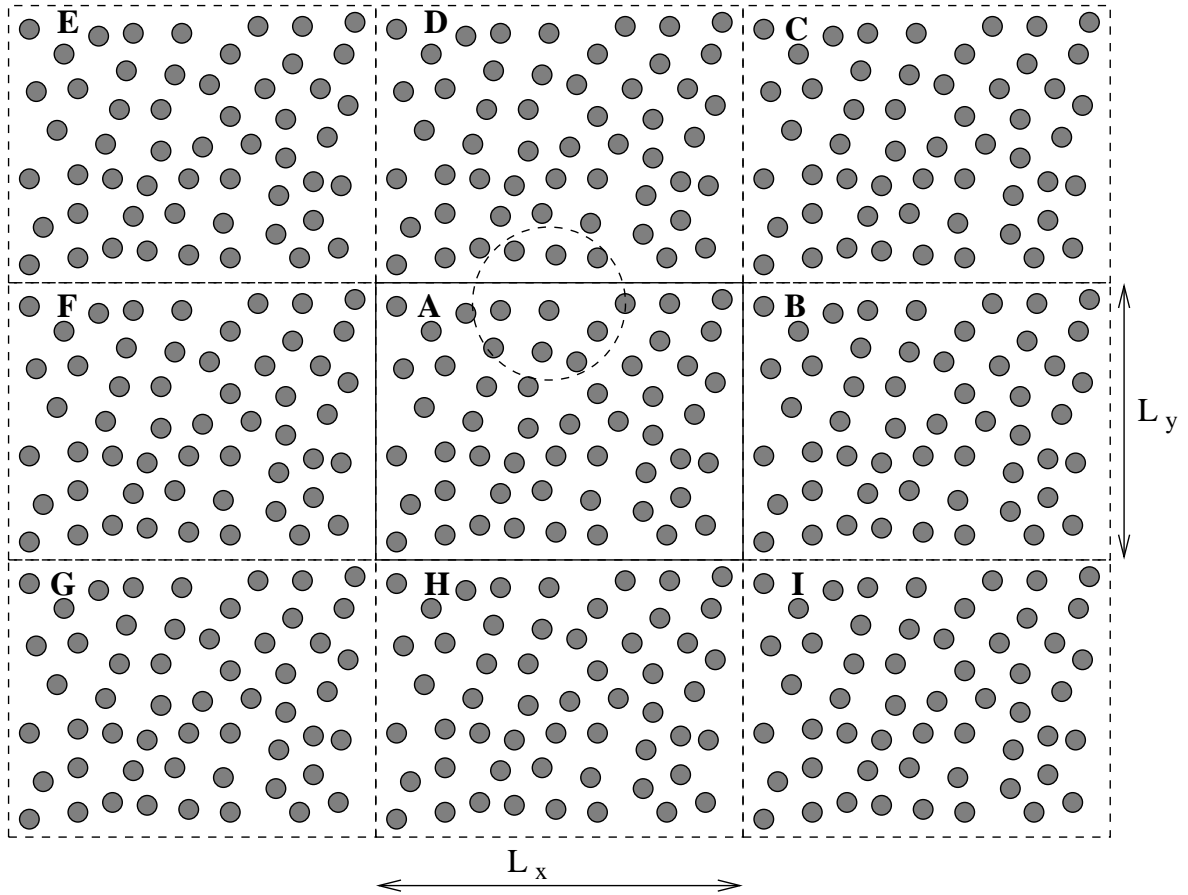
**Figure 2.1:** Illustration of periodic boundary conditions (PBCs) in a MD simulation

**A** having size $L_x$ and $L_y$ in the X and Y directions is replicated at its 4 edges and 4 corners to form boxes labeled **B**, **C**, **D**, **E**, **F**, **G**, **H**, **I**. The force calculation for atoms within a distance $r_c$ of these corners or edges (note the dashed circle on the top edge of **A**) involves those atoms that lie at the bottom edge of box A which due to PBCs also lie in box **D**. Note that such an ansatz is valid only when evaluating physical quantities with local correlations. Only fluctuations that have a wavelength not greater than the single box size can be simulated. Care must also be taken to avoid spurious correlations that can creep in due to assumed periodicity of the system and care must be taken that $r_c < L_{x,y}/2$.

Other boundary conditions that can be used are "free" or "open" boundary conditions which can be used when simulating a small collection of atoms or a long molecule which is unbounded. In this kind of boundary condition, the force calculation is carried out over existing atoms within $r_c$ without any replication of boxes. Such boundary con-

ditions can also be used to simulate surfaces where no replication is carried out along the direction normal to the surface, (say $Z$, with the surface lying at $Z = 0$). PBCs are implemented along the plane (say $X - Y$) in which the surface extends. At $-L_z$, where $L_z$ is the dimension of the system along Z, the bottommost atoms can be held fixed with atoms lying within $r_c$ of these atoms assigned a temperature equal to the bulk temperature (assigning a temperature is discussed under the topic **fixing macroscopic parameters** below). Note that some potentials fitted for modeling bulk phenomena may not be suitable for modeling surfaces correctly. Furthermore in the special case of simulating interactions of fast particles with a surface, special considerations have to be made for the time step, and boundary conditions called "slab–boundary–conditions" are applied. In this case, the atoms lying at the faces bounding the system in the $X$ and $Y$ directions are held fixed and atoms lying within a distance $r_c$ from these faces are assigned a temperature equal to the bulk temperature. The system size and impact position of the fast particle must be chosen such that the collision cascade does not extend to the temperature controlled regions.

## Fixing macroscopic parameters

Statistical mechanics provides a link between the macroscopic properties of matter (like temperature, pressure, etc.) and the microscopic properties (like positions, velocities, individual kinetic and potential energies) of atoms and molecules that constitute it. These macroscopic properties reflect the time average behavior of the atoms at equilibrium (i.e in one of the many possible degenerate minimum energy states accessible to the system). Details of this are available in any book on MD [50, 65, 66] and is not reproduced in this thesis where MD is only the first step in a multi–scale–model. Here only the basic technical terms in the MD simulation are addressed.

Before doing the MD simulation one is faced with the task of initializing the atomic positions and velocities. In the case of crystalline solids the starting positions will be defined by the crystal symmetry and positions of atoms within the unit cell of the crystal. The unit cell is then repeated to fill up the desired dimensions of the system. Realistic atomic displacements from crystal lattice sites can also be derived using the Debye model [51] (Lecture 2, page 12). For amorphous solids the particles can be randomly distributed within the desired dimensions making sure that there exists a minimum distance between the atoms so that strong local forces do not exist in the

system.

The initial velocities are set by assuming a Maxwell-Boltzmann distribution for velocities along the three dimensions. This is done by using Gaussian distributed random numbers multiplied by a mean square velocity given by $\sqrt{2k_B T/m}$ in each of the three directions and making sure that the system has total momentum equal to zero. Generally speaking, if sensible (tailored to avoid large impulsive forces) position and velocity distributions are chosen, particle positions at equilibrium relax to oscillating around the minimum energy locations of the potential $\Phi$. A Maxwellian distribution of velocities is naturally obtained in the simulation.

Therefore the initial temperature and total energy of the system has been fixed. The temperature is fixed by the velocity distribution. The total energy of the system is given by

$$E_{tot} = KE_{tot} + PE_{tot} \tag{2.3}$$

where $KE_{tot}$ is the total kinetic energy in the system given by

$$KE_{tot} = \sum_{i=1}^{N} \frac{1}{2} m \left( v_{x,i}^2 + v_{y,i}^2 + v_{z,i}^2 \right) \tag{2.4}$$

and $PE_{tot}$ is the total potential energy of the system given by

$$PE_{tot} = \sum_{i=1}^{N} \Phi_i(r_i) \tag{2.5}$$

with $v_{x,y,z}$ being the velocities, $r$ being the positions of atoms, and $i$ being the index that sums over all the atoms $N$ in the system. $\Phi_i(r_i)$ is the potential energy of the $i^{th}$ atom due all other atoms in the system. In a optimized MD simulation, with truncated–shifted potentials, $\Phi_i(r_i)$ is calculated by summing over the potential energy at $r_i$ due to the atoms in the neighbor list and adding truncation and shifting corrections.

The recipe used to fix the temperature above cannot be used at every time step since this fixes the temperature rigidly. This also destroys the purpose of solving Eqn.2.1, since atoms are assigned velocities randomly at each time step. Normal tem-

perature fluctuations are suppressed. There are many methods to control temperature and pressure [67, 68, 69]. Our MD simulations implement the Berendsen temperature and pressure control [69] and only this is described below.

In the Berendsen temperature control scheme, all velocities are scaled at each time step by a factor $\lambda$ given by

$$\lambda = \sqrt{1 + \frac{\Delta t}{\tau_T}\left(\frac{T_o}{T} - 1\right)} \qquad (2.6)$$

where, $\Delta t$ is the time step of the simulation, $\tau_T$ is the time constant for temperature control and has to be greater than $100\Delta t$, $T_o$ is the desired temperature and $T$ is the current temperature. The Berendsen pressure control is implemented by changing all atom positions, and the system size is scaled at each time step by a factor $\mu$ given by:

$$\mu = \left[1 - \frac{\beta \Delta t}{\tau_P}(P_o - P)\right]^{\frac{1}{3}} \qquad (2.7)$$

where $\tau_P$ is the time constant for pressure control which should be typically greater than $100\Delta t$, $P_o$ is the desired pressure and $P$ is the current pressure. $\beta$ is the isothermal compressibility of the system. This type of temperature and pressure scaling gives realistic fluctuations in temperature and pressure when large values of $\tau_T$ and $\tau_P$ are chosen.

**Post processing of results**

Solving Eqn.2.1 gives the particle positions and velocities at each time step. The total kinetic energy, potential energy and total energy can also be output using Eqns.2.4,2.5, 2.3, averaged over a certain number of fixed time steps. Depending on the type of ensemble simulated, various macroscopic parameters of the simulation like temperature, pressure, specific heat at constant pressure or at constant volume, etc can be output. Various transport coefficients are related to time correlation functions of various measurable quantities in a MD simulation as given by the Green-Kurbo relations. See [50] (Section 4.4.1 and Appendix C) for details. We carry out MD to study the diffusion of hydrogen isotope in crystalline graphite and therefore we discuss only this aspect here.

We obtain the diffusion coefficient using the Einstein relation:

$$D \;=\; \lim_{t \to \infty} \frac{1}{2dt}\,[r(t) - r(o)]^2 \tag{2.8}$$

where $D$ is the diffusion coefficient, $d$ is the dimensionality of the system and $<r(t)>$ is the position of the atom at time $t$. This is proportional to the slope of the mean square displacement of a single particle undergoing Brownian motion at the long time limit and is also known as the "tracer diffusion coefficient" [70].

## 2.2 Molecular dynamics study of hydrogen diffusion in graphite

We use the HCParcas code to study hydrogen isotope diffusion in crystalline graphite. The code, which is written and maintained by Kai Nordlund, uses the Brenner potential [63] with the Nordlund long range interaction term [64] to simulate a graphite crystal. The simulations consist of a single H isotope diffusing in a graphite crystal consisting of 960 atoms. A Berendsen's thermostat [69] was used to maintain the temperature of the crystallites. Simulations were carried out at 150 K, 300 K, 450 K, 600 K, 750 K and 900 K. Periodic boundary conditions are applied along **X**, **Y** and **Z** in all the simulations described below. **X-Y** is the plane of the graphene layer, and **Z** is perpendicular to the graphene layers. The simulations were carried out for 100 picoseconds with a time step of less than a femtosecond.

### 2.2.1 Setting up the simulation

The graphite crystal samples are prepared by starting with 960 carbon atoms at the graphite crystal locations. The crystal consisted of 10 unit cells along the **X** direction, 12 unit cells along the **Y** direction and 2 unit cells in the **Z** direction. This results in 4 graphene layers as shown in Fig 2.2. In the figure, all carbon atoms belonging to a graphene layer are assigned the same color with each graphene layer being assigned a different color. The interstitial hydrogen isotope is created by randomly picking a position between the two graphene layers in the center of the graphite crystal and making sure that it is more than 1.5 Å from any of the carbon atoms constituting the graphite lattice. It is given zero initial velocity. The interstitial trajectory is also visible in Fig.2.2 as a yellow wriggling line. The atoms are then allowed to equilibrate
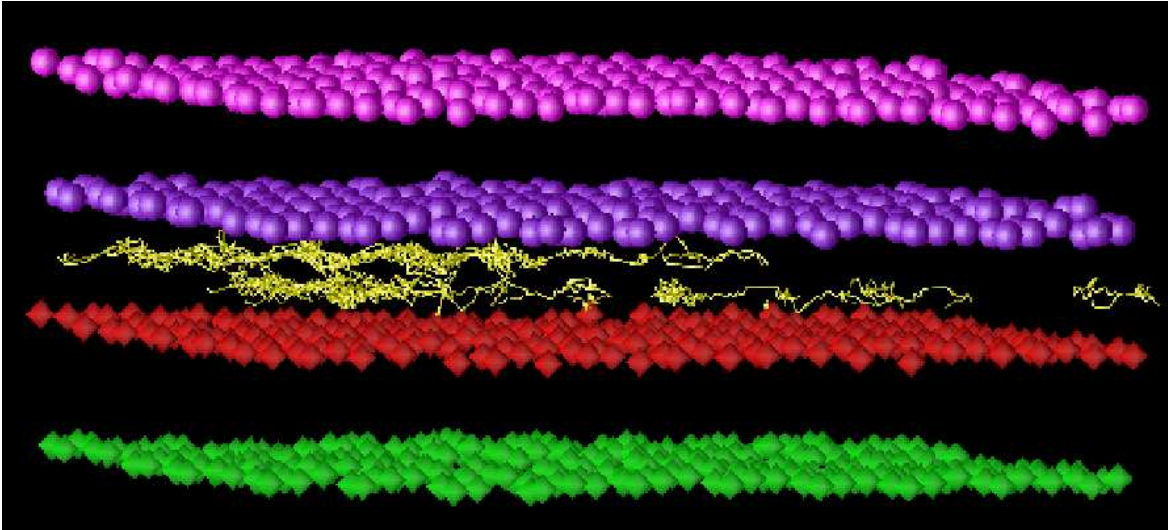
**Figure 2.2:** A typical graphite crystal chosen for doing the MD simulation

using Berendsen's pressure control along **X** and **Y** until they reach a lowest potential energy state and the pressure oscillates around zero.

## 2.2.2 Results and analysis

### Observations

We observe that the interstitial does not show any cross graphene layer diffusion at any of the graphite temperatures simulated. The position of the interstitial is output at every time step of the MD code and the trajectory is analyzed to verify the diffusive nature of the hydrogen isotope transport. Fig.2.3 shows hydrogen interstitial trajectories (in yellow) at different temperatures of the graphite crystal. The view is along the **Z** axis and all atoms having the same color are carbon atoms belonging to the same graphene layer. One can easily identify the hexagonal structures typical of the graphene layer. Diffusion with a short step-size is seen at all target temperatures, with a long step-size diffusion making its appearance at higher temperatures ($\geq 450K$). The H isotope equilibrates with the graphite crystal in a couple of picoseconds. It moves around in the potential well of the vibrating carbon atoms and makes a jump from one potential well to another depending on the migration energy barrier and the graphite temperature. It is seen that typically 100 such jump events occur during the course of a 100 picosecond simulation at $150K$ and more than 400 jumps occur at $900K$. This
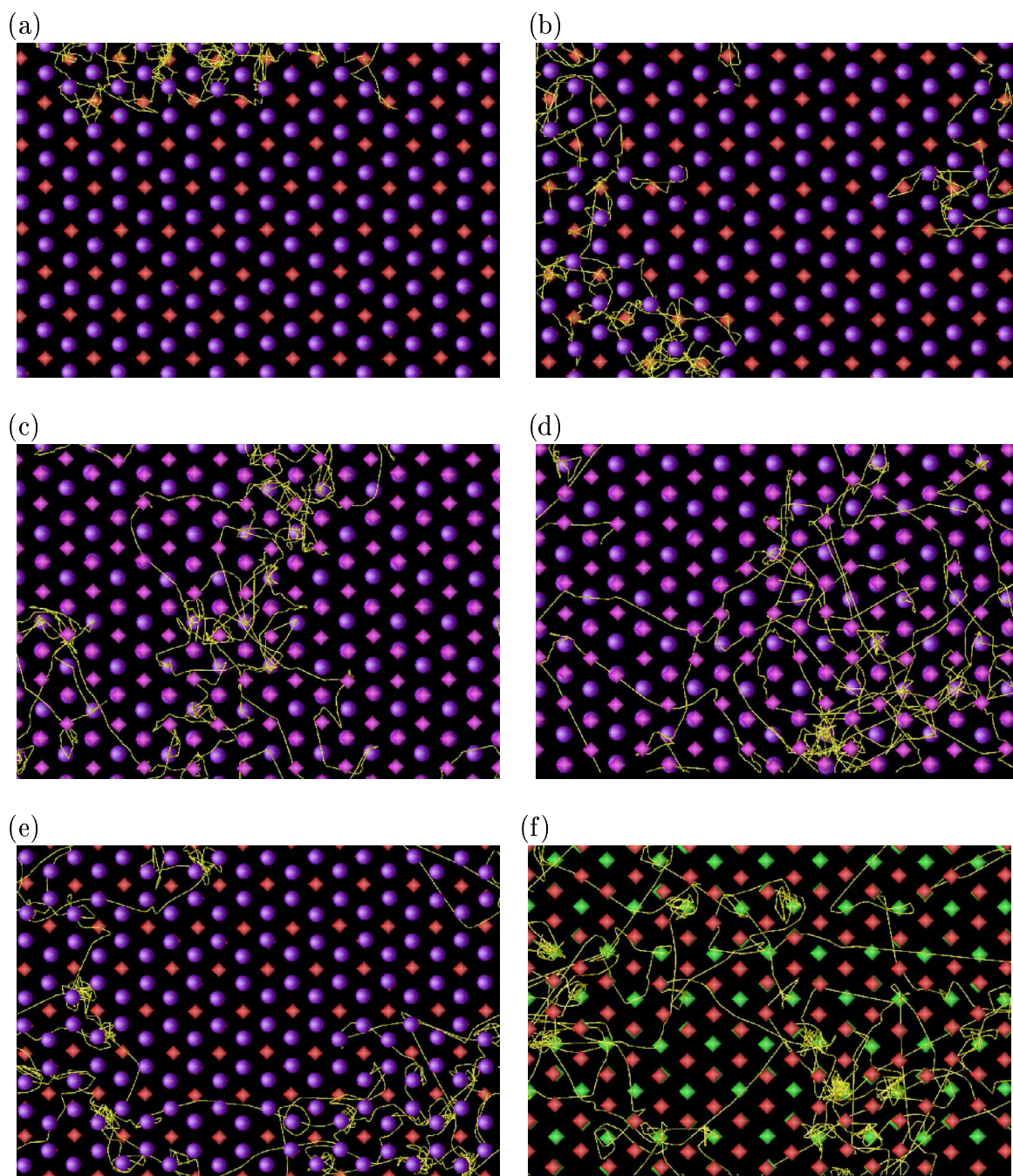
**Figure 2.3:** Interstitial trajectory at (a) 150 K, (b) 300 K, (c) 450 K, (d) 600 K, (e) 750 K and (f) 900 K. from MD

is sufficient to provide equilibration and statistics to analyze the interstitial diffusion in the graphite crystal.

## Analysis

Specifically what is needed for scaling up is to characterize the diffusion in terms of the jump attempt frequency $\omega_o$, the migration energy $E_m$, and the jump distance $L_i$.

$$\omega = \omega_o \, e^{\frac{-E_m}{k_b T}} \tag{2.9}$$

where, $\omega$ is the jump frequency (the frequency with which the interstitial jumps a distance $L_j$ in a specified direction), and $k_B$ is the Boltzmann's constant. Such a characterization assumes that the diffusion is Arrhenius like. With such a characterization one can use Kinetic Monte Carlo (KMC) [71] to simulate diffusion of many atoms over much larger length scales with the same computing resources. A brief introduction to KMC and how we scale up to the next level is described in the next chapter of this thesis.

It is essential to keep in mind that the MD time step is short enough so that the interstitial experiences only a fractional change in potential energy for numerical stability when solving for the force equation. Therefore one can expect the direction of the interstitial to be randomized only after several MD time steps, or equivalently after only a certain length $dr$. For a random walk with equal probability of jumping in any direction the expectation value of the mean square displacement is $N \times dr^2$, where N is the number of jumps. In the simulation, the simulation time is fixed at 100 picoseconds. Therefore, as $dr$ is increased, the number of jumps $N$ (defined as the number of times the interstitial displaces by a distance $dr$) decreases.

Therefore to determine at what value of $dr$ the trajectory is randomized, we plot $N \times dr^2$ as a function of $dr$ for hydrogen, deuterium and tritium (Fig.2.4). The value of $dr$ for which $N \times dr^2$ gets saturated is taken as $L_j$ and the corresponding value of $N$ is used to calculate $\omega$. This analysis is carried out for interstitial trajectories at different temperatures and Eqn.2.9 is used to fit the data to obtain $\omega_o$ and $E_m$. We see that at lower temperatures ($\leq 450K$) a saturation of $N \times dr^2$ is seen at $dr = 2.5$ Å. At higher temperatures, the saturation occurs at larger values of $dr$. Note that the saturation

(i) H interstitials
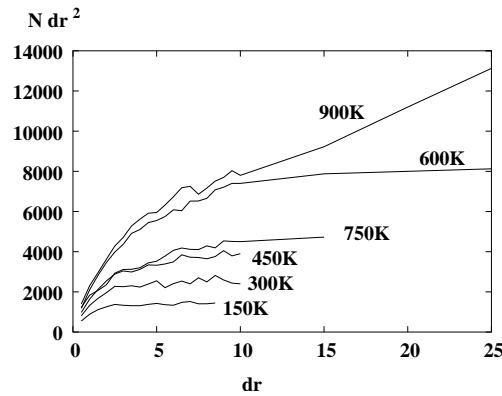


(i) D interstitials
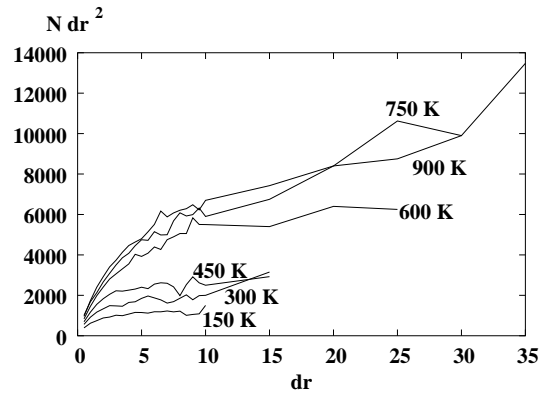


(i) T interstitials
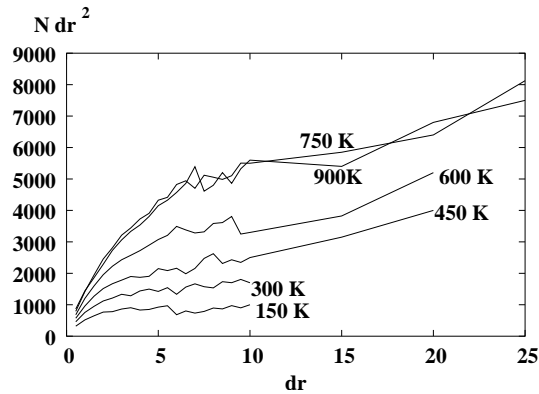


**Figure 2.4:** Variation of $N\ dr^2$ with dr for (i) hydrogen, (ii) deuterium and (iii) tritium

threshold is lower for the 750 K case as compared to the 600 K case. The 900 K case does not saturate at all. This indicates that there are probably two different length scales for the jumps.

The various possible jump paths of an interstitial hydrogen in a graphite crystal is

illustrated in Fig.2.5. The squares and circles represent carbon atoms lying on separate



HB

HAB

HA

(HB + HAB)
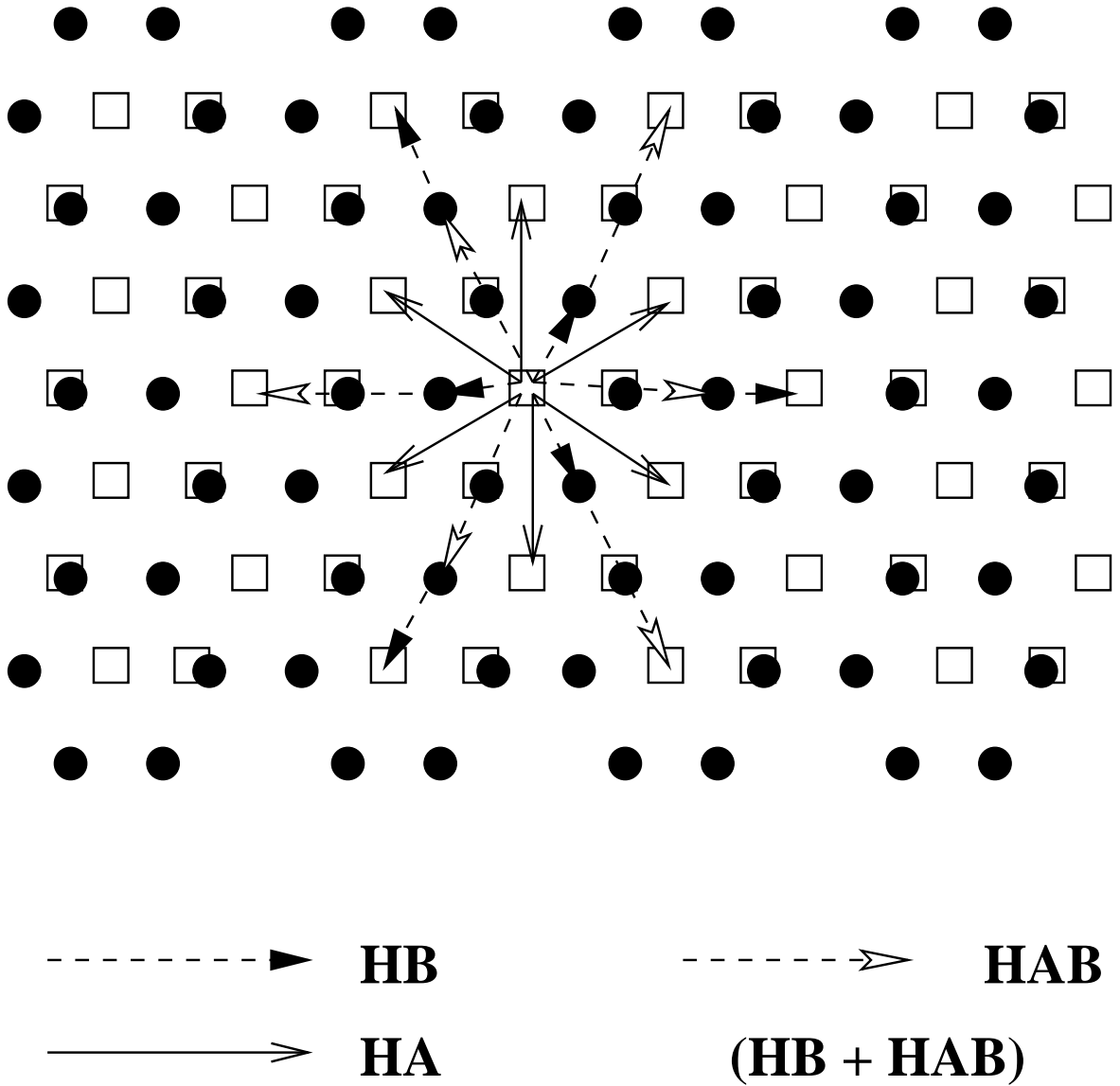
**Figure 2.5:** Various possibilities for interstitial jumps in a graphite crystal

graphene layers which sandwich the interstitial hydrogen atom. The hydrogen atom occupies the large gap between the graphene layers and cannot squeeze through the graphene layer. The lowest energy state for the inter-crystallite seems to lie below the center of the hexagons that constitute the graphene layer. The easiest pathway for diffusion is from below the center of one hexagon to above the center of the neighboring hexagon lying on the opposite graphene layer (denoted by **HB** in Fig.2.5). Another possibility is the jump from below the center of one hexagon to the center of the

neighboring hexagon on the graphene layer (denoted by **HA** in Fig. 2.5). Note that one **HA** jump is achieved with to two consecutive **HB** jumps. Other possibilities for diffusion pathways which have longer step lengths are **HAB** and combinations of the **HB+HAB** types. From our simulations we find that **HB** and **HA** jumps are the main diffusion pathways at low temperatures (Fig. 2.3) below 450 K and that jumps of the type **HAB** and **HB+HAB** start contributing to the diffusion coefficient at temperatures above 450 K (Fig.2.3). These however do not explain the long jumps of 10 Å.

**Parameter fitting**

From the analysis above we have obtained the jump frequency, $\omega$, and typical values of jump sizes, $L$. We note the existence of two different jump lengths, one around 2.5 – 3.5 Å and the other around 10 Å. We also note that hydrogen has enhanced diffusion at $600K$ (Fig.2.4-(i)) and deuterium and tritium have enhanced diffusion at $750K$ (Figs.2.4-(ii) and 2.4-(iii)). These observations have to be made consistent with our need to scale up based on Eqn.2.9. It is seen that a simple Arrhenius fit does not match our MD simulations at different temperatures. Note also the existence of two different slopes in Fig.2.6. Two slopes may not be immediately obvious from the data, but when one takes into account that the data at $600K$ has enhanced diffusion for hydrogen and the data at $750K$ has enhanced diffusion for deuterium and tritium, the effect becomes clear. We therefore conclude that there exists two different migration energies.

Therefore for the numerical fitting we assume a sum of two diffusive processes, with different jump attempt frequencies $\omega_o$, different migration energies $E_m$ and different jump sizes $L$. Therefore four parameters, $\omega_o^l$, $\omega_o^h$, $E_m^l$ and $E_m^h$, have to be fit with 6 data points of jumps per second of $\omega$ observed from our simulations at $150K$, $300K$, $450K$, $600K$, $750K$ and $900K$. Fig. 2.6 shows the fits with the values for the fit parameters given in Table.2.2.

Note that $\omega_o^l$ varies as a function of $\sqrt{m}$, where m is the mass of the interstitial. $\omega_o^h$ is independent of the mass and becomes significant only at temperatures greater than $450K$. When movies of the simulation are made we also observe that phonon vibrations of the graphene layers show a large amplitude at temperatures greater than $450K$ (Fig.2.7). This allows the interstitials to sneak through the larger openings
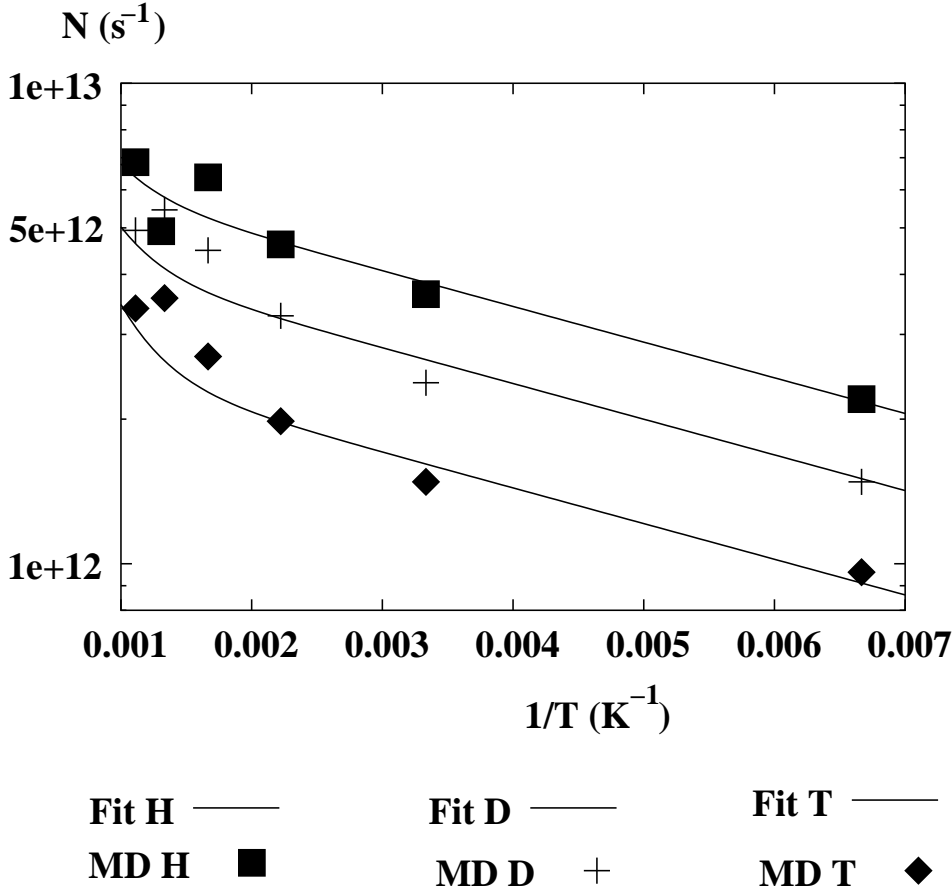
**Figure 2.6:** Sum of two Arrhenius like curves fit to the number of hydrogen isotope interstitial jumps per second as observed from HCParcas simulations

between the graphene layers and at times also surf on the phonon, thereby allowing long jumps $L^h$. We therefore speculate that this branch of diffusion ($\omega_o^h$, $E_m^h$, $L^h$) is due to phonon vibrations in graphite wherein the randomly moving particle can pass through potential well gaps created by the large amplitude phonon vibrations. The enhanced diffusion of hydrogen at $600K$ and of deuterium and tritium at $750K$ could be due to synergistic interactions of the interstitials with phonons. However, this is speculation and further analysis is required.

## 2.3  Summary

We have studied the diffusion of hydrogen isotopes in crystalline graphite. We see that there exist two channels for diffusion and represented these as trapping–detrapping processes with characteristic jump attempt frequencies, migration energies and jump

Table 2.2: Fitting parameters to parametraze hydrogen isotope diffusion

| Isotope | $E_m^l$ (eV) | $\omega_o^l$ $(10^{12}s^{-1})$ | $E_m^h$ (eV) | $\omega_o^h$ $(10^{13}s^{-1})$ |
|---------|--------------|-------------------------------|--------------|-------------------------------|
| hydrogen | 0.0147 | 6.8 | 0.269 | 2.7 |
| deuterium | 0.0147 | 4.7 | 0.269 | 2.7 |
| tritium | 0.0147 | 2.8 | 0.269 | 2.7 |

lengths. We see that the isotopes do not diffuse across the graphene layers and that the diffusion is isotropic in the plane of the graphene layer.

Other interesting studies beyond the scope of this thesis are:

- Saturated hydrogen isotope diffusion in crystal graphite,

- Trace and saturated hydrogen isotope diffusion in damaged crystal graphite,

- The above two kinds of diffusion in crystal graphite with open boundary conditions,

- In reality the edges of the crystallites may contain open bonds or SP2-SP3 mixtures of bonds. This can be investigated and hydrogen isotope transport and trapping probabilities at the edges of such crystallites can be studied.

These studies require major modeling effort and will bog us down at length scales of nanometers and time scales of a few hundred picoseconds. The main aim of this study is to develop a general multi–scale code by identifying parameters at lower scales that can be used to model the problem at higher scales. This will be demonstrated in the next chapter for hydrogen isotope diffusion in crystalline graphite, and is a continuous process that gets repeated for different parameters at the different scales.

(a)
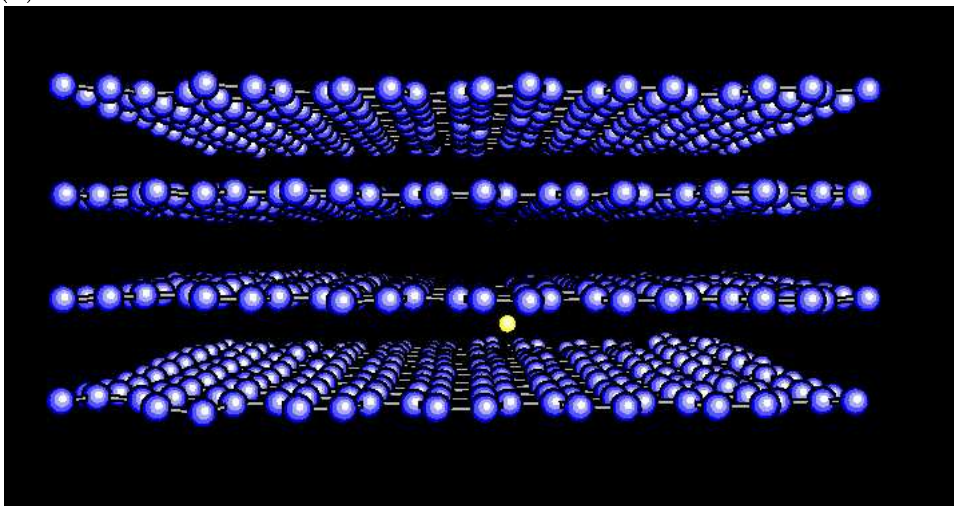


(b)



**Figure 2.7:** Figure showing typical phonon vibrations at (a) 450 K and at (b) 900 K

# Chapter 3

# Kinetic Monte-Carlo simulation: Parametrization of MD

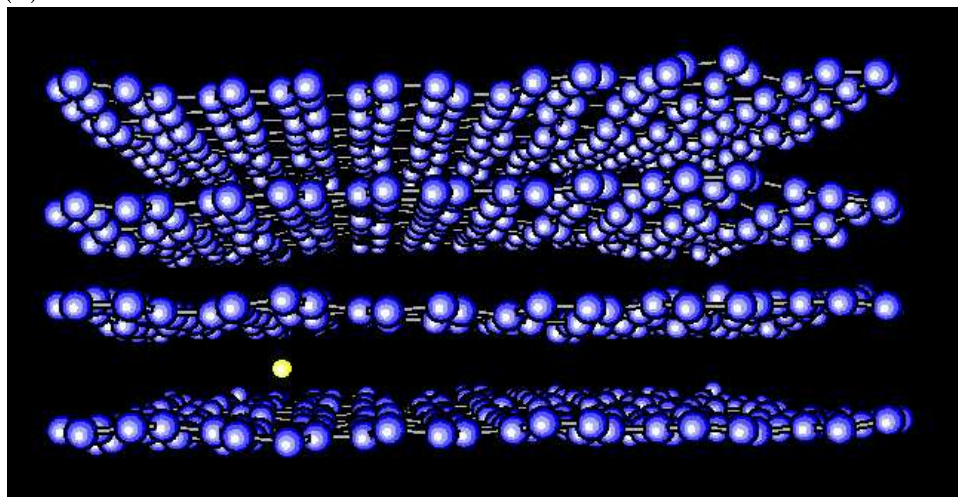There exist various methods to overcome the limitations of MD (see [72] for a review of these methods). Molecular dynamics gives a microscopic insight into the physical process of diffusion of a hydrogen isotope in crystalline graphite as we have seen in the previous chapter. The hydrogen isotope vibrates in a potential well formed by the vibrating carbon atoms and wanders in the XY plane which is the plane parallel to the graphene layers (Fig.2.3). During the vibrations it exchanges energy with the vibrating carbon atoms around it. At some point in the simulation, due to interaction with its neighboring atoms, it gains enough energy to exit the potential well it is trapped in and enters a new potential well at a new location within the graphite crystal. Most of the simulation time is spent in these vibrations in a potential well. Note that the hydrogen isotope also loses information about its entry pathway into the potential well within a few vibrations. Its exit route from the potential well is independent of its entry path. This implies that each consecutive jump is independent of its past history. Therefore if we can reformulate the above diffusion phenomena as probabilities for jumping out of the potential traps, with probable lengths and directions for the jumps, we can scale up a lot in the time and in the number of particles simulated using Kinetic Monte–Carlo (KMC) [71].

In the next section the ideas behind KMC are presented along with the algorithm we use [73]. KMC uses the insights gained from MD and does not have the limitations on the number of particles or on the time that can be simulated as in MD.

The parametrization of the MD results within the KMC model is described and the results are compared. Finally a simple model for the diffusion of hydrogen isotope in crystalline graphite is presented which matches the KMC and the MD results.

# 3.1   Brief introduction to Kinetic Monte–Carlo simulations

Dynamics of a N body problem can be simulated by transiting through the various successive states of the system, denoted by $\sigma$. $\sigma$ is characterized by the positions and velocities of the individual particles that constitute the system. This transition can be represented by the equation (widely known as the Master equation)

$$\frac{\partial P(\sigma, t)}{\partial t} = \sum_{\sigma'} W(\sigma' \to \sigma) \, P(\sigma', t) - \sum_{\sigma'} W(\sigma \to \sigma') \, P(\sigma, t) \qquad (3.1)$$

where $\sigma$ and $\sigma'$ are successive states of the system, $P(\sigma, t)$ is the probability that the system is in state $\sigma$ at time $t$, and $W(\sigma' \to \sigma)$ is the probability per unit time that the system will undergo a transition from state $\sigma'$ to state $\sigma$. Usually, Monte–Carlo methods are employed to explore the various states of such a system in order to find the most probable minimum energy state at equilibrium. This can be done by setting the LHS of Eqn.3.1 to zero and exploring various states of the system without really bothering about the dynamical transition from one state to another. However, in order to give a dynamical interpretation for the transitions, criteria for the transition probabilities are necessary.

## 3.1.1   Criteria for dynamic Monte–Carlo simulation

Fichthorn and Weinberg [71] established that Monte–Carlo simulations can be used to simulate the dynamics of a Poisson like process if

- Transition probabilities are created such that a dynamical hierarchy of transition rates to correctly model the microscopic barrier crossings (events) is established;

- Detailed balance is satisfied at equilibrium, which means that all the equally probable eigen states of a system at equilibrium can be accessed with the same probability;

- The various events are independent, and

- Time increments are calculated appropriately as defined by [71].

$$\Delta t \; = \; -\frac{\ln(U)}{\sum_i n_i r_i} \qquad (3.2)$$

where, $n_i$ is the number of atoms capable of undergoing a transition labeled $i$, $U$ is a uniform random number between zero and one, and $r_i$ the transition rate.

The above criteria becomes clear when applied to our problem. Suppose we have $N$ hydrogen interstitials distributed inside various crystallites of a graphite sample. We know from our MD simulations that these can diffuse in the crystallites with two different kinds of jumps described by their jump frequencies, migration energies and jump distances ($\omega_o^{l,h}, E_m^{l,h}, L^{l,h}$). Therefore there are $2N$ transitions possible and the transition rates have to occur such that the microscopic barrier crossings are correctly implemented consistent with the probabilities of various jump events. This is done using the BKL algorithm [73] described in the next paragraph. Detailed balance would mean that if we initially assign a Gaussian distribution for the atoms, at equilibrium the interstitials will be uniformly distributed if periodic boundary conditions are specified. We have seen from our MD simulations that a particle jumping out of a potential well has lost all knowledge of where it entered the potential well. This implies that the jumps are independent. Finally the time step after each transition must be incremented as per Eqn.3.2. In this case there are two transitions possible for each of the N atoms, either a low frequency jump or a high frequency jump with the transition rates given by Eqn.2.9. Therefore $\Delta t$ in this case will be $\frac{-ln(U)}{2N(\omega^l+\omega^h)}$.

## 3.1.2 The Bortz–Kalos–Lebowitz algorithm

This subsection is based on Kai Nordlund's notes on the BKL Algorithm, and explained briefly using the above example of $N$ interstitials in crystalline graphite.

(i) **Initialize the system at time $t = 0$. i.e set up distributions of the interstitials at $t = 0$.**

(ii) **Loop depending on time to be simulated or number of KMC steps to be simulated.**

(iii) **Form a list of all rates $r_j$ in the system. i.e calculate $r_l$ and $r_h$.**

(iv) **Calculate the cumulative function**

$$R = \sum_i R_i = \sum_j n_j r_j$$

$j$ **is the number of different jumps possible** $(= 2$ **in our example) and** $i$ **is the total number of possible transitions of the system** $(= 2N$ **in our example)**

(v) **Get a uniform random number** $U \in [0, 1]$.

(vi) **Find the event to carry out,** $i$ **by finding the** $i$ **for which**

$$R_{i-1} \;<\; UR \;<\; R_i$$

(vii) **Carry out event** $i$.

(viii) **Get a new uniform random number** $U \in [0, 1]$

(ix) **Update the time with**

$$t \;=\; t \;+\; \Delta t$$

**where**

$$\Delta t \;=\; -\frac{\ln(U)}{R}$$

**and update the KMC step count.**

(x) **Check for end of loop and either go to step (ii) or end.**

## 3.2    Hydrogen isotope diffusion in crystalline graphite

A KMC code (DiG for Diffusion in Graphite) was developed to study the diffusion of interstitials in graphite. It is written in a modular fashion to make addition of new species, new interactions, etc., easy. The values of $\omega_o^l$, $E_m^l$, $L^l$, $\omega_o^h$, $E_m^h$ and $L^h$ obtained from the MD simulations were used to study the diffusion of hydrogen isotopes in pure, crystalline graphite.

## 3.2.1 Inputs and setting up the simulation

A graphite crystal of size $500 \times 500 \times 500$ Å$^3$ was used with periodic boundary conditions. 1000 atoms of the interstitial species were uniformly distributed within this volume. The simulation was carried out for 100000 KMC steps which implies that each particle has on average undergone 100 jumps. The diffusion coefficient in these cases is again calculated using Eqn.2.8 averaged over the mean square displacements of the 1000 particles. The simulation is repeated 100 times to see the variance of the calculated result which was always less than 0.01.

The inputs to the code are obtained from fits to our MD simulations (Table.2.2). Two types of simulation were carried out, one with a constant jump size $L^l$ and $L^h$, and the other with a varying jump size to model the enhanced diffusion seen at 600 K ($1/T = 0.0017$ K$^{-1}$) in the case of hydrogen (Fig.2.4-(i)) and 750 K ($1/T = 0.0013$ K$^{-1}$) in the case of deuterium and tritium (Fig.2.4-(ii), Fig.2.4-(iii)). The directions of the jumps were chosen assuming equal probability in the 2D plane parallel to the graphene layers.

## 3.2.2 Results

In Fig. 3.1 we compare the values for the diffusion coefficient obtained from our KMC simulations (using **DiG**) with the values obtained from the MD simulations (using **HCParcas**) for hydrogen diffusion in pure crystalline graphite. For the constant jump size simulations we find that 3.8 Å for $L^l$ and 10 Å for $L^h$ gives the best results. In the varying jump size simulations, the jump sizes were also adjusted at other graphite temperatures to match the MD results better in accordance with the MD analysis in Chapter.2. This gives us a good parameter set in ($\omega_o^{l,h}, E_m^{l,h}, L^{l,h}$) when we scale up.

Fig.3.2 plots the diffusion coefficients of hydrogen ($D_H$), deuterium ($D_D$) and tritium ($D_T$) as obtained from the KMC simulations as a function of inverse temperature ($1/T$). These simulations belong to the varying jump size category and therefore the enhanced diffusion at 600 K for hydrogen and 750 K for deuterium and tritium shows up in the figure.
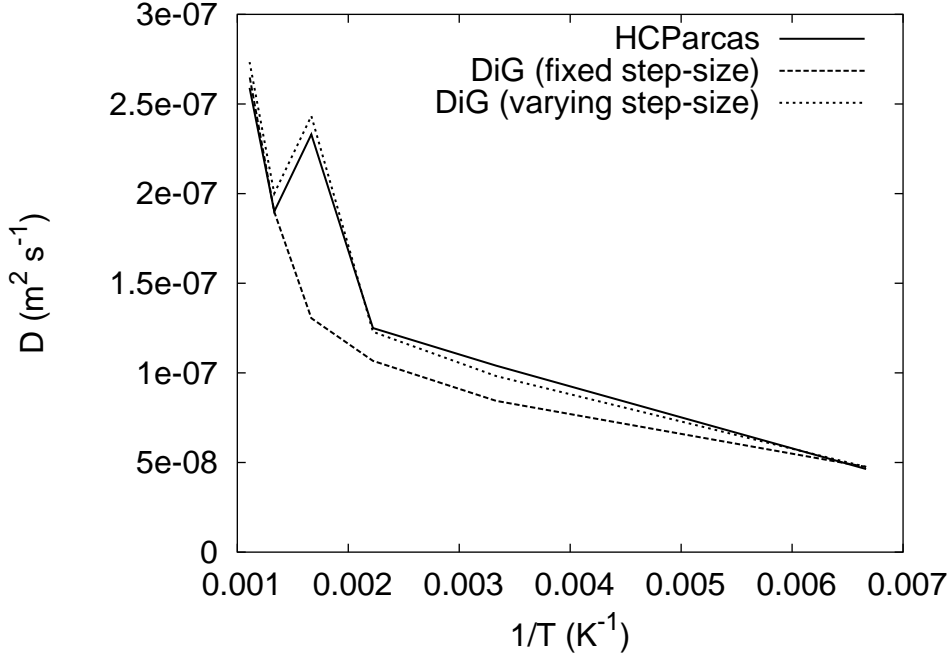
**Figure 3.1:** Diffusion coefficient of hydrogen interstitial in pure crystalline graphite: Comparison of KMC with MD

## 3.3   Simple model for H isotope diffusion in crystalline graphite

From the above results it is clear that our parametrization of the MD is quiet good and our assumption of isotropic jumps in the 2D graphene plane also holds. Therefore we have a 2D random walk with known probabilities for two different kinds of jumps. We can also assign a probable time for each jump. We are therefore encouraged to create the following analytical model based on the above assumptions and parameters.

A particle gets trapped with two possible trap energies $E_M^l$ and $E_M^h$. The particle attempts to jump out of the traps with frequencies $\omega_o^l$ and $\omega_o^h$. Assuming that the jumps are a Poisson like process, the two types of jumps occur with a typical frequency of

$$\omega^{l,h} \;=\; \omega_o^{l,h} \; e^{\frac{-E_m^{l,h}}{k_B\,T}} \tag{3.3}$$

The probability of a jump of type $\binom{l}{,}{}^h$ occurring is given by

$$P^{l,h}(L^{l,h}) \;=\; \frac{\omega^{l,h}}{\omega^l \;+\; \omega^h} \tag{3.4}$$
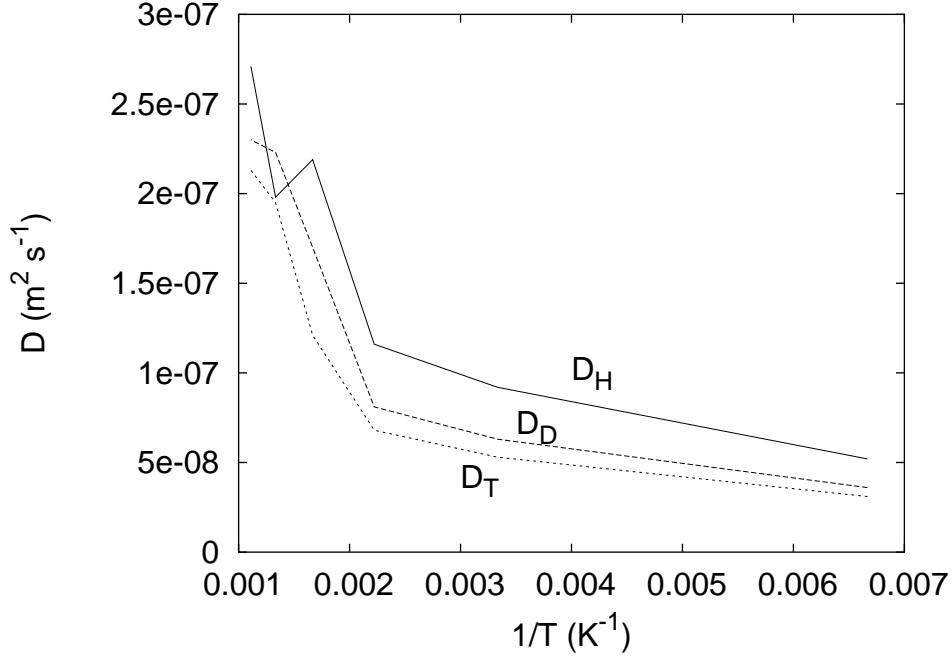
**Figure 3.2:** Comparison of diffusion coefficients of hydrogen isotopes in pure crystalline graphite, obtained from the KMC simulations

where $L^{l,h}$ is the length of a jump for a $^{l,h}$ type of jump. Assuming a simple random walk in 2D (in-between the graphene planes), the mean square displacement after $N$ steps is

$$< (R(t) - R(0))^2 > = N [P^l (L^l)^2 + P^h (L^h)^2] \qquad (3.5)$$

The time increment for each jump event is given by [71]

$$\Delta t = -\frac{ln(U)}{\omega^l + \omega^h} \qquad (3.6)$$

where $U$ is a uniform random number between 0 and 1.

Using Eqns.3.5 and 3.6 and Einstein's relation (Eqn.2.8), we get the diffusion coefficient of hydrogen isotope in crystalline graphite as

$$
\begin{aligned}
D &= \frac{1}{2\,d} \frac{< (R(t) - R(0))^2 >}{\Delta t} \qquad (3.7) \\
&= \frac{N}{4} \frac{\omega_o^l\, e^{\frac{-E_M^l}{k_B\,T}}\, (L^l)^2 + \omega_o^h\, e^{\frac{-E_M^h}{k_B\,T}}\, (L^h)^2}{\sum_i^N (-\,ln(U_i))}
\end{aligned}
$$

## 3.4   Discussion of results

A simple program was written to implement Eqn.3.7. The input parameters for $\omega_o^{l,h}$ and $E_M^{l,h}$ were the same as those used in the KMC simulations. A value of 10 Å was used for $L^h$, and a value of 3.8 Å was used for $L^l$ except for

- 600 K for hydrogen where $L^l = 4.8$ Å,

- 600 K and 750 K for deuterium where $L^l = 5.0$ Å,

- 600 K where $L^l = 4.5$ Å and 750 K where $L^l = 5.0$ Å for tritium.

The diffusion coefficients obtained from HCParcas, DiG and the simple model are shown in Fig.3.3 for hydrogen, deuterium and tritium. It is seen that the simple model reproduces the results for hydrogen isotope diffusion qualitatively and quantitatively (up to a factor of 2) in the temperature range studied, demonstrating that the key elements for this process is understood.

## 3.5   Characterization of the jump trajectories

In the analysis of the MD trajectories in the previous chapter we see that the product $N \times dr^2$ does not saturate for the 900 K case for hydrogen interstitial (Fig.2.4-(i)), for the 750 K and 900 K cases for deuterium interstitial (Fig.2.4-(ii)), and for temperatures above $450K$ for the tritium interstitial (Fig.2.4-(iii)) diffusion. This means that the trajectory represented as a random walk is not exactly diffusive.

In a paper titled, "Beyond Brownian motion" [74], J. Klafter et. al. talk about random walk processes that are *sub−diffusive* (wherein the trajectory results in a mean squared displacement that shows slower−than−linear growth with time), and *super−diffusive* (wherein the trajectory shows faster−than−linear growth of the mean squared displacement with time). They give the example of a 2-D random walk where step lengths of size 1, $b$, $b^2$, .... and so on are allowed with the longer jumps having an order of magnitude (in $\lambda$) less probability of occurring, with $b > \lambda > 1$. Such random walks are called Lévy flights and can show super−diffusive behavior with infinite variance (read mean square displacement) and their trajectories show self similar patterns characteristic of fractals (for example, figure 1 of [74]) and such phenomena have been noticed in simulations of adsorbed gold nanoclusters on the basal plane of graphite [75]

(i) Hydrogen diffusion in crystalline graphite.
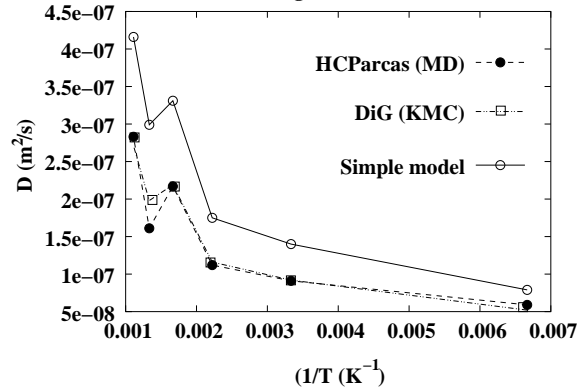


(ii) Deuterium diffusion in crystalline graphite.
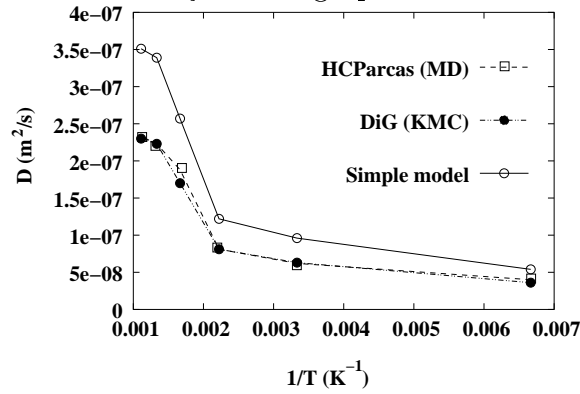


(iii) Tritium diffusion in crystalline graphite.



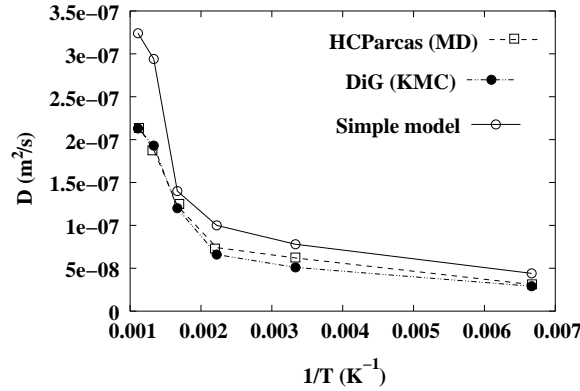**Figure 3.3:** Comparison of hydrogen isotope diffusion in crystalline graphite using MD, KMC and a Simple model

and in a wide range of physics issues ([74] and references therein). In physical systems there do not exist infinite number of length scales for jumps and a class of stochastic processes called truncated Lévy flights (TLF) are defined, wherein the arbitrary large steps of a Lévy flight are eliminated [76].

In our random walk problem above we see two different scale lengths for the jumps $L^l$ and $L^h$, occurring with probabilities $P^{l,h}$ given by Eqn.3.4 and plotted in Fig.3.4. However in our MD simulations there exist three length scales for the interstitial tra-
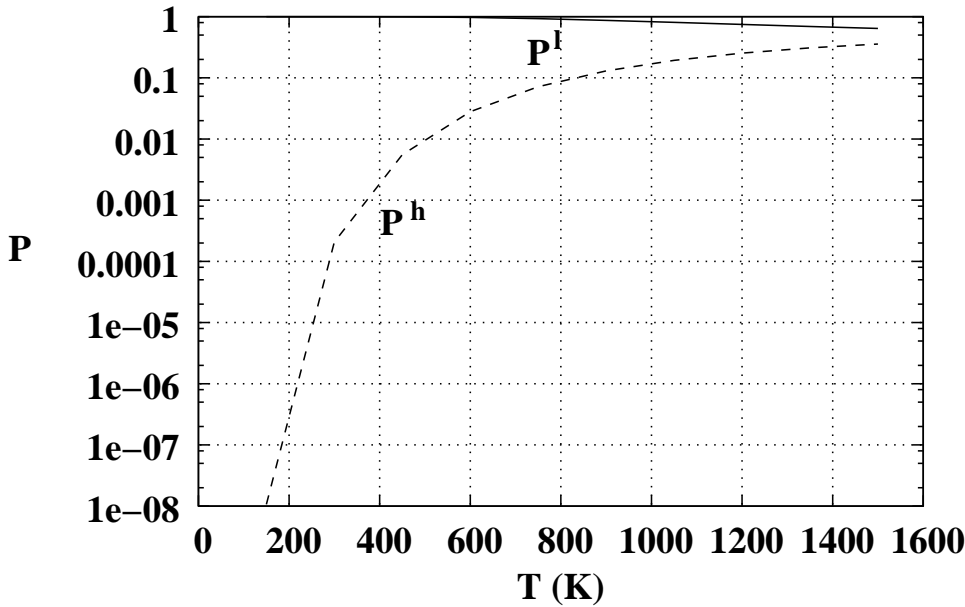


**Figure 3.4:** The jump probabilities corresponding to a short jump $P^l$ and a long jump $P^h$ for hydrogen isotopes in crystalline graphite

jectory:

- The smallest length scale being the amplitude of the random vibrations in a potential well which is $\sim$ Å.

- The next higher length scale being the short jumps defined by $L^l$.

- The largest length scales are the long jumps $> L^h$ observed at temperatures greater than $450K$.

The equivalent KMC simulation, and our simple model, do not have the smallest length scales. We also see super–diffusion like characteristics (Fig.2.4-(i), Fig.2.4-(ii) and Fig.2.4-(iii)) at some higher temperatures where it is possible to have a few large scale jumps within the simulation time. From the above considerations and from Fig.3.4 it is possible that the hydrogen isotope trajectories have Lévy flight characteristics.

A program implementing the box counting method [77] is used to calculate the dimension of the diffusing isotope trajectory as obtained from (i) MD simulation, and (ii) from the simple model. A plot of the factorial dimension is shown as a function of the graphite crystal temperature in Fig.3.5 for the MD runs and the simple model. $\rho$ is the ratio of $L^l$ to $L^h$ used in the the simple model. Note that the value of the dimension lies between 1.3-1.6 in all cases.
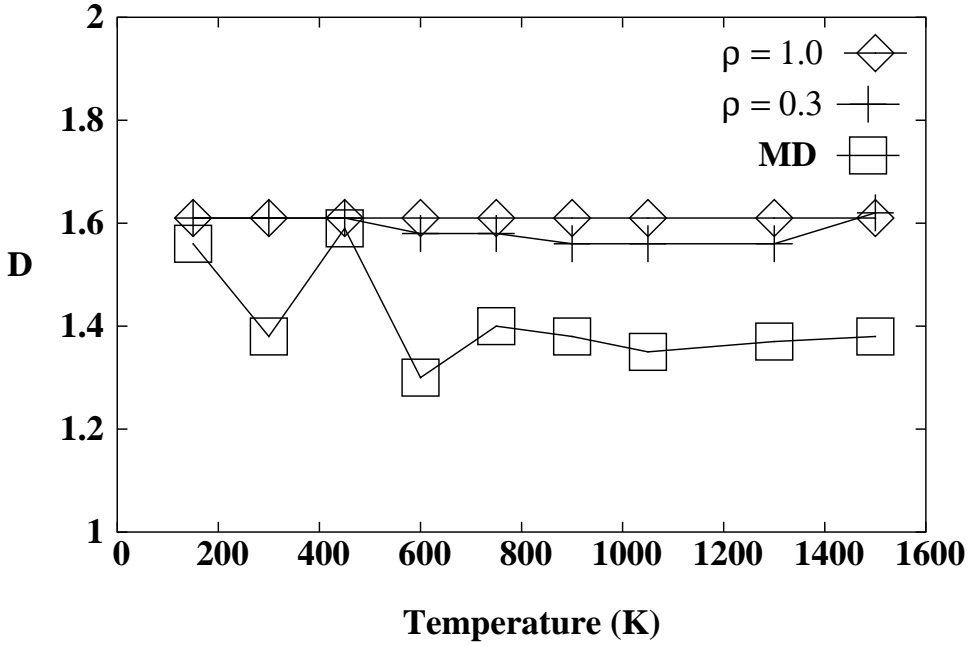


**Figure 3.5:** The box-counting-dimension of hydrogen isotope trajectories in crystalline graphite

## 3.6   Summary and outlook

We have modeled the MD results for hydrogen isotope diffusion in crystalline graphite using KMC and as a simple 2-D random walk using the information $(\omega_o^{l,h}, E_m^{l,h}, L^{l,h})$ obtained from MD. This is already a scaling up since our KMC model treats the diffusion of thousands of particles (within the trace particle diffusion approximation) over any realistic size of crystalline graphite containing millions of carbon atoms. We show that the isotope trajectories in crystalline graphite have a fractional dimension lying between 1.3 and 1.6.

The model developed in this chapter is scalable to macroscopic system sizes. However, in reality graphite micro–crystals have a typical size of $50 - 100$ Å in PFMs.

Additional physics mechanisms like trapping/detrapping at traps, recombination, dissociation, etc of the hydrogen isotopes must be added. In order to scale up, we must now include the realistic structure of porous graphite. In the next chapter we describe an algorithm to generate a porous graphite structure with granules, voids, crystallites and microvoids and extend the model to simulate trans–granular –diffusion of hydrogen isotopes.

# Chapter 4

# Trans–Granular–Diffusion: Scaling up to microns

In this section we first describe how we scale up to study hydrogen isotope diffusion across a granule of graphite which is a few microns in size. As described in the introduction of the thesis, graphite consists of micron sized granules separated by voids which are a fraction of a micron. A granule consists of graphite crystallites which are a few nanometers in size oriented randomly, separated by microvoids which are a fraction of a nanometer in size. Therefore, except for the orientation of the crystallites, the general structure is the same at different scales. In this chapter an algorithm for setting up a general, porous geometry in 3D is described. A model for hydrogen transport in a granule is proposed and the KMC code DiG is extended to model trans–granular–diffusion (TGD). The results for hydrogen isotope diffusion in a typical granule of graphite are presented and compared with the results from experiments [35]. Finally, a simple model is presented which incorporates the essential physics and reproduces the results.

## 4.1 General algorithm for producing a 3D porous structure

An algorithm to generate a 3-D rectilinear parallelepiped with a specified void fraction and sub–structures having random shapes separated by gaps (voids/microvoids) is presented. It also allows for random orientation of the sub–structures (to model

crystallites). The average size of the sub–structures and their smoothness can also be varied.

### 4.1.1    Underlying philosophy

The idea behind the algorithm is the one presented by Graziani [49] for creating mixtures of alloys. For a given volume, a Poisson distribution is used to specify a sub–structure *element* that has a random shape and a mean width denoted by *element–size*. *Elements* are created by populating basic blocks called *cells*. The smoothness of the *element* depends on the *cell–size*. If the sub–structures are crystallites, random orientations are also specified. After each such populating event the remaining void fraction is checked. The process is repeated if the void fraction is greater than required.

### 4.1.2    Algorithm used

The algorithm used is described below:

(i) **Reading in inputs**. The Void fraction (VoidFrac), length of the system along X,Y,Z, (Lx,Ly,Lz), mean dimensions of the sub-structure (ELx, ELy, ELz), basic cell size (CellSizex, CellSizey, CellSizez) and the smoothness of the sub-structure (SmoothY, SmoothZ), Typical crystallite orientations (Euler angles [78] (Theta, Phi, Psi)) and variation within this typical orientation (dTheta, dPhi, dPsi) are input.

(ii) **Initializing various parameters in the simulation**. The number of cells along X (nx), Y (ny) and Z (nz), the total number of cells (TotalCells), the number of cells occupied (NumOccupied=0), and the Occupied fraction (OccFrac=0) and flag indicating whether a cell is occupied or not (OccFlag=1 or 0) are initialized. Memory allocation is carried out.

(iii) **Picking up a random point within the system to populate**. Uniformly distributed random numbers are used to pick up a random point (Px, Py, Pz) within the rectilinear parallelepiped.

(iv) **Constructing the sub-structures**. A Poisson random number distribution with a mean corresponding to the sub-structure dimensions along with a selection process to maintain the required smoothness is employed around the point P (Px, Py, Pz). The algorithm for doing this is:

- **Scanning substructure along X (i)**. Generate a random number following the Poisson probability distribution with a mean corresponding to the sub-structure size along X (iel).

- **Scanning substructure along Y (j) while traversing cells along X**. Loop over Px-0.5*iel to Px+0.5*iel generate a random number following the Poisson probability distribution with a mean corresponding to the sub-structure size along Y (jel), at each increment along X. If the value of jel is within the smoothness percentage specified (SmoothY) accept it, else regenerate jel.

- **Scanning substructure along Z (k) while traversing cells along Y**. Loop over Py-0.5*jel to Py+0.5*jel generate a random number following the Poisson probability distribution with a mean corresponding to the sub-structure size along Z (kel), at each increment along Y. If the value of kel is within the smoothness percentage specified (SmoothZ) accept it, else regenerate kel.

- **Constructing the substructure**. At each cell defined by (i,j,k) check occupancy. If not it is not occupied, occupy it (OccFlag = 1) and also provide an orientation (if input flag so dictates) and keep track of the number of cells occupied (increment NumOccupied). the deviation from the orientation is specified again by a Poisson distribution.

(v) **Checking for the void fraction and stopping the program**. Check if the fraction of voids is greater than the specified void fraction. If yes, pick a random point within the system, check that it is unoccupied and build a substructure as in point (iv) above. If not store the structure in arrays or in a file and exit.

Fig.4.1 shows a porous graphite structure of a micron sized cube created with the above algorithm using an mean *element–size* of $10^{-7}$ meters and a mean *cell–size* of $10^{-8}$ meters.

## 4.2 The trans–granular–diffusion model

We have seen in the previous chapter that the diffusion of hydrogen isotopes in crystalline graphite can be represented by the parameter set $(\omega_o^{l,h}, E_m^{l,h}, L^{l,h})$ within a KMC scheme. In our TGD model (Fig.4.2), we use these parameters to model transport in
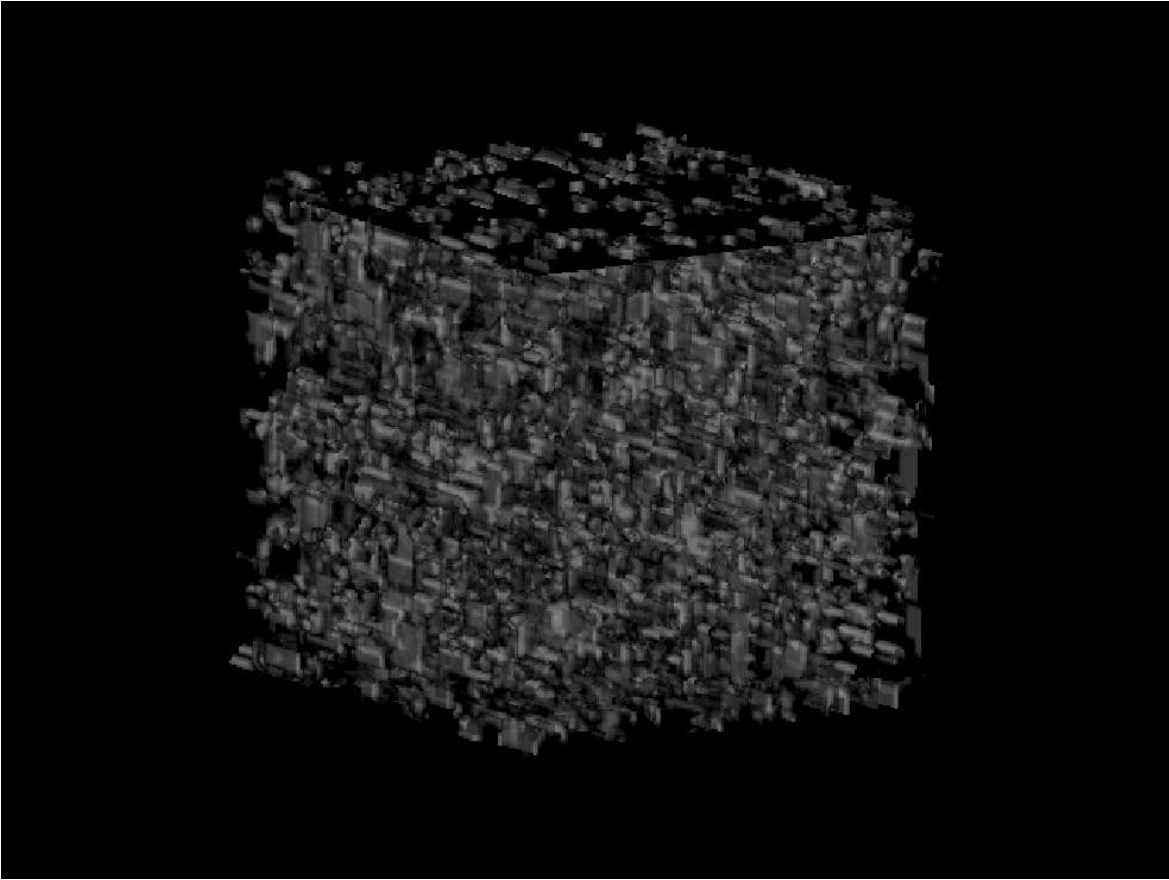
**Figure 4.1:** Porous Graphite structure created using the algorithm described in Section.4.1.2

the crystallites. The transport in the microvoids is modeled by specifying a trapping probability for the interstitial as it passes from the crystallite region to the microvoid region. These atoms get detrapped within the KMC scheme with a detrap attempt frequency $\sim 1 \times 10^{13}$ $s^{-1}$ which is a typical phonon frequency, and a detrapping energy (between 2.6 and 4.3 eV) taken from literature [35]. The detrapped atoms initially take a random 3D step. If this step takes it into a microvoid, it continues its flight until it comes in contact with a crystallite where it again has a probability of getting trapped. If the step takes it into a crystallite it then diffuses into the graphene plane of the crystallite. We look only at the regime where the graphite granule is unsaturated and the diffusion is limited by the trapping and detrapping at microvoids.
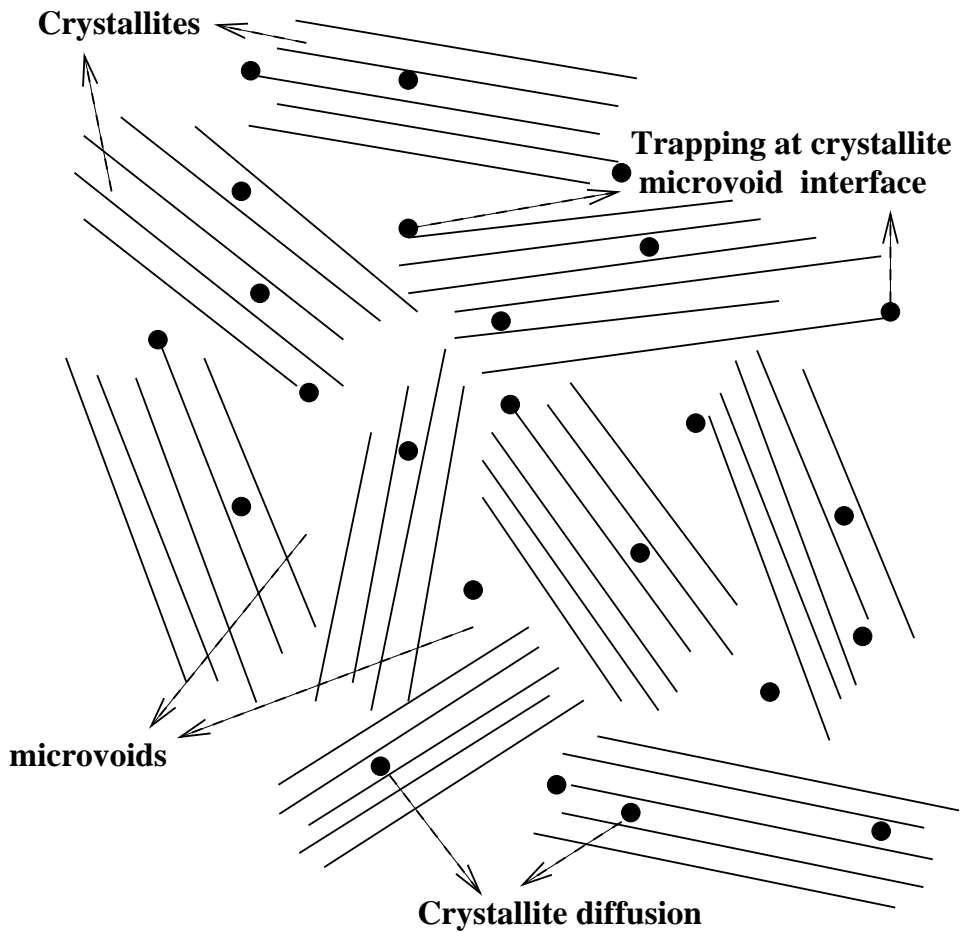
**Figure 4.2:** Trans–Granular–Diffusion model schematic

## 4.3   Code adaptations

The main addition was inclusion of the porous trans–granule geometry using the algorithm described in section 4.1.2. The above model includes a new rate (detrapping at crystal–microvoid interface) which has to be incorporated in the KMC algorithm. Functions to transform to and from the simulation axes to crystallite orientations using Euler transformations [78] are added so as to carry out diffusion parallel to the graphene layers.

From the programming aspect particle positions are kept track of with respect to the porous structure and appropriate transport models implemented depending on the region (crystal or microvoid) the particle lie in. Transitions between regions are noted and trapping probabilities are implemented at the interfaces.

## 4.4   TGD simulations

### 4.4.1   Inputs and setting up the simulation

Simulations were done at $750K$, $1000K$, $1250K$, $1500K$ and $1750K$. The porous structure was generated for a cube of size $5 \times 10^{-8}m$, with an *element–size* corresponding to typical crystallite sizes in graphite of $5 \times 10^{-9}m$ and a minimum *cell–size* of $5 \times 10^{-10}m$, with two different void fractions 10% and 20%. The crystallite orientations were fixed by the Euler angles $\Phi = 30°$, $\Theta = 45°$ and $\Psi = 20°$. A smoothness percentage of 5% is specified for the structure. The orientations were allowed to vary by a mean value of 2°. Note that these parameter choices allow for resolution of details of the granule micro–structure like micro–voids and crystallites and results in a sample of the granule consisting of 1000 crystallites. Periodic boundary conditions are applied in all three directions, thereby effectively simulating an infinite solid.

For interstitial transport in crystallites, the parameter set obtained from the MD simulations ($\omega_o^{l,h}$, $E_m^{l,h}$, $L^{l,h}$) for hydrogen and deuterium is used. Trapping probabilities at the crystallite–microvoid interfaces is taken to be 1. The trapping energies $E_t$ were taken from literature [35] to lie between $2.6eV$ to $4.3eV$ and the detrap attempt frequency was taken as $\omega_o^t = 1 \times 10^{13}$ $s^{-1}$, which corresponds to a typical phonon frequency in graphite [39]. The simulation was carried out for 100 particles uniformly distributed in the sample, for 100000 BKL steps and repeated for 100 trials. Simulations with a larger number of BKL steps ($10^6$) were carried out for a few cases to check if there is any change in the results for the diffusion coefficient.

### 4.4.2   Results at the mesoscopic length range

We observe that the diffusion in the crystallite is fast compared to the diffusion in the granule as a whole. This is mainly because of the low values of $E_m^h$ and $E_m^l$ for crystallite diffusion compared to the detrapping energies ($\sim 2.6 - 4.3$ eV) of the interstitials trapped at the crystallite–microvoid interfaces. This, coupled with the fact that the interstitials get trapped every time they cross over the crystallite–microvoid interface, make the simulations fall in the trapping/detrapping limited regime of diffusion. In this limit the diffusion coefficients of the different hydrogen isotopes are similar. This is because the detrapping energy and the phonon frequencies of graphite are unchanged. The diffusion coefficients we obtained lie in the experimental range (Fig. 13 of [35])

Fig.4.3.
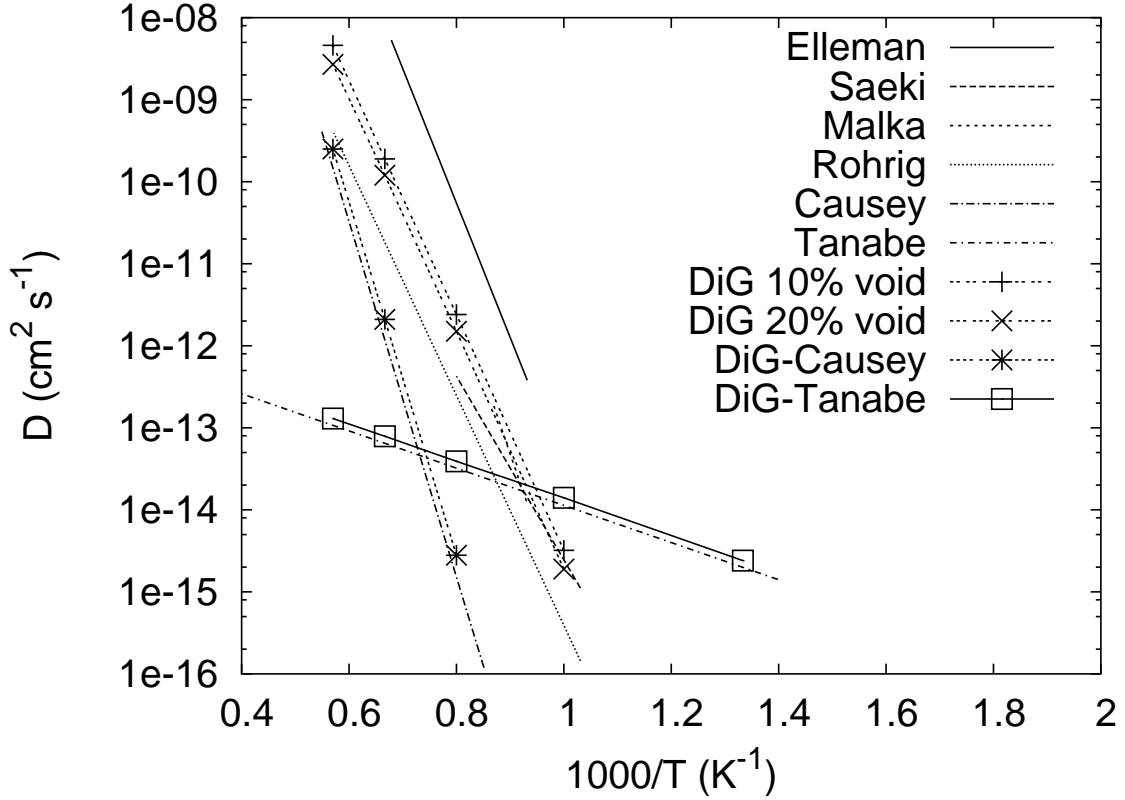


**Figure 4.3:** Comparison of TGD coefficients from the the KMC simulations with experimental values for the diffusion coefficient

We also see that by increasing the void fraction the diffusion coefficient decreases. This is because we kept the element size constant when creating the porous granule structure. Therefore we have similar sized crystallites and microvoids, but the particle covers shorter distances before it gets trapped in the granules with a higher void fraction. This is easily understood from Fig.4.4. where **A** illustrates an object with $\sim 10\%$ voids and **B** and **C** illustrates an object with $\sim 20\%$ voids. In case **B** a particle would travel shorter distances before getting trapped at the microvoid–crystallite interfaces as compared to case **A**. In Case **C** the particle would travel larger distances before getting trapped at a microvoid–crystallite interface. If the travel time is negligible compared to the time spent in the trap, it is seen that the diffusion coefficient of **A** and of **C** is higher than that of **B**. Therefore the inner porous structure of the graphite is important and not just the void–fraction. A main cause for the scatter in the diffusion coefficient data could be due to the differences in graphite porosity and

**(A)**                        **(B)**                        **(C)**

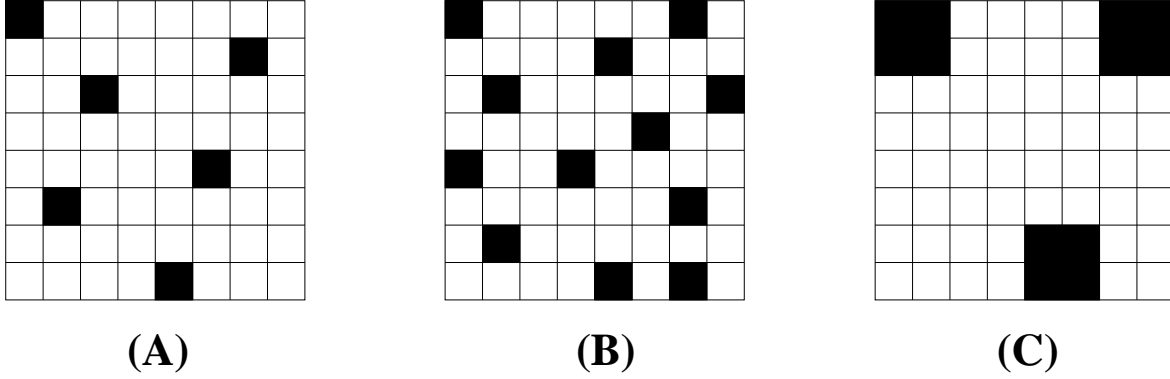**Figure 4.4:** Illustration to explain the dependence of diffusion coefficient on the void–fraction

void sizes. This statement becomes more apparent in the following paragraphs where a interpretive mode of running the simulation is explained.

Diffusion coefficients are usually published [79, 35] in the form

$$D \; = \; D_o \; e^{\frac{-E_m}{k_B \, T}} \tag{4.1}$$

with units of $length^2/second$, $D$ is the diffusion coefficient and $D_o$ is called the the pre–factor of the diffusion coefficient. Within the trapping-detrapping limited diffusion regime, this can be interpreted as

$$D \; = \; \omega_o \; L^2 \; e^{\frac{-E_m}{k_B \, T}}. \tag{4.2}$$

The physical meaning of $D_o$ is obvious from Eqn.4.1 and Eqn.4.2. It is the product of the number of jump attempts to detrap, $\omega_o$, and the square of the length jumped, $L^2$, after a detrapping event. Since our KMC code (and the simple model described later in the chapter) uses the two parameters $\omega_o$ and $L^2$ as inputs, these can be run in an interpretive mode (which means doing a parameter scan in $L$) to see at what values of $L$ does the simulation match the experimental results. The assumption here is that $\omega_o$ is similar in the various experiments and corresponds to the vibration frequency of phonons in the graphite crystallites and is of the order $\sim 10^{13} sec^{-1}$ [39].

We use the KMC code **DiG** in an interpretive mode to match the two experimental results that lie farthest from our simulations results, namely the experimental results of Causey and the saturated hydrogen diffusion experiments of Tanabe, et. al. [35].

We note that by artificially increasing the step size corresponding to transport in voids (as opposed to transport in the microvoids), we can match the various experimental results for bulk diffusion in graphite (for example $L = 1.0e - 7m, \omega_o = 1.0e13s^{-1}$ was used for DiG-Causey in Fig. 4.3). This is despite the fact that we are modeling only the mesoscopic length scales. A possible explanation is that at both macroscopic and mesoscopic length scales, the trapping and detrapping mechanisms are the same and the detrapping energies determine the time scale of transport. This, coupled with the jump length at each detrap event determines the diffusion coefficient. Therefore by introducing isotropic diffusion within the granules, and jump sizes corresponding to voids, a first macroscopic model for diffusion can be set up.

It is also observed that there is a large difference in diffusion coefficients for the hydrogen saturated graphite experiments of Tanabe, where the pre–factor $D_o = 2.1 \times 10^{-12} cm^2 s^{-1}$ suggests that the jump attempt frequency for detrapping must be of the order of $10^5 s^{-1}$ assuming a low jump step size of 1 Å. We match these results (DiG-Tanabe in Fig. 4.3) using $\omega_o^{detrap} = 1 \times 10^5 s^{-1}$ and a step size 1 Å. The reported migration energy (0.45 eV) is also much lower than expected for covalent bonds and seems to be closer to the values seen in hydrogen bonds. Such low values of $\omega_o$ are observed in activated quantum tunneling studies of hydrogen on metal surfaces at very low temperatures ($< 100K$) [80].

## 4.5 Simple model for trans-granular-diffusion

To understand better the physics we again develop a simplified model based on the above results of the simulations with the following elements:

(i) the crystallite diffusion times and void transition times are negligible compared to the time spent in being trapped at microvoid–crystallite interfaces,

(ii) isotropic 3d diffusion, since as the particle traverses the granule it encounters crystallites having a random orientation and also the microvoid diffusion paths or the grain diffusion in-between the crystallites allows 3d random motion.

Using these assumptions we get the TGD coefficient to be

$$D_{TGD} = \frac{N}{6} \left( \frac{P^{void}(L^{void})^2 + P^{cryst}(L^{cryst})^2}{\sum_{i=1}^{N}(-ln(U_i))} \right) \omega^{detrap}, \qquad (4.3)$$

where $N$ is the number of steps in the random walk, and $L^{void}$ and $L^{cryst}$ are the step sizes of the random walk in a void and in the crystallite respectively. $P^{void}$ and $P^{cryst}$ are the probabilities of the detrapped particle getting into a void or into a crystallite. $\omega^{detrap}$ is the detrapping frequency given by $\omega_o^{detrap} e^{\frac{-E_m^{detrap}}{k_B T}}$, where $\omega_o^{detrap}$ is the detrap attempt frequency, $E_m^{detrap}$ is the detrapping energy and $T$ is the target temperature.

With this simple model we are able to reproduce the above results from our TGD modeling (Fig.4.5) [81], which matches the experimental results [35]. For comparison with the simulation of experiments (**DiG_Tanabe** and **DiG_Causey**), values of $E_m^{detrap}$ from the experiments were used. The graphite structure properties used in the KMC simulations were used in the simple model. Therefore the simple model can be used to vary the graphite structure properties like void sizes and crystallite (or granule) sizes to match experimental results on diffusion coefficient in order to get a quick idea of these structural properties.
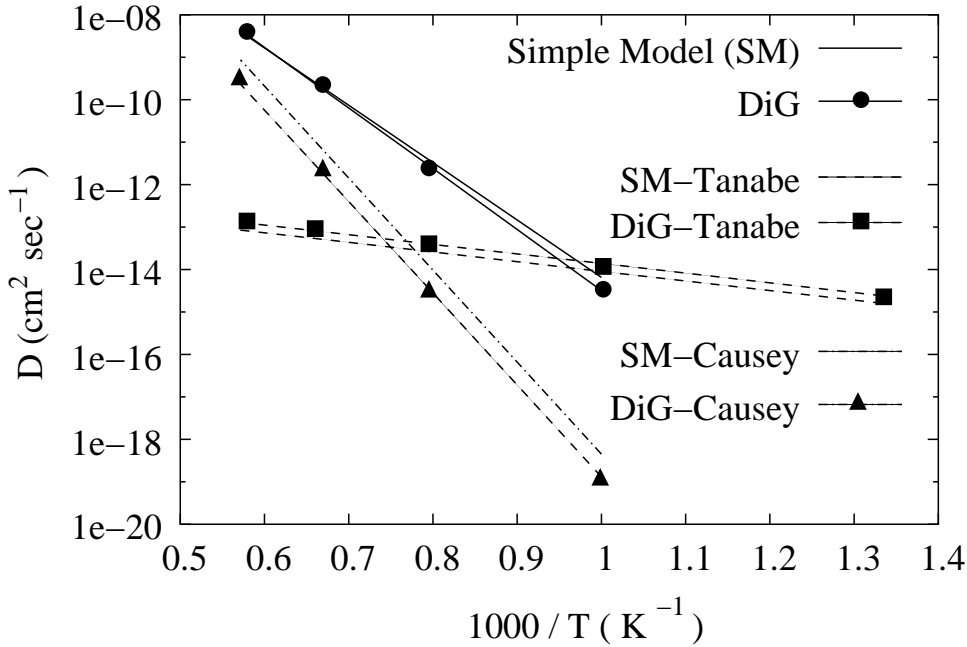


**Figure 4.5:** Comparison of $D_{TGD}$ from the simple model with simulation results (DiG)

## 4.6   Summary and outlook

The model has been extended from nanoscales to meso–scales. A wide range of experimental results for hydrogen diffusion in porous graphite has been matched by including detailed structural effects in our model. A simple model has been developed which takes into consideration the structural effects to describe hydrogen diffusion in porous graphite. The simple model matches the simulation results. It is seen that the isotope mass has almost no effect on the trans–granular–diffusion coefficient. The code has been extended with the addition of new functions to carry out hydrogen transport in randomly oriented crystallites, and to carry out atomic interactions interactions like recombination, dissociation, detrapping, etc in a general way to make adaptation easy.

We must now make use of the insights gained in trans–granular–diffusion to scale up to the next level where we model hydrogen transport in granules and voids at the centimeter scales. The effects of the granule micro–structure on hydrogen transport in granules represented by $D_{TGD}$ will be used to model the transport in granules as discussed in the next chapter.

# Chapter 5

# Scaling up to centimeters

In this section we scale up to macro–scale effects in graphites which have a thickness of a few centimeters. This is the typical width of graphites used as first wall material in fusion devices. In the first section a brief review of the relevant processes and parameters of interest is presented. The next section describes the model. Then the changes needed to implement the model in **DiG** is presented. Finally a description of the simulation and initial results for bulk transport of hydrogen is presented.

## 5.1 Relevant processes to model PSI in porous graphite

As explained in the introduction to the thesis, graphite used as first wall material is porous and consists of granules and voids. There exists a large internal surface area bounding the granules and also within the granules bounding the crystallites. Moreover there exists trap sites in the graphite bulk with estimated concentrations of the order $10^{-3} - 10^{-5}$ per C atom [82, 79]. Graphite surfaces exposed to fusion edge plasmas also get damaged by the incident energetic ions and neutrals from the plasma resulting in a high density of trap sites within the range of penetration of the incident ions ([39, 82] and references therein). Therefore the incident hydrogen ions and neutrals which are not reflected at the surface are deposited in the graphite. There follows a wide range of possibilities for their transport and inventory as reviewed in [18, 38, 39, 41] and briefly described in Chapter.1. The deposited ions neutralize at the graphite target and can either

   (i) get trapped in the region with a high density of traps, or in the bulk and

      • become detrapped (solute),

- undergo chemical reactions to form hydrocarbons or hydrogen molecules,

or

(ii) be solute and

  - become trapped,

  - recombine to form molecules at the crystallite surfaces (or granule surfaces),

In either case, the solute atoms and molecules diffuse along the voids and micro–voids with a probability of again being trapped, dissociated, or forming new molecules. There also exists finite probability of them re–entering the bulk granules or crystallites. Finally, when the hydrogen atom or molecule reaches the surface, it can be either thermally desorbed or knocked out by the incident ions.

Therefore, the relevant processes to model hydrogen isotope transport at the macro–scales are:

(i) Incident hydrogen isotope deposition profile,

(ii) Damage profile,

(iii) Trans–Granular–Diffusion,

(iv) Diffusion along voids,

(v) Trapping–detrapping,

(vi) Recombination, dissociation and molecule formation,

(vii) Desorption from graphite surface.

## 5.2 Model for hydrogen transport at the centimeter scales

A schematic for bulk diffusion in porous graphite is shown in Fig.5.1. Using the algorithm described in Section.4.1.2, a typical bulk graphite structure consisting of granules and voids is generated. The orientations of the elements (*Theta, Phi* and *Psi*) are switched off to generate this structure since our trans–granular–simulations (Chapter.4)
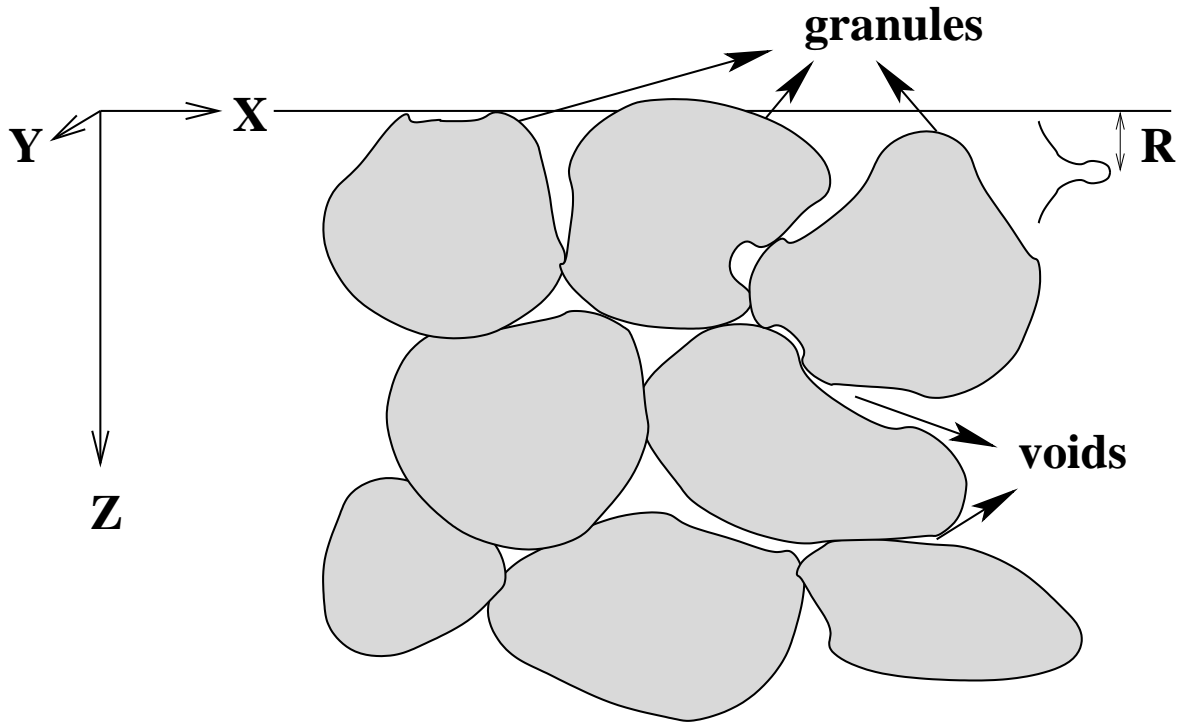
**Figure 5.1:** The Bulk simulation model schematic

show that the diffusion in granules is isotropic. The incident hydrogen deposition profile, damage profile, etc., can be obtained from **TRIM, TRIDYN** [83, 84] simulations which simulate the momentum transfer processes in a isotropic solid. At the end of the **TRIM** and **TRIDYN** simulations, the incident atoms lose their energy and thermalize with the target. Our simulations start from the point where the **TRIM, TRIDYN** simulations end. The thermalized hydrogen atom positions are initialized to have a uniform distribution along **X** and **Y**. Along **Z**, a Gaussian distribution with a specified standard deviation, centered at a depth $R$ is used to distribute the hydrogen atoms. This is a pretty good representation of the H atom deposition profile. The particles are then classified as belonging either to a void–granule surface or belonging to the bulk of the granule, depending on their locations within the graphite structure.

The algorithm for hydrogen transport is shown in Fig.5.2. The atoms at the void–granule interface and within the voids are transported using KMC, which also provides the time step $\Delta t$ for the simulation. Particles reaching the surface have a probability of being desorbed. This is also handled within the KMC algorithm. A Monte Carlo diffusion algorithm [85] (briefly described in Section.5.2.1) is implemented for treating the

trans–granular–diffusion (TGD). The diffusion coefficient for TGD, $D_{TGD}$, obtained

# –Initialise porous geometry
# –Initialise particles
# –Loop over time
## *Segregate particles (voids/granules)
## *KMC in voids (get $\triangle$t)
## *MCD in granules
# –Postprocessing

**Figure 5.2:** The Bulk simulation model algorithm

from the simulations of TGD at the meso–scales is used as input to the MCD algorithm. This is another example of how results from microscopic studies at the smaller scales is used to model transport at the larger scales.

As the hydrogen atoms diffuse along the void surfaces, if they come closer than a specified minimum distance to each other, they recombine to form a hydrogen molecule. Similarly, if the atoms come closer than a given distance to a trap, they are trapped. These minimum distances can be calculated from atomistic simulations or experiments. Dissociation and transport of hydrogen molecules within voids and on void–granule surfaces are included in the KMC algorithm. Recombination, dissociation, etc., in the granule bulk can also be easily included within a MCD algorithm. Therefore hydrogen transport, recombination, dissociation and desorption can all be studied in a porous 3D geometry within the above model.

## 5.2.1 Brief introduction to Monte–Carlo–Diffusion simulation

Any physical situation that can be viewed as a statistical outcome of some basic sub–processes, can be simulated using pseudo random numbers and is characterized as a Monte Carlo (MC) method. MC methods are efficient when a large number of dimensions or complex geometries are involved. They are especially suitable to solve

diffusion of a large number of particles in a complex geometry with independent jumps classified as a *standard Wiener process* in literature [85]. The TGD (Chapter.4) is a good example of such a process.

The N body, diffusion equation is given by

$$\frac{\partial n}{\partial t} = \nabla(D\nabla n) + S \tag{5.1}$$

where $n$ is the density, $D$ is the diffusion coefficient of the particles, $t$ is the time variable, S is the sources or sinks in the system during the diffusion, and $\nabla$ stands for the gradient in 3 dimensions. $n$ is determined by the distribution of the $N$ atoms in the simulation volume. The diffusion can represented as a random walk of the $N$ particles with the jump size given by

$$\Delta r = \sqrt{2\ D\ \Delta t}\ \zeta \tag{5.2}$$

where $\Delta t$ is the time step and $\zeta$ is sampled from a random number distribution satisfying $<\zeta> = 0$ and $<\zeta^2> = 1$. This representation is valid for $\frac{D}{\nabla D} >> \sqrt{2\ D\ \Delta t}$. Interactions can be easily included in the simulation by increasing or decreasing (depending on whether the interactions are sources or sinks) the number of particles diffusing at each time step by $e^{-\frac{\Delta t}{\tau}}$ where $\tau$ is the characteristic time for the interaction to occur. Note that Eqn.5.2 at first glance looks like a rewritten form of Eqn.2.8. In fact it is derived using the differential calculus of stochastic processes called *Itô calculus* [85]. Such a treatment is necessary because the position variable $r(t)$ in Eqn.2.8 is obtained by a stochastic process (random walk).

To simulate TGD of hydrogen atoms in granules, Eqn.5.2 is used. The time step $\Delta t$ is decided within the KMC scheme and $D_{TGD}$ is obtained from the TGD simulations described in Chapter.4. A Gaussian pseudo–random number generator is used to set $\zeta$ in our simulations.

## 5.3  Code adaptations

The main addition to **DiG** is the Monte–Carlo–Diffusion module. Along with this it is necessary to segregate the particles depending on whether they are in voids (transported by the KMC module) or within the granule (transported by the MCD module). A surface from which desorption occurs had to be introduced. Functions for

trapping, detrapping, recombination, desorption, dissociation and for various types of jump events have been introduced. As was the case with earlier upgrades, care is taken to facilitate easy addition of new species and interactions.

## 5.4 Hydrogen transport simulation at macro–scales

### 5.4.1 Inputs and setting up the simulation

A cubic granular structure of length $5 \times 10^{-5}m$ is created (Fig.5.3). This typically
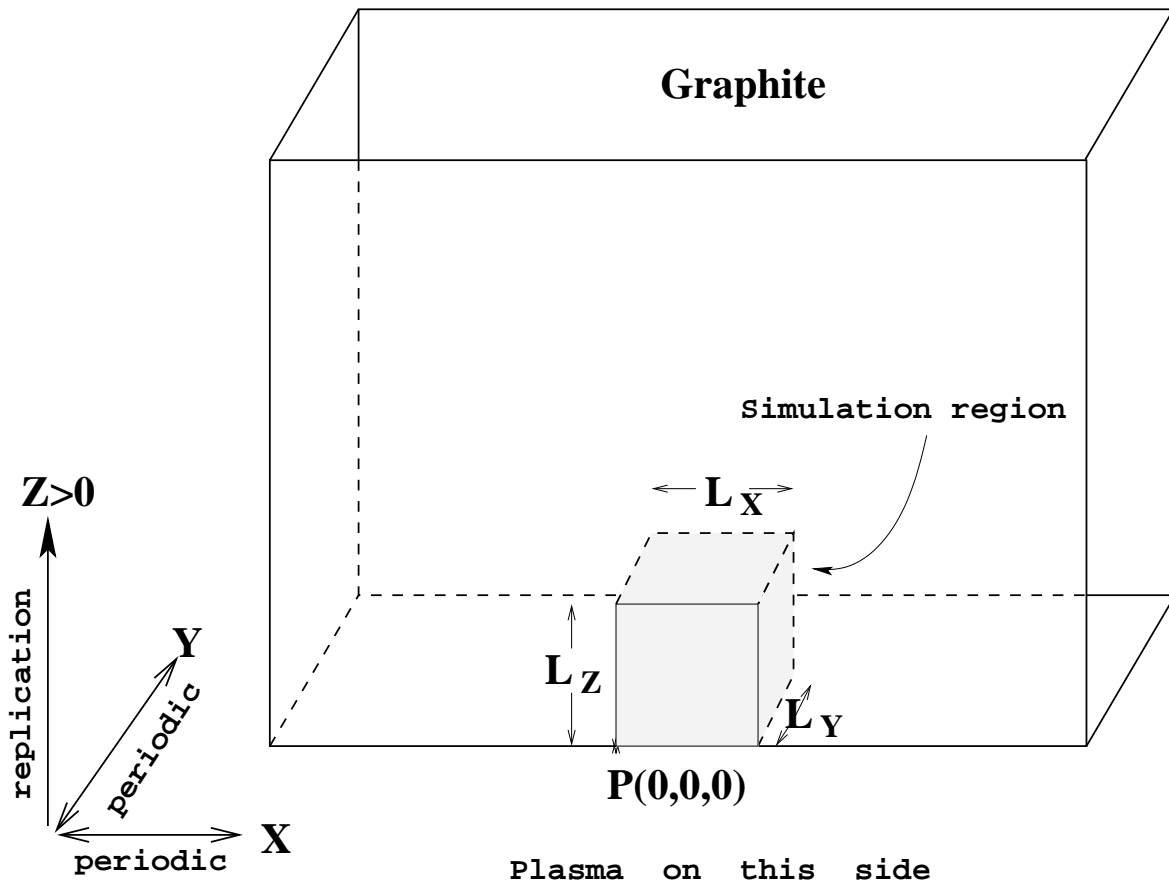


**Figure 5.3:** The Bulk simulation model geometry

accommodates 8000 granules using a *element–length* of $2.5 \times 10^{-6}m$. The *cell–length* chosen is $5 \times 10^{-7}m$. These values for *element–length* and *cell–length* correspond to realistic granule and microvoid sizes. Periodic boundary conditions are applied along the **X** and **Y** directions, which are the directions parallel to the graphite surface. Along the **Z** direction, which lies perpendicular to the graphite surface, the structure is repli-

cated for $\mathbf{Z} > 0$. The graphite surface lies at $Z = 0$ and faces the plasma located in the negative $\mathbf{Z}$ direction.

1000 H atoms are uniformly distributed in the X-Y plane. The atoms have a Gaussian distribution along the Z axis, centered at a depth of 100 Å from the surface with a width 10 Å. The void fraction was chosen to be 0.1 and therefore most of the particles end up inside granules. The rest of the particles are assumed to be solute H on the void–granule interface. Due to the low concentration of H atoms, hydrogen molecules are not formed. The results are applicable to a very low concentration case. However this calculation gives an idea of possible transport preferences within the various regions, i.e. voids, granules and out of the surface (recycling).

The inputs to the code are from a mixture of experimental results and MD simulations. The activation energy for trapping–detrapping within the granule is taken to be 2.7 eV since the TGD diffusion coefficient obtained from our simulations using this value lies nicely in the middle of the range reported in experiments [35]. Within the KMC algorithm, the activation energy for desorption is taken to be 1.91 eV [86]. The activation energy for surface diffusion is taken to be 0.9 eV, with a jump attempt frequency of $10^{13}$ s$^{-1}$ and a jump step length of 34.64 Å to match the surface diffusion coefficient reported in [79]. Activation energy for entering the surface for a solute H atom is same as the activation energy for TGD. The simulations are carried out at target temperatures between 300 K and 1500 K in intervals of 300 K. The particles were followed for $10^6$ steps.

## 5.4.2    First results of macro–scale simulations

The final number of particles in different regions are plotted as a function of target temperature (Fig.5.4). In this plot $N$ stands for the number of particles in a region, and the region is given as a subscript. We see that there is almost no transfer of particles from one region to another below $900K$ because the activation energies for bulk diffusion and desorption are too high. Most of the transport is by surface diffusion of the solute atoms. Particles start getting into the bulk and from the bulk to the voids in our simulations at 1200 K and this is more pronounced at 1500 K. It is also seen that desorption of hydrogen atoms from the surface (denoted by $N_{recycle}$ in Fig.5.4) starts off somewhere between 900 K and 1200 K. Such behavior for hydrogen atom

desorption is observed in experiments [79, 87].
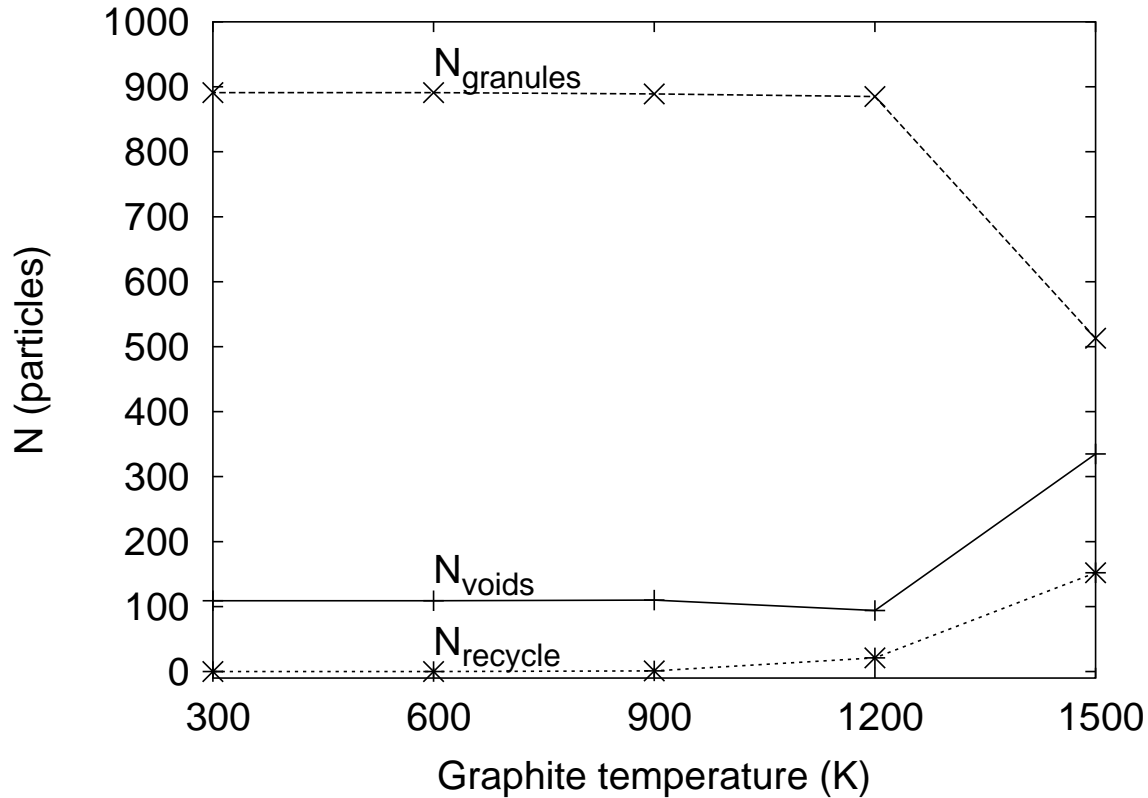


**Figure 5.4:** Number of particles in different regions at the end of a million KMC steps

Note that $10^6$ time steps correspond to different times of simulation at different graphite temperatures since the time step is determined by the KMC algorithm (see Eqn.3.2). A plot of the final hydrogen atom positions are shown in Fig.5.5 for

(i)  300 K where $10^6$ steps correspond to $1.38 \times 10^6 s$,

(ii)  900 K where $10^6$ steps correspond to $1.15 \times 10^{-4} s$, and

(iii)  1500 K where $10^6$ steps correspond to $9.25 \times 10^{-7} s$.

The plot is a projection of the atomic positions on the **Z-X** plane, with the **Z** axis stretched. This stretching creates the effect of atoms moving preferentially along **Z**, which is not the case. The brown color is used for atoms which are situated in voids and cyan color is used for atoms situated in granules. It is seen that particles in the voids and void-granule surface diffuse much faster due to the low migration energy of

surface diffusion and get deep into the surface in the absence of open trap sites at all temperatures. It is seen that there is almost no diffusion within the granule (cyan colored atoms) at temperatures $\leq$ 900 K where the migration energy for diffusion is too high $\sim 2.7eV$. Therefore it can be expected that in the presence of open traps (which typically have a binding energy of $\sim 2.7eV$), the atoms will not penetrate to such depths at these temperatures. However, at temperatures $\geq$ 1200 K, the atoms in the granules too (cyan colored Fig.5.5-iii) show a visible diffusion broadening and penetrate into the porous graphite.

## 5.5   Summary and outlook

A model for bulk diffusion in porous graphite is developed. It consists of trans–granular–diffusion, diffusion in voids and along void–granule surfaces. Initial results from the model are in line with experimental observations of desorption and transport into bulk graphite. The model allows molecule formation and transport and can handle recombination, dissociation and trapping. The main aim of this thesis, which was **to create a framework to study multi–scale transport of hydrogen isotopes in a porous graphite like structure** has been achieved.

Using this macroscopic model we are now able to simulate correctly the atomic hydrogen desorption from graphite at temperatures above 900 K, the diffusion of hydrogen along void surfaces into depths of a few microns, and the different regimes of hydrogen diffusion in graphite. The code implementing the multi–scale model **DiG** has a modular structure and new species and interactions can be easily added. Application of the code to a couple of problems of interest are described in the next chapter.

(i) 300 K ($1.38 \times 10^6 s$)
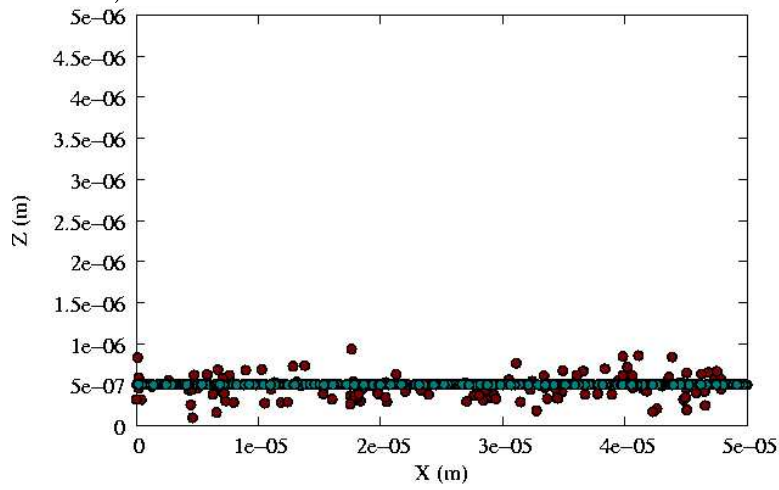


(ii) 900 K ($1.15 \times 10^{-4} s$)
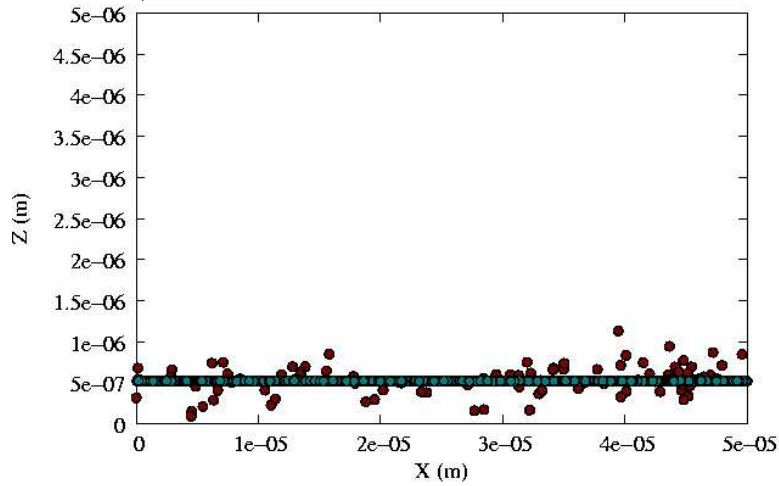


(iii) 1500 K ($9.25 \times 10^{-7} s$)



**Figure 5.5:** Atomic diffusion range (Cyan for atoms in granules and brown for atoms in voids

# Chapter 6

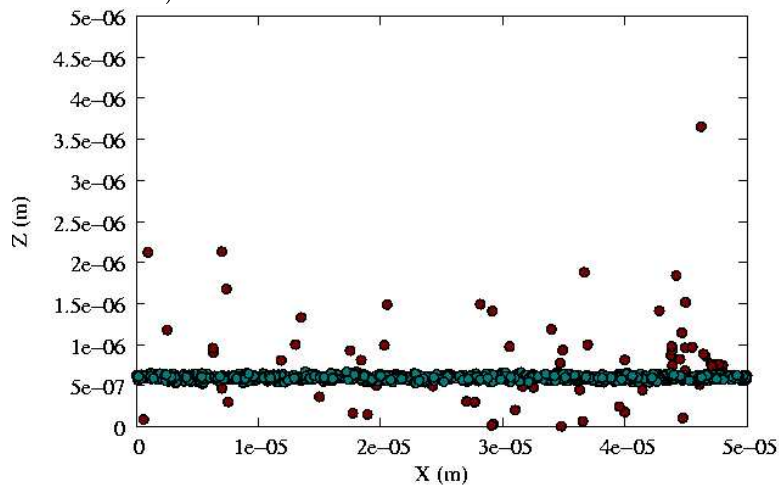# Applications of the simulation

The multi–scale model developed in the previous chapters of this thesis is applied to study:

- Hydrogen transport in graphites with closed pores.

- Diffusion coefficient of hydrogen in porous graphite.

Applications of the model will give us improved insight into these problems and will prove the variousă possibilities for applications of the developed model.

## 6.1   Hydrogen transport in graphites with closed pores

Transport and retention in graphite with closed pores is of interest as part of optimizing the graphites to make them suitable as first materials in fusion devices. Closed pore graphites are created by increasing the graphitization temperature of doped graphite during the production process of graphite [88, 89]. Closed pores can reduce the accessibility of internal surface areas within the graphite, thereby reducing the area available for hydrocarbon formation and hydrogen isotope retention. This can have implications for chemical erosion and hydrogen isotope inventory in graphites. We study the effect of closed pores by artificially keeping the surface cells (cubes of size $5 \times 10^{-7}m$) occupied. This implies that there are no open voids leading out from a depth of $5 \times 10^{-7}m$ inside the graphite sample to the surface, though voids may exist as usual along all other directions. The hydrogen atoms are initialized around $6 \times 10^{-7}m$ with a spread of $1 \times 10^{-9}m$, and are allowed to diffuse in the sample kept at temperatures of 300 K, 600 K, 900 K, 1200 K and 1500 K. The simulation is repeated without closing the

pores for comparison and the results are presented below.

The particle positions at the end of $10^6$ steps is at 300 K, 900 K and 1500 K, for both, closed pores and open pores is shown in Fig.6.1. This plot is a projection of the

(a) 300 K Open pores

(b) 300 K Closed pores

(c) 900 K Open pores

(d) 900 K Closed pores

(e) 1500K Open pores
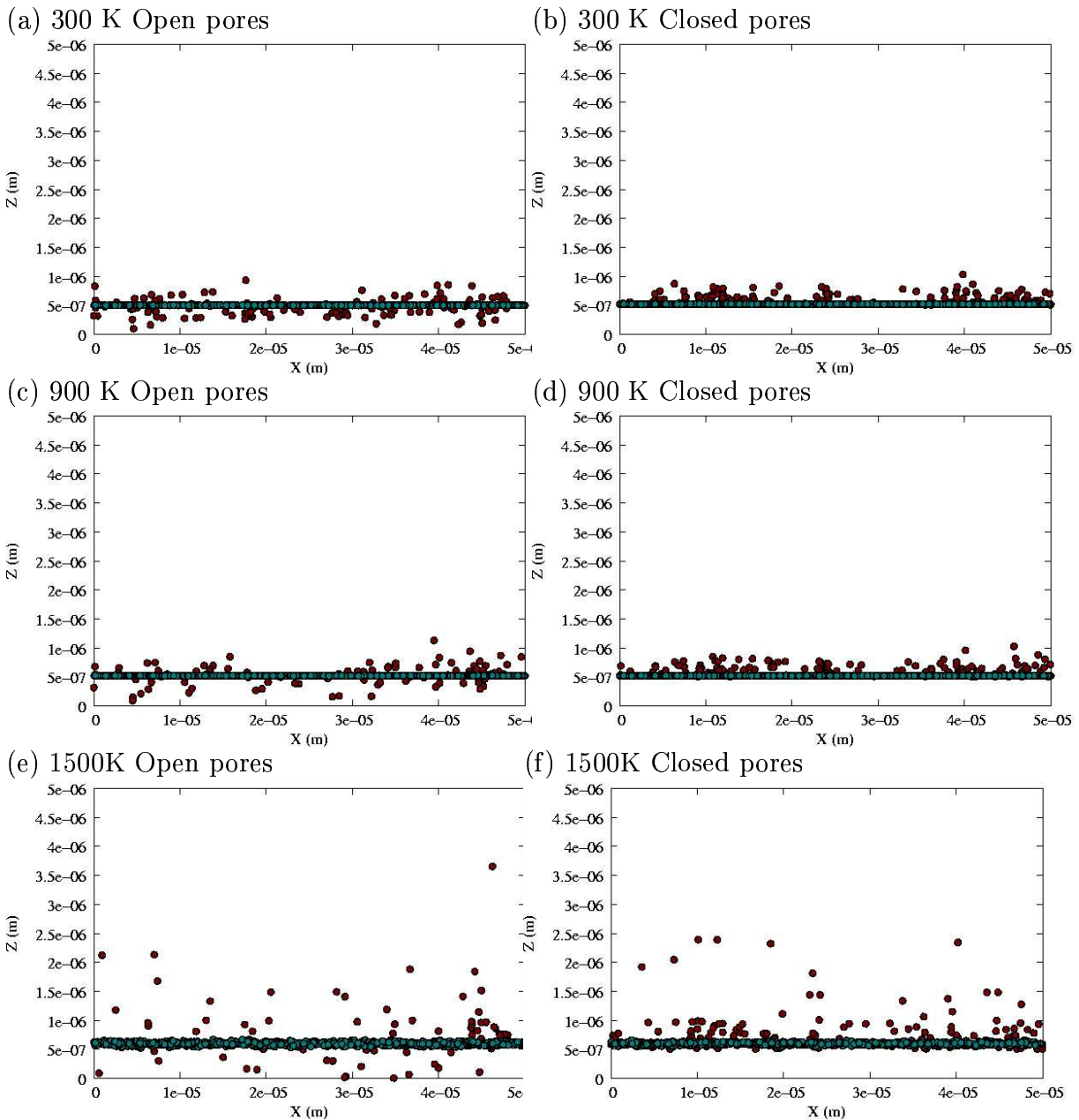
(f) 1500K Closed pores

**Figure 6.1:** H atom positions at the end of $10^6$ steps for different graphite temperatures for open and closed pore cases

atomic positions on the **Z-X** plane, with the **Z** axis stretched (like in Fig.5.5). The

brown color is used for atoms which are situated in voids and cyan color is used for atoms situated in granules. The graphite surface is situated at $Z = 0$. It is seen that most of the diffusion broadening is due to surface diffusion of atoms in the voids. At 1500 K the atoms in the granules too show some diffusion broadening in both cases. Note that there is no diffusion into closed pore region ($\mathbf{Z} \leq 5 \times 10^{-7} m$) for the 900 K and $300K$ *closed pores* cases. In the 1500 K *closed pores* case there is some diffusion into the closed pores region. This is in contrast to the *open pores* cases where there is a normal diffusion in all directions.

The above idealized example suggests that when closed pore graphites are used as plasma facing materials, the diffusion into the bulk of the graphite will be hindered and the hydrogen isotope inventory within the graphite bulk in such cases will be reduced.

## 6.2 Diffusion coefficient of hydrogen in porous graphite

There exist many channels for hydrogen diffusion in porous graphite:

- Diffusion in crystallites, with two channels of diffusion, considered in Chapters.2 and 3.

- Trans–granular–diffusion (TGD), which consists of the diffusion in crystallites plus the possibility of trapping–detrapping at the crystallite–microvoid interfaces as discussed in Chapter.4.

- Diffusion in voids, consisting of surface diffusion, a adsorption–desorption based mechanism and a trapping–detrapping mechanism on the void–granule surface as described in Chapter.5.

Within our bulk transport model presented in Chapter.5, the diffusion in the crystallites and TGD enter the simulation as a trans–granular–diffusion coefficient, $D_{TGD}$. We have seen that the transport due to $D_{TGD}$ (i.e. the transport in granules) is much smaller than the transport in the voids and void–granule surfaces. It is only at high graphite temperatures ($\sim$ 1500 K) that TGD shows up (Fig.6.1–e,f). In Chapter.4 we discuss how by artificially increasing the step size corresponding to transport in voids, a good match with the experimental results [35] of diffusion coefficient in bulk graphite is obtained. It is desirable to apply the bulk diffusion model to study the diffusion coefficient variations with graphite temperature and to compare the simulation results

with experiments.

Using the inputs as described in Section.5.4.1, bulk simulations at 300 K, 600 K, 900 K, 1200 K, 1500 K and 1800 K are carried out. The diffusion coefficients are calculated using Eqn.2.8. The diffusion coefficients obtained are plotted on a log–scale as a function of $1000/T \ K^{-1}$ in Fig.6.2 (labeled **DiG**). We see that the diffusion coefficients
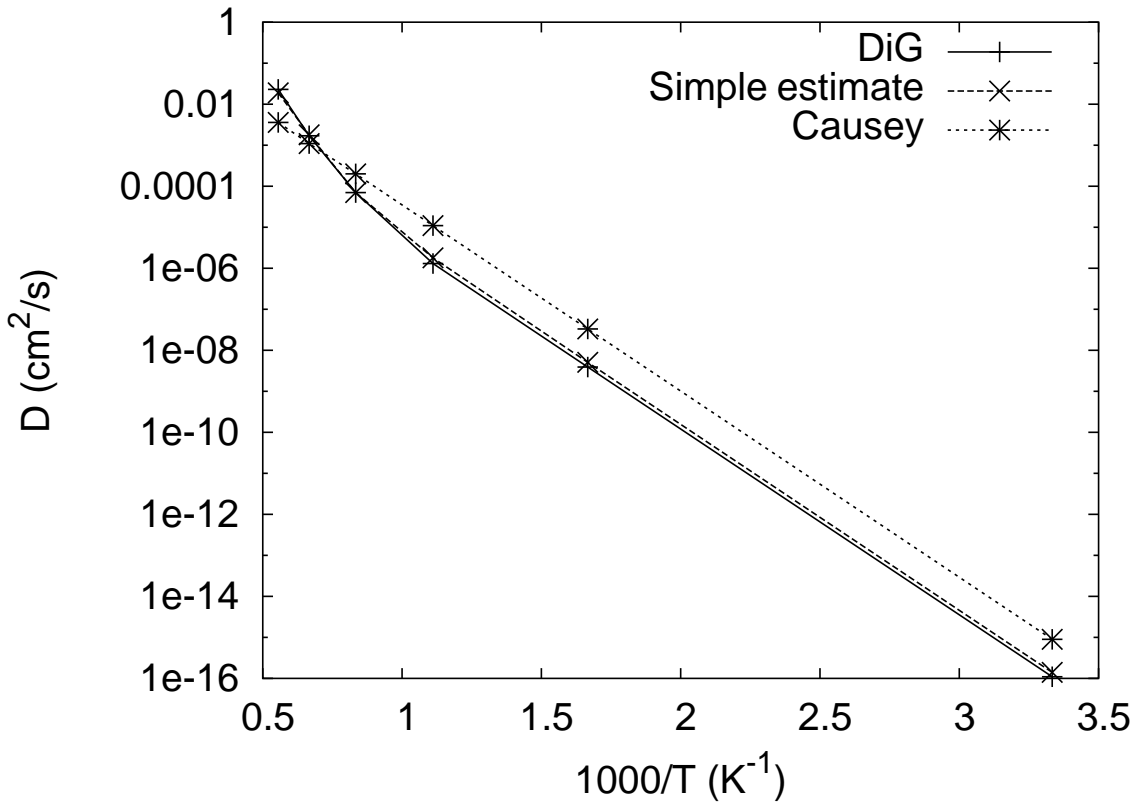


**Figure 6.2:** Diffusion coefficient for hydrogen in porous graphite compared with a simple estimate similar to the two kinds of jumps model presented in Section.3.3 and Causey's result for surface diffusion in graphite [79]

are much larger than the reported values [35] for bulk diffusion in graphite. We also see that there exists two different channels for diffusion by the two different slopes that are seen in Fig.6.2. This is because the diffusion is dominated by surface diffusion on the void–granule surface and the adsorption–desorption diffusion mechanisms in voids. These mechanisms have much smaller migration energies ($0.9eV$ and $1.91eV$) respectively, compared to the trapping–detrapping mechanisms at trap sites (between $2.65eV$ to $4.3eV$ [35]). We also plot a simple estimate of the diffusion coefficient by using the *two kinds of jumps* model presented in Section.3.3 for jump parameters corresponding

to surface diffusion and adsorption–desorption in voids. Reported [79] values of diffusion coefficient for surface diffusion ($1.2\ e^{\frac{-0.9}{k_B T}}$) is also plotted in Fig.6.2 for comparison. It is seen that at temperatures $< 1200$ K the surface diffusion dominates, with the adsorption–desorption channel dominating at temperatures $\geq 1200$ K.

There is a difference of almost an order of magnitude in the values of the surface diffusion coefficient obtained from our simulation and [79]. This is inspite of the choice of step size of surface diffusion being based on this experimental result. This could be due to the fact that the diffusion is occurring in a complex geometry, and our method of evaluating the diffusion coefficient ($D = \lim_{t\to\infty} \frac{1}{2dt}\ [r(t) - r(o)]^2$), assuming a dimensionality of 3 is naive. Special techniques must be used to evaluate the diffusion coefficients in a porous disordered geometry [90]. One can understand this looking at figure Fig.6.3 which is a schematic (not to scale) of the projection of a granule surface on a 2–D plane. It is clear that the mean square deviation calculated using $r(t) - r(o)$
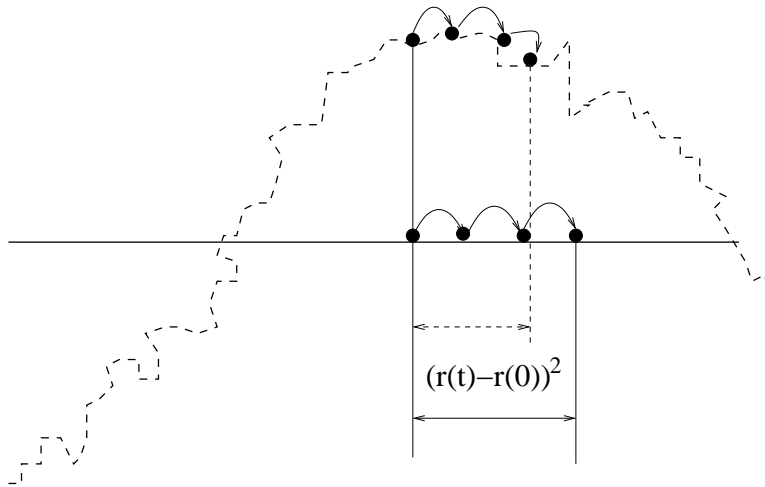


**Figure 6.3:** Illustration of the complex diffusion surface as opposed to the a smooth surface

of a particle undergoing a random walk with a uniform step size on the rough surface (dashed line) is lesser than that if it were undergoing the random walk on the smooth surface. This should be considered when setting the step size in the simulation based on reported experimental results.

We then carry out simulations by switching off the surface diffusion and the adsorption–desorption mechanisms, keeping only the trapping–detrapping mechanism with $4.3 eV$ trap energies. The simulation was on a highly resolved structure using a cell size

$1 \times 10^{-8} m$ which required around 1/2 GB of RAM. The RAM requirement scales as $(L/CellSize)^3$ since the geometry details have to be stored for quick access in the RAM, where $L$ is the length scale of the simulation volume and $CellSize$ is the size of a cell. Note that $L$ must be large enough to at least contain a few granules (of size $\sim 1micron$) to realistically simulate bulk diffusion. We chose $L$ to be 5 $microns$ so as to be able to accommodate at least 5 granules, which would mean around 125 granules in the whole simulation volume. The simulations were carried out at 1200 K, 1500 K and 1800 K to compare with the results for bulk diffusion by Causey et. al. reported in [35]. The results of these simulations are presented in Fig.6.4. The diffusion coef-
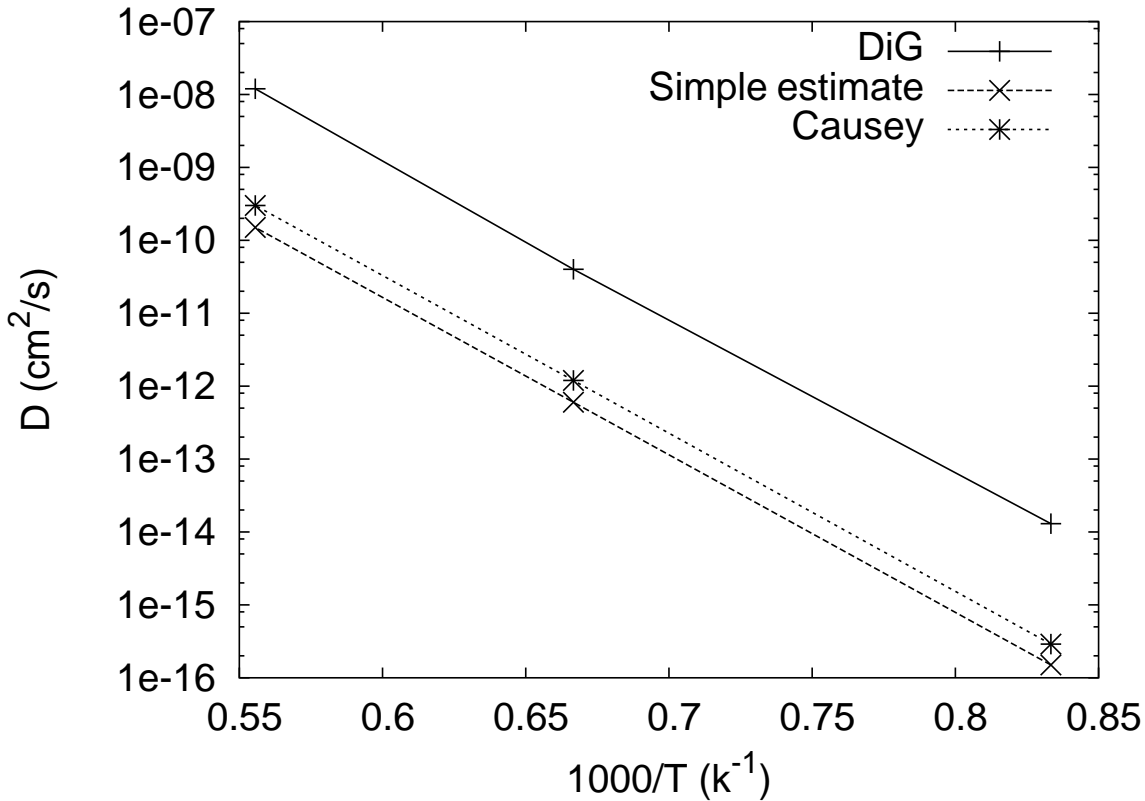


**Figure 6.4:** Diffusion coefficient for hydrogen in porous graphite with surface diffusion and adsorption–desorption mechanisms on void surfaces switched off. This is compared with with a simple estimate based on a 3–D random walk and Causey's result for bulk diffusion in graphite [79]

ficient obtained lies in the range of reported experimental results for bulk diffusion in graphite. It differs by almost two orders of magnitude as compared with the results by Causey et. al. The main reason is the granule size (and therefore the void size) we choose is $1/10^{th}$ the value reported in Causey's experiment due to RAM limitations in our simulation. Simulation of a realistic bulk structure will require around 500 GB of

RAM. However, using the results of this simulation in a simple estimate including a modified void size which is typically 10 times greater than in the simulation, we are able to reproduce the experimental result within a factor of 2. The results from the simple estimate are also included in Fig.6.4.

## 6.3   Summary and outlook

In this chapter we applied the multi–scale model to various problems gained some insights and directions for future work like,

- Closed pore graphites can prevent diffusion along internal surfaces deep into the graphite bulk and will minimize the effective surface available for hydrocarbon formation and hydrogen retention.

- Surface diffusion dominates H transport in bulk graphite at temperatures < 1200 K beyond which adsorption–desorption diffusion begins to dominate inspite of its larger migration energies. This is due to larger possible step sizes depending on the void sizes.

- Diffusion coefficients have to be interpreted taking into account the disordered internal surfaces, not only in simulations, but also when reporting experimental results.

# Chapter 7

# Summary and Conclusions

Plasma surface interactions (PSI) are an important aspect of modeling the edge plasma and designing plasma facing materials (PFM) for fusion devices. Graphite is the most widely used PFM in the various experimental devices used to study fusion plasmas, due to its good thermal conductivity, low atomic number, etc. However as the stage sets for ITER, a experimental fusion reactor, some aspects of hydrogen isotope interactions with graphite like tritium inventory, flux dependence of chemical sputtering, higher hydrocarbon formation and release, etc., need to be understood. This will help in understanding the limitations of graphite as a PFM and also probably in designing new types of graphite which can be used as PFMs.

The graphites used as PFMs in fusion devices are porous and consist of granules (few microns in size) separated by voids (fraction of a micron in size). These granules further consist of randomly oriented crystallites (a few nanometers in size) separated by micro–voids (a few Å in size). The incident hydrogen isotopes from the plasma cause damage within their range of penetration and the atoms that do not get backscattered, thermalize with the carbon atoms within the graphite. Due to the porous structure there exist large internal surface areas within the graphite. An algorithm to create a porous medium of specified void–fraction, consisting of elements, the sizes of which are assigned by a Poisson distribution, is developed.

The hydrogen isotopes can diffuse along the voids and micro–voids, get trapped at trap sites in the graphite bulk or at the surface where there exists a high density of traps due to incident ions. They can also recombine to form molecules and react chem-

ically with the carbon atoms in graphite to form hydrocarbons. In order to understand how the microscopic processes at the atomistic level affect the macroscopic transport and inventory of hydrogen isotopes and hydrocarbons, models of atomic interactions and transport at the different scales are required. Parameters that get transferred between the models at different scales have to be identified and can be used either from ab–initio theory or from experiments. The main aim of this thesis is to develop such a multi–scale model for hydrogen transport in porous graphite which serves as a test bed for addressing other problems concerning using graphite in fusion devices.

At the microscopic scales, molecular dynamics (MD) is used to simulate the diffusion of hydrogen isotopes in crystalline graphite. It is seen that hydrogen isotope diffusion has two channels for diffusion. These channels can be represented as a trapping–detrapping process, with characteristic jump attempt frequencies, migration energies and jump lengths. It is seen that the channel with a low migration energy dominates the diffusion and varies as the inverse square root of the isotope mass. The channel with the high migration energy starts contributing to the diffusion above 450 K and is independent of the isotope mass. A Kinetic Monte–Carlo (KMC) simulation, and a simple analytical model, reproduce the MD results using the two channel, trapping–detrapping description.

At the mesoscopic scales, hydrogen transport in randomly oriented crystallites separated by microvoids are modelled using KMC. The hydrogen atoms diffuse within the crystallites as parametrized from the MD simulations and get trapped at the crystallite–microvoid interface with a specified trapping–detrapping probability. The trans–granular–diffusion (TGD) coefficients, $D_{TGD}$, match a wide range of experimental results for hydrogen diffusion in porous graphite by changing the structure parameters (void sizes). It is seen that the random orientations of the crystallites make the diffusion isotropic and that the isotope mass has almost no effect on $D_{TGD}$ within our model. A simple analytical model is developed, which is consistent with these results.

Extending the model to centimeters, the diffusion of hydrogen within granules and voids is studied. Values of $D_{TGD}$ from our meso–scale simulations are used to implement diffusion in the granules using a Monte-Carlo diffusion (MCD) ansatz. KMC is used to model the transport in voids and on the granule–void interfaces. Dissociation, desorption from the granule–void interface, etc., are all included within the KMC

ansatz using appropriate activation energies as reported in experiments. The hydrogen atoms recombine if they come closer than a specified minimum distance. New species and interactions can be added depending on the problem of interest.

This multi–scale model is used to study hydrogen desorption, transport in gaphites with closed pores, and the various diffusion regimes in porous graphite. The model correctly matches experimental results for the temperature dependence of desorption, shows that diffusion along internal surfaces is hindered in closed pore graphites and lends insight into the different channels of diffusion in porous graphite.

The new multi–scale code developed in this thesis, **DiG**, provides new insights into the transport in porous graphite and improves the physics understanding. This should stimulate also the experimental validation of these predictions. This will only be possible by close interaction with experimental groups and will need a flexible adaption to thier needs. This is easily possible due to the modular structure of the code.

# Appendix A

# Simple model for PSI and coupling with SOLPS-B2.5

The multi–scale model developed in this thesis aims to provide finally a better description of the bulk processes in the target during plasma surface interactions (PSI). This is done by the modeling the underlying physical processes at different scales. The better description obtained, should then be used in a self consistent model for PSIs. In this appendix a simple model for PSI is described which identifies the various modules that are necessary to model plasma surface interactions.

This simple model can be used as the PSI part of edge plasma codes or for making erosion, implantation, and reflection estimates for plasma facing surfaces. Published semi-empirical formulas for physical sputtering [91], chemical erosion [17], radiation enhanced sublimation (RES) [92], and backscattering [93, 94] have been implemented as FORTRAN subroutines [21]. see Appendix.B for details of the formulas. A subroutine to calculate the thermal evaporation of graphite which is important at high heat loads is also implemented. Finally, the effect of self consistently including the target temperature calculation in case of a graphite target is studied by including these subroutines in the scrape off layer plasma simulation code, SOLPS-B2.5 [22, 23].

## A.1 Plasma-surface interaction model

Any material surface facing a plasma is connected to the plasma by means of a sheath. The sheath depends on the plasma parameters like density and temperature, ambient

magnetic field and applied voltage to the plasma facing surface [10, 11, 13]. The sheath affects the energy and angular distributions of ions incident on the plasma facing surface. The energy deposited by the plasma on the surface determines the surface temperature which is an important parameter in quantifying the chemical erosion yield, RES and thermal evaporation contributions to graphite erosion. Therefore a model for the sheath, the incident heat and particle flux, and a heat transport model in the target are important parts of modeling PSI. A zero-dimensional steady-state particle balance model at the target using sputtering yields, backscattering coefficients and evaporation rates, is used to calculate the erosion rate of a plasma-facing surface.

### A.1.1   Sheath

A collision–less 1-D sheath model is used, based on the results of various studies on the plasma sheath which have been compiled by Stangeby [10]. The incident energy of ions on the surface is equal to the sum of the energy with which ions enter the pre–sheath, the energy gained in the pre–sheath and the energy gained in the assumed collision–less sheath. For a plasma temperature $T_i$ (for ions) and $T_e$ (for electrons) at the plasma-sheath interface, the average ion energy will be a sum of:

(i) the average energy per ion leaving a Maxwellian plasma ($= 2T_i$)

(ii) energy gained by acceleration in the pre–sheath, given by the general non-zero $T_i$ Bohm sheath criterion [12] ($= T_e + \gamma T_i$)

(iii) energy gained by acceleration in the sheath ($= Z_i \Phi$).

Note that $T_e$ and $T_i$ are all in units of eV, $\gamma$ is 1 for isothermal flow, 5/3 for adiabatic flow with isotropic pressure and 3 for adiabatic flow [10] in the pre–sheath. The sheath potential $\phi$ is in V and $Z_i$ is the charge of incident ions.

For a floating surface, $\Phi$ is given by [10]

$$\Phi = \Phi_{float} = \frac{1}{2} \, T_e \, ln \left[ \left( 2\pi \frac{m_e}{m_i} \right) \left( 1 + \frac{T_i}{T_e} \right) \right] \tag{A.1}$$

and for a biased surface, the plasma is shielded from the applied voltage $\Phi_{app}$ by the sheath potentials at the anode $\Phi_a$ and at the cathode $\Phi_c$, such that $\Phi_{app} = \Phi_a - \Phi_c$, with $\Phi_a$ given by

$$\Phi_a = T_e \, ln \left[ \frac{2e^{\Phi_{float}/T_e}}{1 + e^{\Phi_{app}/T_e}} \right] \tag{A.2}$$

Note that when $\Phi_{app} = 0$, $\Phi_a = \Phi_c = \Phi_{float}$. Therefore the bombarding ion energy is

$$E_i = T_e + (\frac{3}{2} + \gamma)T_i + Z_i\Phi_c. \tag{A.3}$$

The incident ion flux on the surface is the same as the ion flux entering the sheath from the pre–sheath

$$\Gamma_s \;=\; n_s C_s \tag{A.4}$$

where $n_s(= n_e = Z_i n_i$ is the plasma density at the plasma-sheath interface, and $C_s$ is the sound speed given by $((T_e + \gamma T_i)/m_i)^{1/2}$ where $m_i$ is the mass of the ion.

The heat flux deposited by ions is given by

$$q_i = \Gamma_s E_i \tag{A.5}$$

The heat flux deposited by electrons on the surface is given by

$$q_e = 2T_e C_s n_s e^{\frac{\Phi_{app}}{T_e}} \tag{A.6}$$

Therefore, given the plasma parameters of density $n_s$, ion temperature $T_i$ and electron temperature $T_e$ at the plasma-sheath interface, and the applied voltage $\Phi_{app}$, useful information for PSI like average energy of incidence (Eqn.A.3), the incident ion flux (Eqn.A.4) and the heat flux on the surface (Eqns.A.5,A.6) can be found. Note that we do not have any information of the angular distribution of the bombarding ions, which can affect physical sputtering yields and backscattering coefficients. We assume that in the absence of collisions in the sheath, all ions are accelerated to velocities much greater than their thermal velocities (typically $\sqrt{2E_i/m_i}$) and therefore are more or less normally incident on the surface if it is assumed that there are no magnetic fields present.

## A.1.2 Heat diffusion

The 3-d heat diffusion equation is given by [95]:

$$\frac{\partial}{\partial x}\left(k_x\frac{\partial T}{\partial x}\right) + \frac{\partial}{\partial y}\left(k_y\frac{\partial T}{\partial y}\right) + \frac{\partial}{\partial z}\left(k_z\frac{\partial T}{\partial z}\right) + S = \rho C_p\frac{\partial T}{\partial t} \tag{A.7}$$

where $T$ is the temperature, $(x, y, z)$ are the 3 Cartesian coordinates, $k$ stands for heat conductivity, $S$ is the volumetric sources or sinks of heat per unit time, $\rho$ is the density

of the surface material, $C_p$ is the specific heat of the material at constant pressure and $t$ is the time variable.

A uniform, steady state plasma is assumed to be in contact with a surface. The heat diffusion into the plasma-facing surface is assumed to be 1-dimensional. The thermal conductivity dependence on temperature can be described by $\frac{1}{aT+b}$ in most cases [96]. It is also assumed that there are no bulk sources or sinks of heat. With these assumptions the 3-d, time dependent heat diffusion equation reduces to

$$\frac{\partial}{\partial x}\left(k\frac{\partial T}{\partial x}\right) = 0 \tag{A.8}$$

the steady state 1-d heat diffusion equation (without bulk volumetric sources or sinks) [95].

The heat flux incident on the surface is used to implement a Neumann–type boundary condition at the plasma-facing end $(x = 0)$

$$-k(T)\frac{\partial T}{\partial x} = q_i + q_e \tag{A.9}$$

where $q_i$ and $q_e$ are given by Eqns.A.5, A.6. Therefore, the incident heat flux on the surface enters the equations as a boundary condition which is an effective heat flux source at the boundary surface. Note that cooling of the surface due to radiation and evaporation or sublimation is neglected. The additional contribution to the deposited heat by ion recombination on the target is also neglected.

The temperature at the cool end $(x = L)$ is specified to implement a Dirichlet-type boundary condition.

$$T(L) = T_L \tag{A.10}$$

With the assumed $\frac{1}{aT+b}$ variation of $k$, and solving Eqn.A.8 with the boundary conditions specified by Eqn.A.9 and Eqn.A.10 results in the temperature $T_p$ at the surface (as in [96]) given by:

$$T_p = \left(T_L + \frac{b}{a}\right)e^{a(q_i+q_e)L} - \frac{b}{a} \tag{A.11}$$

### A.1.3   Surface interaction

We present a 0-d steady state particle flux balance equations for surface interactions with hydrogen as the plasma species and graphite as the target. It is similar to [97], but with backscattering of the returning carbon flux considered and is also extended to calculate net erosion. The addition of backscattering of the incident carbon ions is necessary only when one can differentiate between the backscattered carbon atoms and sputtered carbon atoms. The semi-empirical formulas for sputtering yield [91] and backscattering [93, 94] implies differentiation between the carbon sputtered and the carbon backscattered.

Consider an incident flux of hydrogen ions $\Gamma_H$. This results in a sputtered flux of carbon atoms. Some of this flux of carbon atoms gets ionized and returns to the target. The returning flux of carbon also causes self sputtering of graphite. A fraction $R_N$ of the returning flux of carbon atoms also backscatters from the surface, with the remaining fraction $(1 - R_N)$ getting redeposited on the target. In addition to these processes there is also a steady flux of carbon atoms evaporated from the surface. A
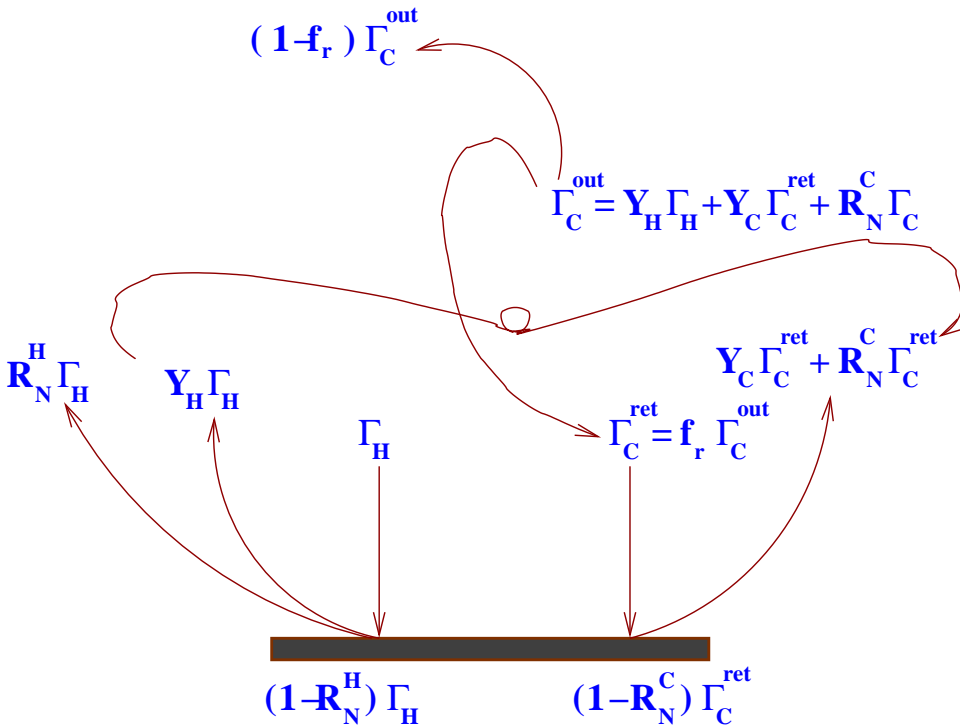


**Figure A.1:** 0-d steady state surface erosion model

steady state picture of all the processes involved is shown in Fig.A.1. We see from the

figure that in steady state the total flux of carbon atoms going away from the target is

$$\Gamma_C^{out} = Y_H \Gamma_H + Y_C \Gamma_C^{ret} + R_N^C \Gamma_C^{ret} + \Gamma_C^{evap} \tag{A.12}$$

where $Y_H \Gamma_H$ is the total sputtered flux of carbon atoms due to hydrogen incidence and $Y_H$ is a sum of the physical, chemical and RES yield contributions of H incident on graphite:

$$Y_H \;=\; Y_H^{phy} + Y_H^{chem} + Y_H^{RES} \tag{A.13}$$

and $Y_C \Gamma_C^{ret}$ is the total self-sputtering flux with $Y_C$ given by

$$Y_C \;=\; Y_C^{phy} + Y_C^{RES} \tag{A.14}$$

$R_N^C \Gamma_C^{ret}$ is the backscattered carbon flux and $\Gamma_C^{evap}$ is the evaporated flux of carbon. $\Gamma_C^{ret}$ is the fraction $f_r$ of $\Gamma_C^{out}$ that returns to the target after ionization in the plasma.

$$\Gamma_C^{ret} = f_r \Gamma_C^{out} \tag{A.15}$$

$f_r$ is an external parameter which is an input to the model and should come from impurity transport calculations.

The flux of carbon atoms lost from the surface is

$$
\begin{aligned}
\Gamma_C^{loss} &=& \Gamma_C^{out} - R_N^C \Gamma_C^{ret} \\
&=& Y_H \Gamma_H + Y_C \Gamma_C^{ret} + \Gamma_C^{evap}
\end{aligned} \tag{A.16}
$$

and the flux of carbon atoms redeposited by the returning carbon flux is

$$\Gamma_C^{redep} \;=\; (1 - R_N^C) \Gamma_C^{ret} \tag{A.17}$$

From Eqns.A.12,A.15 we get

$$\Gamma_C^{ret} = \frac{f_r(Y_H \Gamma_H + \Gamma_C^{evap})}{1 - f_r(Y_C + R_N^C)} \tag{A.18}$$

The gross effective sputtering yield, defined as $\Gamma_C^{loss}/\Gamma_H$, using Eqns.A.16 and A.18 is

$$Y_{gross}^{eff} \;=\; \frac{(Y_H + \Gamma_C^{evap}/\Gamma_H)(1 - f_r R_N^C)}{1 - f_r(Y_C + R_N^C)} \tag{A.19}$$

The net effective sputtering yield, defined as $(\Gamma_C^{loss} - \Gamma_C^{redep})/\Gamma_H$, using Eqns.A.16,A.17 and A.18 is

$$Y_{net}^{eff} = \frac{(Y_H + \Gamma_C^{evap}/\Gamma_H)(1 - f_r)}{1 - f_r(Y_C + R_N^C)} \qquad (A.20)$$

Given a target density $n_{trg}(gm/cm^3)$ the gross or net thickness eroded per second (i.e. the gross or net erosion rate of the target) is given by

$$G = \frac{Y_{gross,net}^{eff} \; \Gamma_H \; M}{n_{trg} \; 6.0221 \times 10^{23}} \; (cm/sec) \qquad (A.21)$$

where M is the molecular weight of the target in amu and $\Gamma_H$ is given in particles/$cm^2/s$.

This model is readily extensible to an arbitrary charge state distribution of the incoming ions and energetic neutrals, provided one accounts for all the charge states and their respective incident energies and yields separately.

## A.2 Results

Using the simple model for PSI, assuming $T_i = T_e$, the target temperature (Fog.A.2) and the gross erosion rate (Fig.A.3) are plotted for a low density $(2.0 \times 10^{13}/cm^3/s)$ and for a high density $(8.0 \times 10^{13}/cm^3/s)$ case. Note that there is a range of $T_i$ wherein the gross erosion rate has a local maximum. The flattening off of the target temperature (and therefore gross erosion rate) in the high density case is artificial because the target surface temperature is not allowed to raise above 3000 K. From Fig.A.2 and Fig.A.4 we see that this is the range where the surface temperature of the target is ideal for maximum chemical erosion.

The local maximum suggests that there could be a plasma parameter range wherein one can see a radiative instability [98] like mechanism in the region where the gross erosion yield has a negative slope (Region I in Fig.A.5). In this region (Region-I), as the plasma temperature decreases, the gross erosion rate would increase thereby introducing more impurity into the plasma which can decrease the plasma temperature further. When the plasma temperature falls below the local maximum (Region-II of Fig.A.5) for gross erosion, a stabilizing mechanism exists wherein the gross erosion rate decreases at lower plasma temperatures and this decreases the impurities in the plasma which could lead to higher plasma temperatures. This could lead to the possibility of oscillations in plasma parameters about the local maximum [99].
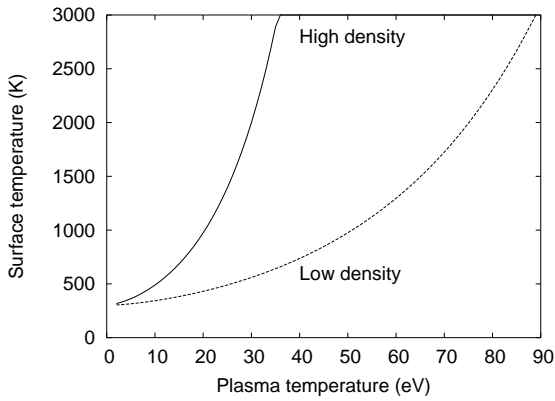
**Figure A.2:** Surface temperature as a function of $T_i$
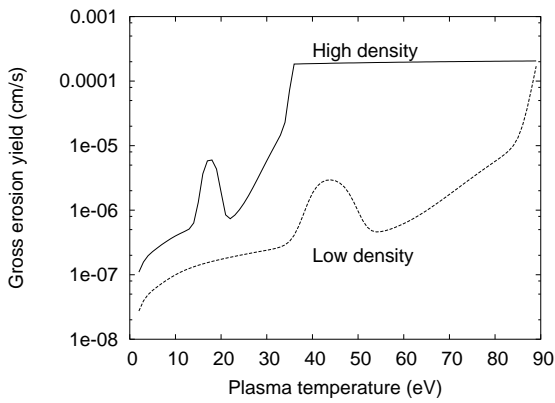


**Figure A.3:** Gross erosion rate a function of $T_i$
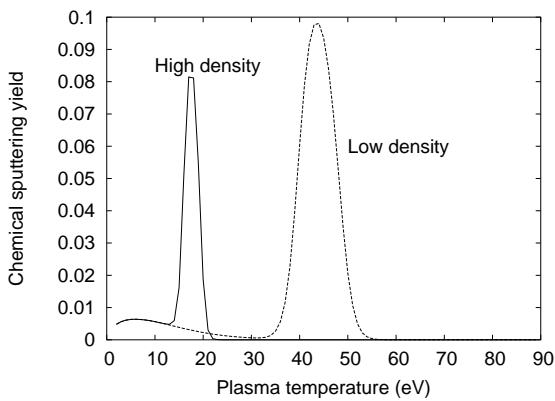


**Figure A.4:** Chemical sputtering yield a function of $T_i$

Therefore, using this model self consistently with a edge plasma code can clearly bring out the importance of self-consistently including the target temperature calculation in any PSI model.
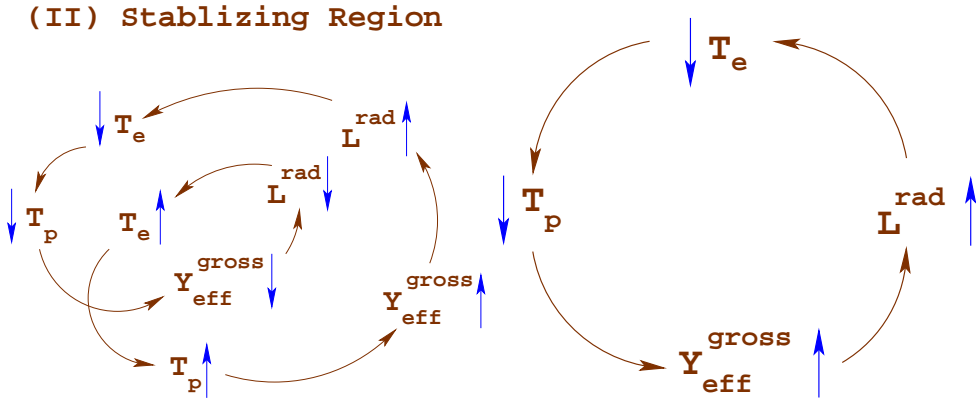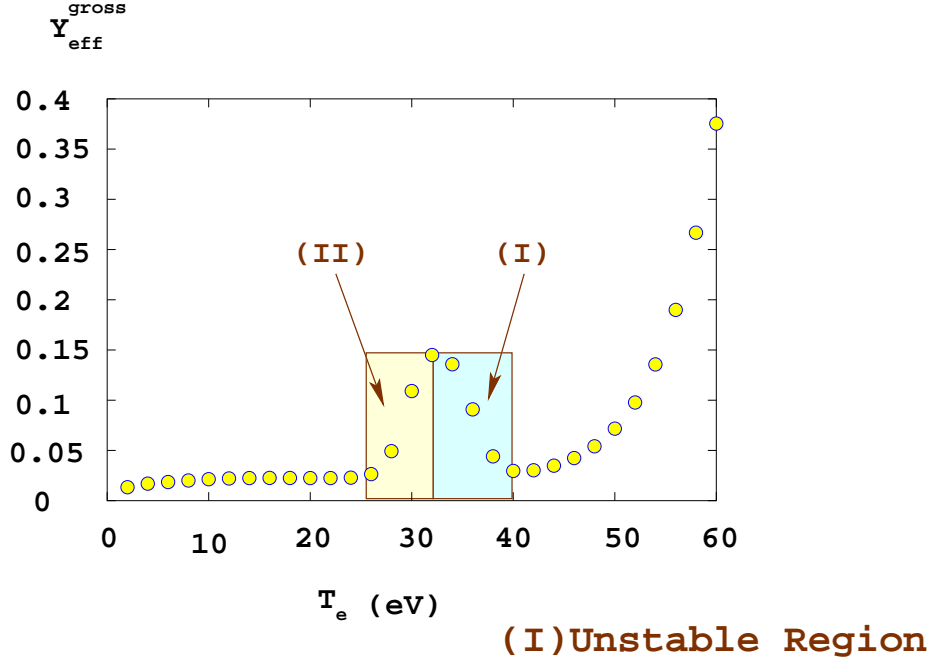
**Figure A.5:** Effective gross erosion yield Vs. Plasma temperature. The unstable region (Region I) and the stablizing region (Region II) are shown below the graph.

## A.3   SOLPS5.0-B2.5 results

The above model was included in the SOLPS5.0-B2.5 code [22, 23]. The results of a edge density scan for ASDEX-U geometry was carried out. We see a the possibility for the existence of oscillatory solutions as discussed above. Oscillatory solutions were observed experimentally [99] and predicted in earlier theoretical models [100]. These

solutions appear in the transition between low-recycling and high-recycling / detached operation. They show up as a hysteresis in the diagram of upstream densities vs. target plate plasma temperatures Fig.A.6. This is driven by the impurity production process itself and not by the negative slope of the carbon radiation characteristics. In simplified 1-D models the negative slope for the carbon radiation characteristics is sufficient to give oscillatory solutions [101]. In 2-D models this possibility seems to be removed due to reorganization of the solution avoiding such scenarios.



**Figure A.6:** The presence of a local maxima in chemical erosion yields manifesting as a hysteresis in the density scans of SOLPS-B2.5

# Appendix B

# Empirical formulas used for PSI
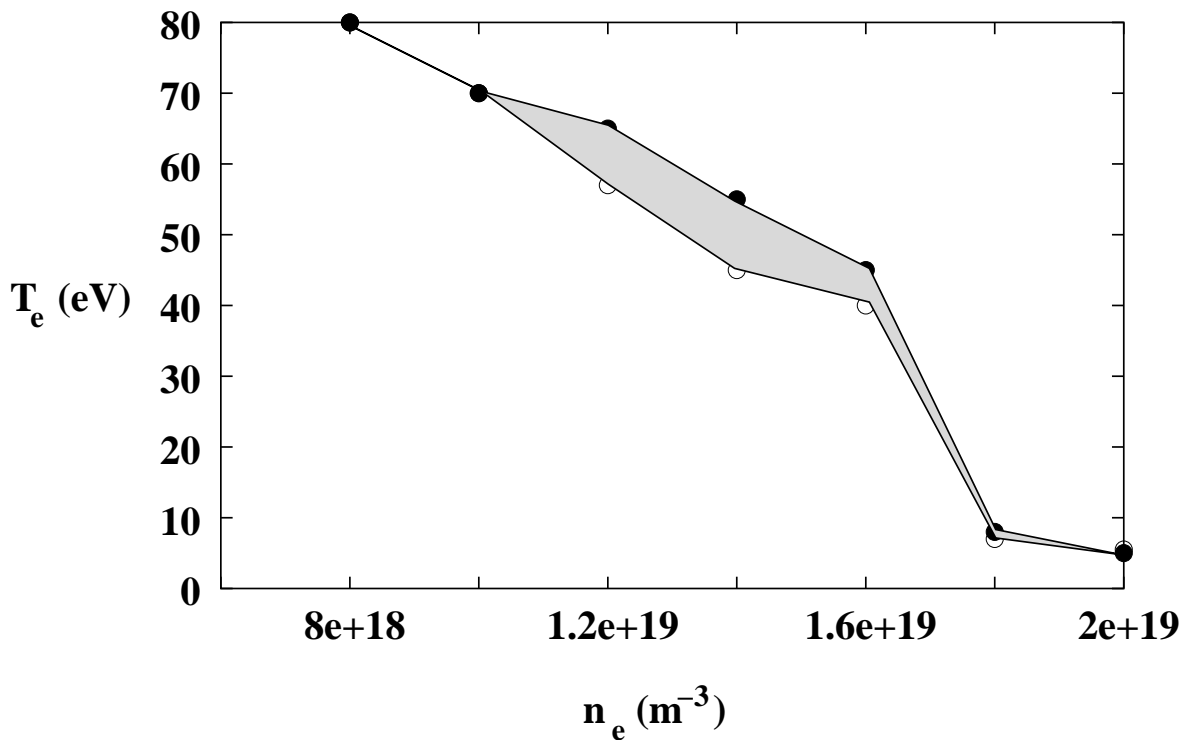
A large amount of work is dedicated to determining various PSI data by experiments and Monte-Carlo codes. These data are then made available as data sets [102, 103, 84] which can be used as inputs for plasma codes or semi-empirical formulas are developed to fit the available data ([17, 91, 92, 93, 94, 104, 105] and references therein). The data sets are available for a large number of projectile–target combinations. They are accurate and are used in existing transport codes [22, 23, 106, 107, 108] with a suitable interpolation to parameters of interest. However they cannot be extended to projectile-target combinations for which data are not available. The semi-empirical formulas on the other hand are not as accurate, but they have been developed by identifying the physical parameters on which the PSI processes depend and are fitted to the experimental and code-generated data, and therefore can be extrapolated to projectile-target combinations for which such data sets are not available. Using an empirical formula might also be computationally faster compared to doing a multidimensional sorting and interpolation on a large data set, especially for code packages which use PSIs as boundary conditions at each iteration. Some of these formulas are usually included in the existing transport codes [22, 23, 106, 107, 108].

In this appendix we present the semi–empirical formulas we have implemented as part of the simple model for PSI (Appendix.A) [21] and incorporated into SOLPS-B2.5.

# B.1   Physical sputtering

The physical sputtering yield $Y^{phy}$ calculation is based on the empirical formulas compiled in [91]. The Bohdansky formula [109] is used to determine the sputtering yield for normal incidence of a projectile on a target and the procedure specified by Yamamura [110] is used to specify the angular dependence:

$$Y^{phy}(E_0) \;=\; QS_n(\varepsilon)\left[1 - \left(\frac{E_{th}}{E_0}\right)^{2/3}\right]\left(1 - \frac{E_{th}}{E_0}\right)^2 \tag{B.1}$$

$$(cos\alpha)^{-f}exp\left(\;f\left[1 - (cos\alpha)^{-1}\right]cos\alpha_{opt}\;\right)$$

where $Q$ and the threshold energy $E_{th}$ are fitting parameters, $E_0$ is the incident particle energy (eV), $\varepsilon \;=\; E_0/E_{TF}$ is the reduced energy.
$E_{TF}$ is the Thomas-Fermi energy (eV):

$$E_{TF} \;=\; 30.74\frac{M_1 \;+\; M_2}{M_2}Z_1Z_2\left(Z_1^{2/3} \;+\; Z_2^{2/3}\right)^{1/2} \tag{B.2}$$

where $Z_1$, $Z_2$, $M_1$, $M_2$ are the nuclear charge and atomic mass of the projectile and target respectively.
$S_n$ is the nuclear stopping cross section based on the Kr-C potential, which is approximated by:

$$S_n(\varepsilon) \;=\; \frac{0.5\,ln\,(1 + 1.2288\varepsilon)}{\varepsilon \;+\; 0.1728\varepsilon^{1/2} \;+\; 0.008\varepsilon^{0.1504}} \tag{B.3}$$

$Q$ and $E_{th}$ are are given by:

$$QE_s^{2/3} = 1.633Z_1^{2/3}Z_2^{2/3}\left(Z_1^{2/3} \;+\; Z_2^{2/3}\right)^{1/3}\frac{M_1^{5/6}M_2^{1/6}}{M_1 + M_2}\frac{0.15 \;+\; 0.05M_2/M_1}{1 \;+\; 0.05(M_2/M_1)^{1.6}} \tag{B.4}$$

$$\frac{E_{th}}{E_s} = 7.0\,(M_2/M_1)^{-0.54} \;+\; 0.15\,(M_2/M_1)^{1.12} \tag{B.5}$$

where $E_s$ is the surface binding energy (heat of sublimation). $\alpha$ is the angle made by the incident projectile with the normal to the target surface. Yamamura's analytical fit formulas for f and $\alpha_{opt}$ are:

$$f = \sqrt{E_s}(0.94 - 1.33 \times 10^{-3}M_2/M_1) \tag{B.6}$$

$$\alpha_{opt} = \pi/2 - a_l n^{-1/3}(2\varepsilon\sqrt{E_s/\gamma E_o})^{-1/2} \tag{B.7}$$

where, $a_l$ is the Lindhard screening length ($= 0.4685\sqrt{Z_1^{2/3} + Z_2^{2/3}}$), n is the target density given in units of atoms / $^3$ and $\gamma$ is the maximum energy transfer factor given by $4M_1 M_2/(M_1 + M_2)^2$.

## B.2    Radiation enhanced sublimation

RES is observed only in graphite targets and the empirical formula is implemented only for a graphite target. The formula for the RES yield was obtained from [92] which states that the energy dependence of physical sputtering could also be applied to RES, with a modified value of $Q$ given by:

$$Q_{RES} \;=\; Q + 54 M_i^{1.18}\; e^{\frac{-0.78}{T}}\left(\frac{\Gamma}{10^{16}}\right)^{-0.1} \tag{B.8}$$

where $M_i =$ mass of incident ion (a.m.u.), $T$ is the plate temperature (eV) and $\Gamma$ is the incident ion flux ($cm^{-2}s^{-1}$). $M_i = 1$ for H$^+$. Then the RES yield is given by Eqn.B.1, with the value of Q replaced by Eqn.B.8 for $Q_{RES}$.

## B.3    Chemical erosion:

The chemical erosion yields formulas are described clearly by Roth in the Appendix A of [17]. Chemical erosion consists of two contributions, one the thermal part $Y^{therm}$ and the other the surface part $Y^{surf}$.

$$Y^{chem} = Y^{therm}\,(1\;+\;DY^{dam})\;+\;Y^{surf} \tag{B.9}$$

The thermal erosion is enhanced by the damage production due to incident ions $Y^{dam}$. D is given by $250/M_1$ where $M_1$ is the mass of the incident hydrogen isotope. The thermal erosion is obtained by the formula

$$Y^{therm} = c^{sp3}\;\frac{0.033\;e^{\frac{-E_{therm}}{KT}}}{2\times10^{-32}\phi + [1 + \frac{2\times10^{29}}{\phi}e^{\frac{-E_{rel}}{KT}}]e^{\frac{-E_{therm}}{KT}}} \tag{B.10}$$

where $KT$ is the target surface temperature in eV and $C^{sp^3}$ is given by:

$$C^{sp^3} = \frac{C[2 \times 10^{-32}\Phi + e^{\frac{-E_{therm}}{KT}}]}{2 \times 10^{-32} + [1 + \frac{2 \times 10^{29}}{\Phi} e^{\frac{-E_{rel}}{KT}}]e^{\frac{-E_{therm}}{KT}}}$$ (B.11)

We equate the value of C

$$C = \frac{1}{1 + 3 \times 10^7 e^{\frac{-1.4}{KT}}}$$ (B.12)

with its value for high ion fluxes where a possible influence of hydrogenation time is taken into account

$$C = \frac{1}{1 + 3 \times 10^{-23}\Phi}$$ (B.13)

in order to make a transition from low incident ion fluxes to high incident ion fluxes smoothly.

The term $Y^{dam}$ due to damage caused by incident ions is given by:

$$Y^{dam}(E_0) = QS_n \left[1 - \left(\frac{E_{dam}}{E_0}\right)^{2/3}\right] \left(1 - \frac{E_{dam}}{E_0}\right)^2$$ (B.14)

The surface erosion term is given by

$$Y^{surf}(E_o, T) = C^{sp^3} \frac{Y^{des}(E_o)}{[1 + e^{\frac{E_o - 65eV}{40}}]}$$ (B.15)

where

$$Y^{des}(E_0) = QS_n \left[1 - \left(\frac{E_{des}}{E_0}\right)^{2/3}\right] \left(1 - \frac{E_{des}}{E_0}\right)^2$$ (B.16)

The values recommended in Table 1 of [17] is used for $Q$, $E_{des}$ and $E_{dam}$. For $E_{rel}$ the value for pure carbon ($= 1.8eV$) is used. $E_{th}$, $E_{TF}$ and $S_n$ are calculated from Eqns.B.5,B.2, B.3. $E_{therm}$ is taken as $1.7eV$.

## B.4   Backscattering coefficients:

The empirical formula for values of $M_1/M_2 \leq 0.5$ are taken from [93] and that for values of $M_1/M_2$ up to 4.8 are taken from [94]. For a more detailed description of the variables and the expressions used, please check these original references. The formulas for the number backscattering coefficient $R_N$ and the energy backscattering coefficient

$R_E$ are related as follows:

$$R_N = R_E/r_E \tag{B.17}$$

where $r_E$ is given in terms of the reduced energy $\varepsilon = E_o/E_{TF}$ (see Eqn.B.2):

$$r_E = \frac{1}{1 + \left(\frac{\varepsilon}{0.133}\right)^{0.285}} + \frac{0.530}{1 + \left(\frac{\varepsilon}{85}\right)^{-1.46}} \tag{B.18}$$

For the $M_1/M_2 \leq 0.5$ case, $R_E$ is given by:

$$R_E = \frac{0.705/f}{1 + \left(\frac{\varepsilon}{0.047}\right)^{0.597} + \left(\frac{\varepsilon}{0.619}\right)^{1.5}} \tag{B.19}$$

where,

$$f = Z_1^{2/3} M_1^{-1/2} \alpha^{\frac{2\varepsilon-3}{\varepsilon+1}} \frac{\rho_a}{\rho_t} \tag{B.20}$$

where $\alpha = 1 + \frac{1}{\mu}$ with $\mu$ defined as $\mu = \frac{M-2}{M_1}$, and

$$\frac{\rho_a}{\rho_t} = \frac{\frac{2\varepsilon}{\rho_n} + \left[\frac{1}{S_L} + \frac{1}{4S_B}\right]^{-1}}{S_a} \tag{B.21}$$

with

$$\rho_a = \frac{\Gamma[0, (C-1)ln(B\varepsilon)] - \Gamma[0, -2ln(B\varepsilon)]}{A\ B} \tag{B.22}$$

where $A = 0.56258$, $B = 1.1776$, $C = 0.62680$, and $\Gamma$ is the upper incomplete gamma function given by:

$$\Gamma(\nu, x) = \int_x^\infty e^{-t} t^{\nu-1} dt \tag{B.23}$$

$S_L$, $S_B$ and $S_a$ are given by:

$$S_L = D \frac{\alpha^{\frac{3}{2}}}{\zeta} S_a \tag{B.24}$$

$$S_B = 61.47\ z_1\ \alpha\ \mu\ \zeta\ Z_2^{-\frac{2}{3}} \left(\frac{ln\left[\frac{\varepsilon_B}{1-\beta^2} + 1 + \frac{G}{\varepsilon_B}\right] - \beta^2}{I_o\ \varepsilon_B}\right) \tag{B.25}$$

$$S_a = 0.0793\ Z_1^{\frac{2}{3}}\ \mu\ \sqrt{\frac{\varepsilon}{M_1}} \tag{B.26}$$

where

$$D = 0.2617 \ (1 \ + \ Z_2^{\frac{2}{3}})^{\frac{3}{2}} \ Z_2^{-1} \ A_1 \tag{B.27}$$

$A_1$ is the co-efficient for electronic stopping cross section in the semi-empirical formula of Andersen and Ziegler [111].

$$\varepsilon_B \ = \ \frac{2m_e \ c^2 \ \beta^2}{Z_2 \ I_o} \tag{B.28}$$

$$I_o \ = \ \{^{12+7Z_2^{-1} \quad (for \ Z_2 < 13)}_{9.76+58.5Z_2^{-1.19} \quad (for \ Z_2 \geq 13)} \tag{B.29}$$

$$G \ = \ \{^{100Z_1/Z_2 \quad (for \ Z_1 < 3)}_{5 \quad (for \ Z_1 \geq 3)} \tag{B.30}$$

For the $0.5 < M_1/M_2 \leq 4.8$ case, the formulas from [94] are used and Eqn.B.17 is used to determine $R_E$. $R_N$ is given by:

$$R_N = \frac{G(\varepsilon)}{f_N} \tag{B.31}$$

where

$$G(\varepsilon) = \frac{1}{1 + \left(\frac{\varepsilon}{0.104}\right)^{0.577} + \left(\frac{\varepsilon}{0.730}\right)^{1.5}} \tag{B.32}$$

$$f_N = \frac{Z_1^{\frac{2}{3}}}{M_1^{\frac{1}{2}}} \frac{\rho_a}{\rho_t} \frac{\mu^2}{(1+\mu)^2 \ \psi} \tag{B.33}$$

and

$$\psi = \frac{1 \ + \ 24.1 \ \mu^{-3.995}}{\frac{\mu}{(1+\mu)(\frac{\varepsilon}{1.84}+1)} + \frac{(1+\mu)^3 \varepsilon}{\mu^3(1-\frac{3}{2\mu}+\frac{0.9}{\mu^2}+\frac{1}{2\mu^3})(\varepsilon+13.3)}} \tag{B.34}$$

For a compound target consisting of atoms with concentrations $c^a$, $c^b$, .... etc, atomic charge $Z^a$, $Z^b$, ... etc and atomic masses $M^a$, $M^b$, ..... etc, $Z_2$, and $M_2$ are replaced with $Z_c$ and $M_c$ to evaluate the value of $\varepsilon$, where

$$Z_c \ = \ \frac{c^a Z^a + c^a Z^b + ......}{c^a + c^b + .....} \tag{B.35}$$

$$M_r \ = \ \frac{c^b M^a + c^b M^b + ......}{c^a + c^b + .....} \tag{B.36}$$

Values of $2\varepsilon/\rho$, $S_L$, $S_b$ and $S_a$ for the compound target are calculated using the Bragg rule.

# Bibliography

[1] S. Eliezer and Y. Eliezer. A universe of plasma. *The Fourth State of Matter: An Introduction to Plasma Science, Institute of Physics Publishing, Bristol and Philadelphia, $2^{nd}$ Edition*:49–78, (2001).

[2] Boris V. Somov. Cosmic plasma physics. *Book, Astrophysics and space science library, Kluwer academic publishers, Dordrecht/Boston/London*, (2000).

[3] S. Eliezer and Y. Eliezer. The solution to the energy problem. *The Fourth State of Matter: An Introduction to Plasma Science, Institute of Physics Publishing, Bristol and Philadelphia, $2^{nd}$ Edition*:103–153, (2001).

[4] S. Eliezer and Y. Eliezer. Plasma in industry. *The Fourth State of Matter: An Introduction to Plasma Science, Institute of Physics Publishing, Bristol and Philadelphia, $2^{nd}$ Edition*:79–102, (2001).

[5] F. F. Chen. Introduction to plasma physics. *Plenum press, New York*, 1974.

[6] J. A. Bittencourt. Fundamentals of plasma physics. *Pergamon Press, Oxford*, 1986.

[7] M. A. Leontovich. Reviews of plasma physics (series). *Consultants Bureau, New York*, 1965.

[8] J. D. Lawson. Some criteria for a power producing thermonuclear reactor. *Proceedings of the physical society*, B 70(6), (1957).

[9] R. Schneider. Plasma edge physics for tokamaks. *Max–Planck–Institut f/"ur Plasmaphysik Report*, IPP 12/1, Februar (2001).

[10] P. C. Stangeby. The plasma boundary of magnetic fusion devices. *Plasma Physics series, Institute of physics publishing*, (2000).

[11] R. Chodura. Plasma flow in the sheath and presheath of a scrape–off layer. *Physics of plasma-wall interactions in controlled fusion, Ed. D.E. Post and R. Behrisch NATO ASI series*, Plenum press, New York:99–134, rk.

[12] K.U. Riemann. The bohm criterion and sheath formation. *J. Phys. D: Appl. Phys.*, 24:493–518, (1991).

[13] D. Sharma and H. Ramachandran. Structure of a source driven magnetized oblique presheath. *Phys. Rev. E*, 66:26412, (2002).

[14] R. Chodura. Plasma flow in the sheath and presheath of a scrape–off layer. *Physics of Plasma–wall interactions in controlled fusion, Ed. D. E. Post and R. Behrisch, NATO ASI series*, Series B, Physics Vil. 131:99–134, l. 131.

[15] P. Sigmund. Mechanisms and theory of physical sputtering by particle impact. *Numerical Instruments and Materials in Physics Research*, B27:1–20, (1987).

[16] W. Eckstein and V. Philipps. Physical sputtering and radiation-enhanced sublimation. *W.O. Hofer, J. Roth eds. Physical processes in the interaction of fusion plasmas with solids (Academic press)*, pages 93–133, (1996).

[17] J. Roth. Chemical erosion of carbon-based materials in fusion devices. *J. Nucl. Mater.*, 266-269:51–57, (1999).

[18] J. Küppers. The hydrogen surface chemistry of carbon as a plasma facing material. *Surface Science Reports*, 22:249–321, (1995).

[19] E. Salonen, K. Nordlund, J. Keinonen, and C. H. Wu. Swift chemical sputtering of amorphous hydrogenated carbon. *Phys. Rev. B*, 63:195415–(1–14), (2001).

[20] C. Hopf, A. von Keudell, and W. Jacob. Chemical sputtering of hydrocarbon films. *Jnl. App. Phys.*, 94(4):2373–2380, (2003).

[21] M. Warrier, R. Schneider, and X. Bonnin. Subroutines for some plasma surface interaction processes: physical sputtering, chemical erosion, radiation enhanced sublimation, backscattering and thermal evaporation. *Computer Physics Communication*, 160(1):46–68, (2004).

[22] V. Rozhansky, S. Voskoboynikov, E. Kovaltsova, D. Coster, and R. Schneider. Perpendicular conductivity and self-consistent electric fields in tokamak edge plasma. *Contrib. Plasma Phys.*, 40:423–430, (2000).

[23] R. Schneider, D. Coster, B. Braams, P. Xantopoulos, V. Rozhansky, S. Voskoboynikov, E. Kovaltsova, and H. Bürbaumer. B2-solps5.0: Sol transport code with drift and currents. *Contrib. Plasma Phys.*, 40:328–333, (2000).

[24] H. Wolff. Arcing in magnetic fusion devices. *Atomic and plasma–material interaction data for fusion, (supplement to the journal Nuclear Fusion)*, 1:93–107, (1991).

[25] Y. Ueda, T. Shimada, and M. Nishikawa. Impacts of carbon impurities in hydrogen plasmas on tungsten blistering. *Nucl. Fusion*, 44:62–67, (2004).

[26] J. Winter. Dust in fusion devices – experimental evidence, possible sources and consequences. *Plasma Phys. Control. Fusion*, 40:1201–1210, (1998).

[27] E. W. Thomas. Particle induced electron emission. *Atomic and plasma–material interaction data for fusion (Supplement to the journal Nuclear Fusion)*, 1:79–91, (1991).

[28] J. Wesson. *Tokamaks (Second Edition), Oxford Science Publishing*, page 11, (1997).

[29] J. D. Huba. Revised nrl plasma formulary. *Naval Research Laboratory, Washington DC*, page 56, (2000).

[30] ITER team. Iter physics basis. *Muclear Fusion*, 39(12):2137–2664, (1999).

[31] D.G. Whyte, G.R. Tynan, R.P. Doerner, and J.N. Brooks. Investigation of carbon chemical erosion with increasing plasma flux and density. *Nuclear Fusion*, 41(1):47–62, (2001).

[32] V. Dose, R. Preuss, and J. Roth. Evaluation of chemical erosion data for carbon materials at high ion fluxes using bayesian probability theory. *J. Nucl. Mater.*, 288:153, (2001).

[33] G. Federici et. al. Plasma-material interactions in current tokamaks and thier implications for next–step fusion reactors. *Nuclear Fusion*, 41(12R):1967–2137, (2001).

[34] B. V. Mech, A. A. Haasz, and J. W. Davis. Model for the chemical erosion of graphite due to low-energy h+ and d+ impact. *J. Appl. Phys.*, 84(3):1655–1669, (1998).

[35] K. L. Wilson et. al. Trapping, detrapping and release of implanted hydrogen isotopes. *Atomic and plasma-material interaction data for fusion (supplement to the journal Nuclear Fusion*, 1:31–50, (1991).

[36] G. Federici et. al. In-vessel tritium retention and removal in iter. *J. Nucl. Mater.*, 266-269:14–29, (1999).

[37] G. Janeschitz, ITER JCT, and HTs. Plasma-wall interaction issues in iter. *J. Nucl. Mater.*, 290-293:1–11, (2001).

[38] Wolfhard Möller. Hydrogen trapping and transport in carbon. *J. Nucl. Mater.*, 162-164:138–150, (1989).

[39] A. A. Haasz, P. Franzen, J. W. Davis, S. Chiu, and C. S. Pitcher. Two-region model for hydrogen trapping in and release from graphite. *J. Appl. Phys.*, 77(1):66–86, (1995).

[40] A. Hassanein, B. Wiechers, and I. Konkashbaev. Tritium behaviour in eroded dust and debris of plasma-facing materials. *J. Nucl. Mater.*, 258-263:295–300, (1998).

[41] G. Federici and C.H. Wu. Modelling of plasma hydrogen isotope behavious in porous materials (graphites/carbon-carbon composites). *J. Nucl. Mater.*, 186:131–152, (1992).

[42] B. M. U. Scherzer, M. Wielunski, W. Möller, A. Turos, and J. Roth. Hydrogen–ion–induced detrapping of implanted deuterium in graphite. *Nucl. Instrum. Methods Phys. Res. B*, 33:714, (1988).

[43] B. M. U. Scherzer, J. Wang, and W. Möller. Temperature dependence of ion-induced detrapping of deuterium in graphite. *J. Nucl. Mater.*, 162-164:1013, (1989).

[44] W. Möller and B. M. U. Scherzer. Modeling of hydrogen implantation into graphite. *J. Appl. Phys.*, 64:4860, (1988).

[45] R. A. Causey. The interaction of tritium with graphite and its impact on tokamak operations. *J. Nucl. Mater.*, 162-164:151, (1989).

[46] H. Atsumi, S. Tokura, and M. Miyake. Absorption and desorption of deuterium on graphite at elevated temperatures. *Proc. 3rd Int. Conf. on Fusion Reactor Materials, Karlsruhe, (1987), J. Nucl. Mater.*, 155-157:241, (1988).

[47] Y. Ferro, F. Marinelli, and A. Allouche. Density functionl theory investigation of the diffusion and recombination of h on a graphite surface. *Chemical Physics Letters*, 368:609–615, (2003).

[48] Y. Ferro, F. Marinelli, and A. Allouche. Density functional theory investigation of h adsorption and $h_2$ recombination on the basal plane and in the bulk of graphite: Connection between slab and cluster model. *Journal of Chemical Physics*, 116(18):8124–8131, (2002).

[49] F. Graziani. Radiation transport in hetrogeneous materials. *APS meeting : Conference on Computational Physics 2002*, August 25-28(San Diego), (2002).

[50] D. Frenkel and B. Smit. Understanding molecular simulations: From algorithms to applications. *Academic Press, Computational Science Series, Vol. 1*, (2002).

[51] K. Nordlund. Introduction to atomistic simulations. *http://www.acclab.helsinki.fi/$\sim$ knordlun/atomistiset*, (2003).

[52] P. Hohenberg and W. Kohn. Inhomogeneous electron gas. *Phys. Rev.*, 136:B864–B867, (1964).

[53] W. Kohn and L. J. Sham. Self–consistent equations including exchange and correlation effects. *Phys. Rev.*, 140(4A):1133–1138, (1965).

[54] W. Matthew, C. Foulkes, and R. Haydock. Tight–binding models and density–functional theory. *Phys. Rev. B*, 39(17):12520–12536, (1989).

[55] N. W. Ashcroft and N. D. Mermin. *Solid state physics, Saunders College Publishing*, page 398, (1976).

[56] P. M. Morse. Diatomic molecules according to the wave mechanics. ii. vibrational levels. *Phys. Rev.*, 34(1):57, (1929).

[57] F. H. Stillinger and T. A. Weber. Computer simulation of local order in condensed phases of silicon. *Phys. Rev. B*, 31(8):5262–5271, (1985).

[58] M. S. Daw and M. I. Baskes. Embedded–atom method: Derivation and application to impurities, surfaces, and other defects in metals. *Phys. Rev. B*, 29(12):6443–6453, (1984).

[59] D. W. Brenner. The art and science of an analytic potential. *phys. stat. sol.*, (b) 217:23–40, (2000).

[60] G. C. Abell. Empirical chemical pseudopotential theory of molecular and metallic bonding. *Physical Review B*, 31(10):6184–6196, (1985).

[61] J. Tersoff. New empirical approach for the structure and energy of covalent systems. *Physical Review B*, 37(12):6991–7000, (1988).

[62] D. W. Brener. Chemical dynamics and bond-order potentials. *Mater. Res. Soc. Bull.*, 21(2):36, (1996).

[63] D. W. Brenner. Empirical potential for hydrocarbons for use in simulating the chemical vapour deposition of diamond films. *Phys. Rev. B*, 42:9458, (1990).

[64] K. Nordlund, J. Keinonen, and T. Mattila. Formation of ion irradiation induced small-scale defects on graphite surfaces. *Phys. Rev. Lett.*, 77:699, (1996).

[65] D. C. Rapaport. The art of molecular dynamics simulation. *Cambridge university press*, (1995).

[66] M. P. Allen and D. J. Tildesley. Computer simulation of liquids. *Oxford science publications*, (1987).

[67] H. C. Andersen. Molecular dynamics simulations at constant pressure and/or temperature. *J. Chem. Phys.*, 72(4):2384–2393, (1980).

[68] W. G. Hoover. Canonical dynamics: Equilibrium phase–space distributions. *Phys. Rev. A*, 31(3):1695–1697, (1985).

[69] H. J. C. Berendsen, J. P. M. Postma, W. F. Van Gunsteren, A. DiNola, and J. R. Haak. Molecular dynamics with coupling to an external bath. *J. Chem. Phys.*, 81(8):3684–3690, (1984).

[70] J. M. Lahtinen. Diffusive dynamics of interacting particles in equilibrium and under hydrodynamic sedimentation. *Ph.D Dissertation, Laboratory of Physics, Helsinki university of technology, Finland*, (2002).

[71] K.A. Fichthorn and W.H. Weinberg. Theoritical foundations of dynamical monte carlo simulations. *J, Chem. Phys.*, 95(2):1090–1096, (1991).

[72] Arthur F. Voter, Francesco Montalenti, and Timothy C. Germann. Extending the time scales in atomistic simulation of materials. *Annu. Rev. Mater. Res.*, 32:321–346, (2002).

[73] A. B. Bortz, M. H. Kalos, and J. L. Lebowitz. A new algorithm for monte carlo simulation of ising spin systems. *J. Computational Physics*, 17:10, (1975).

[74] Joseph Klafter, Michael F. Shlesinger, and Gert Zumofen. Beyond brownian motion. *Physics Today*, February:33–39, (1996).

[75] W. D. Luedtke and U. Landman. Slip diffusion and lévy flights of an adsorbed gold nanocluster. *Phys. Rev. Lett.*, 82(19):3835–3838, (1999).

[76] R. N. Mantegna and H. E. Stanley. Stochastic processes with ultraslow convergence to a gaussian: The truncated lévy flight. *Phys. Rev. Lett.*, 73(22):2946–2949, (1994).

[77] J. J. Sarraille. Developing algorithms for measuring fractal dimension. *http://www.arbitrage-trading.com/Downloads/ARTiclesJJSAuthorsNotes.pdf*, (1992).

[78] H. Goldstein. Classical mechanics. *Addison Wesley publishing company*, (1971).

[79] R. A. Causey, M. I. Baskes, and K. L. Wilson. The retention of deuterium and tritium in poco axf-5q graphite. *J. Vac. Sci. Technol. A*, 4(3):1189–1192, (1986).

[80] S.C. Badescu, S.C. Ying, and T. Ala-Nissila. Quantum diffusion of h/ni(111) through a monte carlo wave function formalism. *Physical Review Letters*, 86(22):5092–5095, (2001).

[81] M. Warrier, R. Schneider, E. Salonen, and K. Nordlund. Multi-scale modelling of hydrogen isotope diffusion in graphite. *Contrib. Plasma Phys.*, 44(1-3):307–310, (2004).

[82] M. Mayer, M. Balden, and R. Behrisch. Deuterium retention in carbides and doped graphites. *J. Nucl. Mater.*, 252:55–62, (1998).

[83] W. Eckstein. Computer simulations of ion–solid interactions. *Springer series in material science 10, Springer-Verlag*, (1991).

[84] W. Eckstein. Calculated sputtering, reflection and range values. *Rep. IPP 9/132, Max-Planck-Institut für Plasmaphysik, Garching, Germany*, (2002).

[85] P. E. Kloeden and E. Platen. Numerical solution of stochastic differential equations. *Springer series in Applications of Mathematics*, 23, (1999).

[86] K. Ashida, K. Ichimura, M. Matsuyama, and K. Watanabe. Thermal desorption of hydrogen, deuterium and tritium from pyrolytic graphite. *J. Nucl. Mater.*, 128 & 129:792, (1984).

[87] P. Franzen and E. Vietzke. Atomic release of hydrogen from pure and boronized graphites. *J. Vac. Sci. Technol. A*, 12(3):820–825, (1994).

[88] E. de Juan Pardo. Private communication.

[89] M. Balden, E. Oyarzabal, E. de Juan Pardo, K. Durocher, J. Roth, and C. Garćia-Rosales. Deuterium retention by implantation in carbide–doped graphites. *Physica Scripta*, T103:38–42, (2003).

[90] S. Havlin and D. Ben-Avraham. Diffusion in disordered media. *Adv. Phys.*, 51(1):187–292, (2002).

[91] C. García-Rosales, W. Eckstein, and J. Roth. Revised formulae for sputtering data. *J. Nucl. Mater.*, 218:8–17, (1994).

[92] J. Roth, E. Vietzke, and A.A. Haasz. Eosion of graphite. *Supplement to the Journal Nuclear Fusion*, 1:63–78, (1991).

[93] R. Ito, T. Tabata, N. Itoh, K. Morita, T. Kato, and H. Tawata. Data on the backscattering coefficients of light ions from solids (a revision). *Institute of Plasma Physics Report, Nagoya, Japan*, IPPJ-AM-41, (1985).

[94] T. Tabata and R. Ito. Present status of data compilation on ion backscattering. *Institute of Plasma Physics Report, Nagoya, Japan*, IPPJ-AM-64:84–89, (1989).

[95] Frank P. Incropera and David P. DeWitt. Introduction to heat transfer. *John Wiley and sons*, pages 63–68, (2002).

[96] R. Behrisch. Contribution of the different erosion processes to material release from the vessel walls of fusion devices during plasma operation. *Contrib. Plasma Physics*, 42((2-4)):431–444, (2002).

[97] C. García Rosales. Erosion processes in plasma wall interactions. *J. Nucl. Mater.*, 211:202–214, (1994).

[98] J. F. Drake. Marfes: Radiative condensation in tokamak edge plasma. *Physics of Fluids*, 30:2429–2433, (1987).

[99] U. Wenzel, P. Bachmann, A. Carlson, M. Laux, B. Napiontek, and M. Weinlich. Relaxation oscillations in the asdex upgrade tokamak. *Nuclear Fusion*, 37(10):1343–1347, (1937).

[100] P. Bachmann, D. Sünder, and U. Wenzel. Bifurcation and relaxation oscillations in divertor plasmas. *Contrib. Plasma Phys.*, 36:519, (1996).

[101] J. Neuhauser, W. Schneider, and R. Wunderlich. Thermal instabilities and poloidal asymmetries in the tokamak edge plasma. *Nucl. Fusion*, 26(12):1679, (1986).

[102] W. Eckstein, C. García-Rosales, J. Roth, and W. Ottenberger. Sputtering data. *Rep. IPP 9/82, Max-Planck-Institut für Plasmaphysik, Garching, Germany*, (1993).

[103] W. Eckstein. Sputtering, reflection and range values for plasma edge codes. *Rep. IPP 9/117, Max-Planck-Institut für Plasmaphysik, Garching, Germany*, (1998).

[104] R. A. Langley, J. Bohdansky, W. Eckstein, P. Mioduszewski, J. Roth, E. Tagleur, E. W. Thomas, H. Verbeek, and K.L. Wilson. Data compendium for plasma surface interactions. *Supplement to the journal Nuclear Fusion*, (1984).

[105] R.K. Janev. Scientific ed., atomic and plasma-material interaction data for fusion. *Supplement to the journal Nuclear Fusion*, 1, (1991).

[106] R. Simonini, A. Taroni, M. Keilhacker, G. Radford, J. Spence, G.Vlases, M.L. Watkins, and S. Weber. Modelling inpurity control at jet. *J. Nucl. Mater.*, 196-198:369–373, (1992).

[107] R. Simonini, G. Corrigan, G. Radford, J. Spence, and A. Taroni. Models and numerics in th multi–fluid 2–d edge plasma code edge2d/u. *Contrib. Plasma Phys.*, 34:368–373, (1994).

[108] D. Naujoks, R. Behrisch, J.P. Coad, and L.C.J.M. De Kock. Material transport by erosion and redeposition on surface probes in the scrape off layer of jet. *Nuclear Fusion*, 33(4):581–590, (1993).

[109] J. Bohdansky. A universal relation for the sputtering yield of monatomic solids at normal ion incidence. *Nucl. Inst. and Meth.*, B 2:587, (1984).

[110] Y. Yamamura, Y. Itikawa, and N. Itoh. Angular dependence of sputtering yields of monoatomic solids. *Rep. IPPJ-AM-26, Institute of Plasma Physics, Nagoya, Japan*, (1983).

[111] H.H. Anderson and J.F. Ziegler. Hydrogen stopping powers and ranges in all elements. *Pergamon press, Elmsford, N.Y*, (1977).

# Acknowledgments

This work would not have been possible without the support of my thesis supervisor, Dr. Ralf Schneider, Prof. P. K. Kaw and Dr. Shishir Deshpande. I thank Prof. Dr. Jürgen Nührenberg for giving me an opportunity to work in his group at the Max-Planck-Institut für Plasmaphysik (IPP), Greifswald, Germany. I thank Prof. P. K. Kaw, Dr. S. P. Deshpande and the academic committee from the Institute for Plasma Research (IPR), Gandhinagar, India, for granting me leave to do this study.

Ralf always showed me light when I was stuck in any problem. I would like to thank Shishir for the early discussions and for his discourse on how to conduct a literature survey. The collaboration with Prof. Kai Nordlund and Dr. Emppu Salonen from the Accelerator Laboratory, Helsinki, Finland has helped me enormously. I would like to thank Kai for letting me use his molecular dynamics code HCParcas and for the great notes he provides at his home page. I have widely used these notes when introducing MD simulations in this thesis without citation at each instance. Thanks to Emppu for teaching me to use HCParcas, and for his enthusiasm which got things going. The brainstorming sessions at Helsinki and by e–mail with both of them were very useful. Dr. Xavier Bonnin was instrumental in cleaning up the plasma surface interaction sub-routines and incorporating them in B2.5-SOLPS. I thank him and Dr. David Coster for their interest and encouragement. Thanks to Dr. A. Runov for introducing me to Monte–Carlo diffusion. Thanks to Dr. K. M. Kolwankar and Dr. R. Ganesh for some short, but very useful discussions on Lévy flights and fractal dimensions.

My colleagues at the Stellaratortheorie division at IPP were helpful in a variety of ways and I thank each of them. Special thanks to Jutta Gaugher who made difficult office procedures look simple. Henry and Matthias made stubborn compilers, puzzling networks, and unyielding computing systems, behave synergistically. Many thanks to the Materials research Group at IPP Garching for hosting me for a very productive

week. I would specially like to thank Elena de Juan Pardo for the various references she gave me and the discussions we had during the visit to IPP-Garching. The International Max-Planck Research School (IMPRS) was interesting and useful. Thanks to Prof. Tomas Klinger, Dr. Olaf Gurlke and Dr. Ramin Madani who made it so. Many thanks to Devendra for his "addref" package which saved me a lot of time, and also for his coffee time discussions. I would like to thank Frau. Schirmacher, the librarian of IPP–Greifswald for her help in obtaining numerous references and books. There are a couple of regrets too, like, not continuing the nice plasma physics discussions with Vasile and Shyju, and, not doing at least a a small plasma instability problem inspite of being part of Stellaratortheorie.

I remember Shashank teaching me how to get started on a problem fast, Ganesh for the many discussions we had over a period of ten years which have no doubt contributed to the way I did this study and Shishir for teaching me how to make simple models for seemingly complex phenomena. I missed the three of them during the course of this study. Ralf was an amalgamation of the three of them and I guess that is what saw me through this work. The nine years I spent at IPR was most helpful and I thank my teachers, colleagues and friends who taught me a lot of things not restricted to only plasma physics.

I would like to thank the developers of Linux, GNU, TeX/LaTeX for making computing a pleasure, the gsl developers for their nice numerical library and Daniel Spanberg for his nice molecular dynamics viewer ymol.

As I submit this thesis I remember a host of friends and relatives who have wished me well and helped me at various times. I would like to thank Abbaiee, Amaiee and BIL, for holding the fort at crucial moments. Finally a big thanks to Vaishali, my daughter, who put the Ph.D in perspective within the global scheme of life.

Hiermit erkläre ich, daß diese Arbeit bisher von mir weder an der Mathematisch-Naturwissenschaftlichen Fakultät der Ernst-Moritz-Arndt-Universität Greifswald noch einer anderen wissenschaftlichen Einrichtung zum Zwecke der Promotion eingereicht wurde.

Ferner erkläre ich, daß ich diese Arbeit selbständig verfaßt und keine anderen als die darin angegebenen Hilfsmittel benutzt habe.

Greifswald, im August 2004

---

(Manoj Warrier)